Phenotypic Analysis of Motor Defects in Neuronal Ostm1 Conditional Loss of Function

Milhem Hajj Hassan

Master of Science

Faculty of Graduate Studies

Division of Experimental medicine

McGill University

Montreal, Quebec, Canada

April 2020

A thesis submitted To McGill University in partial fulfillment

of the requirements of the degree of Master of Science

TABLE OF CONTENTS

LIST OF TABLES

LIST OF FIGURES

ABSTRACT

Mutations in the human and mouse *OSTM1/Ostm1* gene result in the most severe form of autosomal recessive osteopetrosis, an inherited hematopoietic bone disorder. We isolated and characterized the *Ostm1* gene responsible for the spontaneous murine osteopetrotic *gl* mutation and functional rescue of hematopoietic defects was obtained in PU.1-*Ostm1 gl/gl* BAC transgenic mice. However, these transgenic *gl/gl* mice became overtly ill and died prematurely around 6-7 weeks with severe neurodegeneration associated with impaired autophagy. To investigate whether Ostm1 has a direct role in neuronal cells, we generated a conditional *Ostm1*$^{lox/lox}$ allele to address the *Ostm1* neuronal specificity with Synapsin1-Cre loss of function. *Ostm1*$^{lox/lox}$ SYN1-Cre^{+} progenies developed normally until ~7 weeks and were undistinguishable from control littermates. Around ~8-9 weeks of age *Ostm1*$^{lox/lox}$ Synapsin1-Cre^{+} mice developed a rapid and progressive neuronal deficit. These mice showed abnormal limb-clasping reflexes, severe motor defects and stopped gaining weight. Consistently, brain histology revealed inflammatory response with gliosis, loss of neuronal cells in CA3 and dentate gyrus of the hippocampus and thinning of the cortex. Spinal cord EM analysis showed axonal swelling with accumulation of vesicular structures similar to autophagosomes. End-stage disease is characterized by hind limbs paralysis consistent with reduced motor neurons population, neuromuscular junctions' pathology and muscle fiber atrophy. Together, our results provided evidence that the Ostm1 plays a major role in neuronal homeostasis and further establish an Ostm1 neuromuscular crosstalk.

RÉSUMÉ

Les mutations du gène *OSTM1/Ostm1* humain et de souris entraînent la forme la plus sévère d'ostéopétrose autosomique récessive, une maladie osseuse hématopoïétique héréditaire. Nous avons isolé et caractérisé le gène *Ostm1* responsable de la mutation *gl* spontanée ostéopétrotique murine et le sauvetage fonctionnel des défauts hématopoïétiques a été obtenu chez des souris transgéniques PU.1-*Ostm1 gl/gl* BAC. Cependant, ces souris transgéniques *gl/gl* tombent gravement malades et meurent prématurément vers 6-7 semaines avec une neurodégénérescence grave associée à une autophagie altérée. Pour étudier si Ostm1 a un rôle direct dans les cellules neuronales, nous avons généré un allèle *Ostm1*$^{lox/lox}$ conditionnel pour répondre à la spécificité neuronale *Ostm1* avec perte de fonction Synapsin1-Cre. Les descendances d'*Ostm1*$^{lox/lox}$ SYN1-Cre^{+} se sont développées normalement jusqu'à ~7 semaines et ne se distinguaient pas des compagnons de portée témoins. Vers l'âge de 8 à 9 semaines, les souris *Ostm1*$^{lox/lox}$ Synapsin1-Cre^{+} ont développé un déficit neuronal rapide et progressif. Ces souris ont présenté des réflexes anormaux de raideur des membres, de graves défauts moteurs et ont arrêté de prendre du poids. De manière cohérente, l'histologie cérébrale a révélé une réponse inflammatoire avec gliose, perte de cellules neuronales dans CA3 et gyrus denté de l'hippocampe et amincissement du cortex. L'analyse par ME de la moelle épinière a montré un gonflement axonal avec une accumulation de structures vésiculaires similaires aux autophagosomes. La maladie en phase terminale est caractérisée par une paralysie des membres postérieurs compatible avec une réduction de la population de motoneurones, une pathologie des jonctions neuromusculaires et une atrophie des fibres musculaires. Ensemble, nos résultats démontrent que l'Ostm1 joue un rôle majeur dans l'homéostasie neuronale et établissent en outre une diaphonie neuromusculaire Ostm1.

ACKNOWLEGDMENTS

I would like to thank my supervisor, Dr Jean Vacher, for his guidance and support which helped me develop my research skills and build stronger lab practices. Dr. Vacher helped guiding me in analyzing results from a variety of perspectives. Being a member of his lab was a crucial and transformative learning experience. Regular group meetings helped create a collegial and collaborative environment where different ideas were discussed and students were allowed to grow and thrive. Overall, undertaking my masters program at the McGill and IRCM helped make me a more well-rounded researcher.

I would also like to acknowledge the help of my lab members, especially our research assistant, Monica Pata. Monica was friendly, patient and supportive, available to offer help and support whenever possible. Her presence and knowledge helped me in my learning of different molecular and histological techniques which, in turn, helped make my work smoother and more effective.

Finally, I would like to thank God for his benevolent giving, support, caring and loving and for gifting me my incredible parents. I want to thank my Dad, Ali Hajj Hassan, and my Mom, Maissa Mossawi, for their unconditional sacrifices during my entire life and for being understanding, caring and supportive parents. Their encouragement, advices and love made me what I am today and helped me in achieving my dreams. I am blessed and grateful to have them as the guiding light of my life.

CONTRIBUTION OF AUTHORS

The author generated the text, the data in the introduction and the 5 chapters of the thesis which are: literature review, material and methods, results, discussion, and conclusion and perspectives.

In the literature review, the figures were reproduced from its original source with permission. Moving to materials and methods and results, Dr. Vacher's laboratory generated the *Ostm1* neuronal conditional knockout mouse model and contributed in the development of the project. All figures were generated by the author except the electron microscopy (EM) (Figure 3-11) and the neuromuscular junction (NMJ) (Figure 3-12) images were generated with the contribution of others. For the EM images, Diane Gingras M.Sc. (EM Manager, Département de pathologie et biologie cellulaire, Montreal University) captured the images of the anterior horn of the lumbar spinal cord. For the NMJ images, Monica Pata aided me through the experiment and Dr. Rashmi Kothary contributed in sharing the protocol.

ABBREVIATIONS

3-MA: 3-methyladenine

ADO: Autosomal Dominant Osteopetrosis

alpha-BTX: alpha-Bungarotoxin

ALS: Amyotrophic Lateral Sclerosis

APP: Amyloid Precursor Protein

ARO: infantile malignant Autosomal Recessive Osteopetrosis

ATG: Autophagy-related protein

BAC: Bacterial Artificial Chromosome

BECN1: Beclin-1

BMD: Bone Mineral Density

Br: Brain

CA-II: Carbonic Anhydrase-2 gene

ChAT: Choline Acetyltransferase

cKO: conditional KnockOut

Cl^-: Chloride

CNS: Central Nervous System

CO_2: Carbon dioxide

CSF: Cerebrospinal Fluid

CT: Computed Tomography

DAPI: 4',6-diamidino-2-phenylindole

DC-STAMP: Dendritic Cell-Specific Trans-Membrane Protein

ER : Endoplasmic Reticulum

ESC: Embryonic Stem Cells

FACS: Fluorescence-Activated Cell Sorting

F-actin: Filamentous actin

FLPeR: flipase

Gastro: Gastrocnemius

GFAP: Glial Fibrillary Acidic Protein

gl: grey lethal

H&E: Hematoxylin and Eosin

H^+: Proton

H_2O: water

HCO_3^-: bicarbonate

HRP: Horseradish Peroxidase

HSCT: Hematopoietic Stem Cell Transplant

HSV TR: Herpes Simplex Virus Thymidine Kinase

IRO: Intermediate autosomal Recessive Osteopetrosis

LC3: Light Chain 3

Lvr: Liver

MAPK: Mitogen-Activated Protein Kinases

MBP: Myelin Binding Protein

M-CSF: Macrophage Colony Stimulating Factor

MEP: Motor Endplates

MITF: Microphthalamia-Associated Transcription Factor

mnd: motor neuron damage

MRI: Cerebral Magnetic Imaging

mTOR: mammalian Target Of Rapamycin

NADH-TR: Nicotinamide Adenine Dinucleotide Tetrazolium Reductase

NBT: Nitro-Blue Tetrazoluim

NCL: Neuronal Ceroid Lipofuscinoses

NeuN: Neuronal Nuclei

NFATc1: Nuclear Factor of Activated T-cells, cytoplasmic 1

NFH: Neurofilament Heavy chains

NF-M: Neurofilament-Medium

NFκB: Nuclear Factor kappa-light-chain-enhancer of activated B cells

NMJs: Neuromuscular Junctions

OCLs: Osteoclast-like cells

OPG: Osteoprotegrin

Ostm1: Osteopetrosis associated transmembrane protein

p62: sequestosome 1

PCR: Polymerase Chain Reaction

PE: Phosphatidylethanolamine

PIK3C3: Phosphatiylinositol 3-Kinase Catalytic subunit type3

PNS: Peripheral Nervous System

PVDF: Polyvinylidene Fluoride

qPCR: Real-time PCR

RANK: Receptor Activator for Nuclear factor κ B

RANKL: Receptor Activator for Nuclear factor κ B Ligand

RT: Room Temperature

RT-PCR: Reverse Transcription PCR

Sc: Spinal cord

ScC: Cervical Spinal cord

ScL: Lumbar Spinal cord

SMA: Spinal Muscular Atrophy

SMN1: Survival Motor Neuron 1

SOD1: copper-zinc superoxide dismutase

SV2: Synaptic Vesicle 2

SYN1: Synapsin 1

TA: Tibialis Anterior

TCIRG1: T-Cell Immune Regulator 1

TR: Transgenic

TRAP: Tartrate-Resistant Acid Phosphatase

TRITC: Tetra-methylrhodamine

TVA: Transverse Abdominal

UPS: Ubiquitin Proteasome System

V-ATPase or H^+-ATPase: Vacuolar proton ATPase

wt: wild type

Introduction

The human body is a collection of integrated systems that cooperate together to ensure a proper functioning. Some of our indispensable functions that we use daily are movement, breathing, thinking, eating, digesting, and others. The musculoskeletal and the central nervous systems collaborate to generate the required vital actions. Whether it is the commander as the central nervous system or the responder like the muscles, any malfunction would impede this proper functioning.

Neuromuscular diseases refer to a broad group of disorders due to a defect in any of the following organs: brain, spinal cord and muscle. Some of the known neuromuscular diseases are amyotrophic lateral sclerosis (ALS) and spinal muscular atrophy (SMA). Interestingly, the similar pathological phenotypes have been found by mutations in other genes that play an important role in other organs such as the bone. Osteopetrosis associated transmembrane protein (Ostm1) involved in bone resorption is an example of this phenomenon. The common observational pathology of the neuromuscular disease is motor defect, weak muscle strength, and impaired gait. Whether it is only osteopetrosis or neuromuscular diseases, it will hinder the well-being and the continuity of the patients' life. Any disease will put the patient in a state of anxiety and distress. It is only natural that a combination of both neuromuscular disease and osteopetrosis will make the patients' life much harder.

The prognosis of the *Ostm1* linked disease appears particularly poor due the early death of the patient within the first year of age. Comparing to other forms of osteopetrosis, *Ostm1* deficiency is more severe due to several complications that appear in different systems. These complexities will be covered thoroughly through this thesis. Since this gene was also spontaneously and naturally mutated in mice (such as the grey lethal mice (*gl/gl*)), these mice are also expected to have a shorter life span with respect to their normal 2-year life expectancy and comparable to an Ostm1-defecient patient life expectancy.

The limited access of patients such as the limited number and kind of biopsies, the poor characterization of the pathogenesis in animals and the difficulty in applying pre-clinical results on human clinical trials motivates the creation of mouse models for a better understanding of the structure, the physiology and the pathology of the protein.

In the thesis, we focus on the neuronal function of Ostm1 through the generation of a lox allele *Ostm1*$^{lox/lox}$ with a unique and specific neuronal Synapsin Cre^{+} to ensure the conditional knockout of *Ostm1* only in neurons. Specifically, we analyze the mouse growth and the behavioral parameters at the phenotypic level. Then, investigation of the link between the neuronal loss and the locomotion defect is done through the brain, spinal cord neuronal population and neuromuscular junction analysis. Finally, we show that ex-vivo studies aid in quantifying and qualifying the neuronal enriched population using immunochemistry and immunofluorescence with specific markers.

Chapter 1

Literature Review

1.1 The Nervous System

The nervous system is a network of over 100 billion cells that interact, communicate and regulate signals to control different functions and maintain homeostasis [1]. The crucial functions of the nervous system include: sensation and perception, motor function, thinking and planning, memory, regulation of heart rate, endocrine and exocrine glands, breathing, temperature and vasculature, emotions, and balance. These sophisticated functions are governed by two divisions of the nervous system: the central and the peripheral nervous system [2].

1.1.1 Central Nervous System (CNS)

The central nervous system comprises the brain and the spinal cord. The brain is composed of the white matter that consists of myelinated axons and the grey matter that consists of unmyelinated cell bodies and dendrites. The brain structure is made of the forebrain, midbrain, and hindbrain. The forebrain is composed of the diencephalon (the thalamus and the hypothalamus) and the telencephalon that contains the highest-level cognitive processing, the cerebrum. The hindbrain structures are: the brain stem, reticular formations, and cerebellum. The spinal cord protrudes downward from the brainstem. The spinal cord is divided into four parts: cervical, thoracic, lumbar, and sacral. The spinal cord intervenes with most body parts below the neck. The common components between the spinal cord and the brain are grey and white matter, but both differ in localization. In the brain, the grey matter encases the white matter. On the contrary, in the spinal cord, the grey matter lies deeper than the white matter [3].

1.1.2 Peripheral Nervous System (PNS)

The peripheral nervous system comprises nerves that protrude outside the brain and the spinal cord. The peripheral nervous system contains 10 of the 12 pairs of cranial nerves and 31 pairs of spinal nerves. The PNS is the bridge that links the CNS to the rest of the body. Same as the CNS, the PNS could be subdivided into autonomic and somatic nervous system [4].

1.2 Types of Nerves

In order for the body to receive the message and process it, then translate it into an action or a response, there should be different kinds of nerves that carry different tasks. The nervous system is organized into three kinds of nerves which are: sensory, motor and interneurons. The sensory neurons carry sensory information from the receptors to the CNS and are also called afferent neurons. On the other hand, motor neurons transmit the information to the targets (muscle and

glands) from the CNS to the peripheral and are termed efferent neurons. Interneurons are the most abundant type of neurons and are the mediator between the sensory and the motor neurons. They are usually found in the brain and in the spinal cord. The spinal cord contains both axons of the motor and sensory neurons. The sensory information being transmitted by sensory neurons in the sensory area of the cortex or in the spinal cord is integrated in the motor cortex that is the highest level in the motor system. The motor cortex governs the limb movements through the cortico-spinal tract. Some information can bypass this long circuit in case of reflexes where the entire neuronal message occurs in the spinal cord by transmitting the sensory information through the dorsal side which is the back side of the spinal cord, and then the stimulus passes through the motor neurons located in the ventral part of the spinal cord reaching the target, the muscle. The location of the nuclei of these motor neurons specifies the body area which they control. For instance, the lateral nuclei control the limbs which are distally located according to body axis. On the other hand, the medial nuclei govern the proximal muscles [5-7].

1.3 Cells of the Nervous System

The neurons and the glial cells compose the nervous system. These two types of cells are the fundamental blocks of the nervous system where each one has its specific role and structure.

1.3.1 Neurons

Neurons are unique cells capable of conveying the electrical impulses and converting them into chemical signals that are processed by other targets. Neurons are the largest cells with highly precise and polarized structure. Neurons can have a variety of shape that is dictated by the cells which neurons interact with. These shapes determine the function of the neuron, but all share the same organelles as other cells. The soma, which is the cell body, contains the nucleus, the rough endoplasmic reticulum and the ribosomes. Dendrites are the appendages protruding from the soma body. The receiving message passes from the dendrites to the soma body reaching the axon hillock where all the messages are integrated. The message will be converted into an electrical signal that travels through the axon reaching the nerve terminals. To speed up the transmission of the message and the preventing its loss, the axons are insulated with myelin [5].

1.3.2 Glial Cells

Glial cells, also known as neuroglia, support the survival and normal functioning of the neuron. One type of glial cell forms the neuron myelination required for signal transmission. The types of

glial cells are the astrocytes, ependymal cells, microglia, oligodendrocytes and Schwann cells. The astrocytes provide nutrients from the blood brain barrier to the neurons; hence they control the passage of these solutes. The ependymal cells produce the cerebrospinal fluid and line the ventricles of the brain. Microglia cells are the defense cells of the neurons and phagocyte pathogen and debris. The oligodendrocytes and the Schwann cells both produce the myelin, but the former is in the CNS, while the latter is in the PNS [8].

1.4 Neuromuscular Junction

Muscle contraction is an indispensable process required for carrying out our daily tasks such as locomotion and posture. For this contraction to occur, a communication between the muscle and the motor neurons whose nuclei reside in the grey matter should take place through the neuromuscular junctions (NMJs). The motor neuron divides into many branches where each branch forms an NMJ with a muscle fiber. A collection of multinucleated muscle fibers forms a muscle. The region where the motor neuron terminal innervates with the muscle is called end plate. The branches further split into tiny branches to generate the synapse. The pattern of a synapse comprises a presynaptic neuron that contains synaptic vesicles filled with neurotransmitters acetylcholine, and the postsynaptic cell which is the muscle fiber. When acetylcholine is released by exocytosis through the fusion of the synaptic vesicles with the membrane, it binds to the muscle receptors and depolarizes its membrane causing an action potential. This action potential triggers the contraction machinery [9].

1.5 Macroscopic Bone Structure

The bone constitutes approximately 15% of the total body's weight and is considered one of the vital organs in the body [10]. The bone is characterized by its unique conventional functions: it supports and protects crucial organs, serves a niche for hematopoiesis within its cavities, aids in movement and locomotion of the body muscles and maintains homeostasis state of minerals (calcium and phosphate), acid and base [11].

The two types of bone structure are the cortical bone and the trabecular bone, also known as the spongy or cancellous bone. The cortical bone composes 80% of the total adult human skeleton, forms the outer layer of the bone, and is highly dense, durable and resistant for break. On the contrary, the spongy bone makes up the other 20% and is the inner part of the bone. It consists of trabeculae or rod-like structure network allowing a space for the marrow and the blood vessels; it

is less dense and flexible. Red marrow contains the hematopoietic stem cells which form the blood cells, whereas the yellow mater is filled of fat and is inactive [12, 13].

1.6 Microscopic Bone Structure

The bone matrix forms the stiffness of the compact bone. The bone matrix has inorganic and organic components. The inorganic components consist of calcium, phosphate and hydroxide, which harden to make the hydroxyapatite crystals $Ca_{10}(PO_4)_6(OH)_2$. The organic elements are glycoproteins, collagen and other peptides [14]. The bone matrix is organized into units named osteons or Harversian system. Every osteon contains lamellae, concentric circles of bony matrix that surrounds the Harversian Canals. These canals are parallel to the bone while the Volkmann's canals are perpendicular to the bone. Both canals contain the blood and lymph vessels, and nerves. The small spaces between the lamella are called lacunae, which forms the shelter for mature bone cells named osteocytes. Canaliculi are tiny channels that connect the lacunae for the supply of nutrients and waste between the Harversian and Volkmann's canals and the osteocyte [15].

1.7 Bone Remodeling

Although the bone is rigid and static, it undergoes remodeling. Remodeling is a process by which the old bone is replaced by a new one to maintain the rigidity, and healthiness characteristics and functions of the bone [16]. The bone remodeling process is orchestrated by a dual communication between two types of bone cells. One is involved in removing the old bone by the osteoclast. The other, which is an antagonist of the former, adds bone and is called osteoblast.

1.7.1 Osteoblast

Osteoblasts are derived from mesenchymal stem cells. They synthesize the bone matrix. They are cuboidal in shape and express alkaline phosphatase. They are found on the bone surface composing 4-6% of the total resident bone cells and contain many rough endoplasmic reticulum, Golgi apparatus and secretory vesicles [17, 18]. After bone formation, the osteoblasts pass through one of the 3 status: they can die by apoptosis, turn into quiescent bone lining cells found on the bone surface, or encapsulate themselves by their own matrix (collagen type-1, calcium and phosphate) and differentiate into osteocytes [19].

1.7.2 Osteoclast

Osteoclasts are large differentiated post-mitotic multinucleated bone resorbing cells originated from mononuclear progenitors of hematopoietic stem cell lineage. The osteoclasts attach to the bone through filamentous actin and αvβ3 integrins to create a sealing zone or acting ring [20] . The osteoclasts are characterized by two main functional domains: the ruffled border and the basolateral domain. The ruffled border is involved in bone resorption by pumping out protons through the V-ATPase and secreting enzymes like Cathepsin K to the bone surface. The protons (H^+) create an acidic environment with a pH 4-5 in the resorptive lacuna required for the activity of the enzymes. While in return, the active enzyme breaks the organic component of the bone. The degraded products are shuttled by vesicles containing the enzyme tartrate-resistant acid phosphatase (TRAP) to the basolateral membrane to be secreted [21].

Bone resorption and bone formation are two tightly controlled processes (Figure1-1).

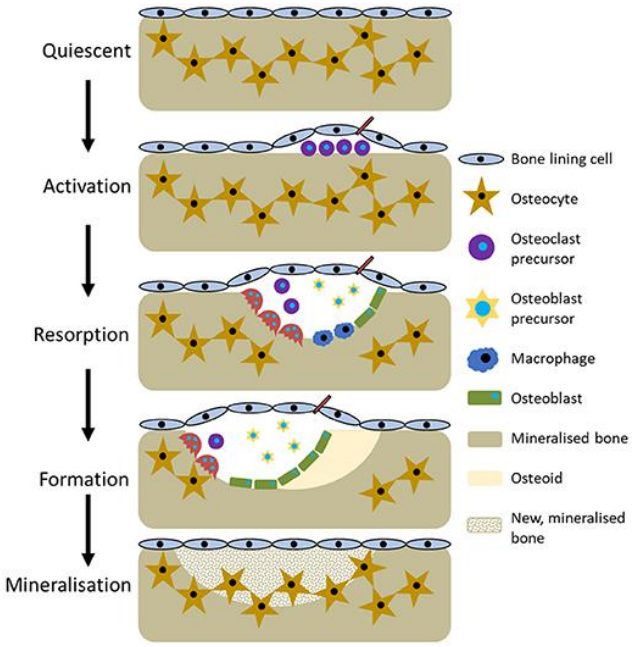

Figure 1-1 Bone Remodeling. Bone remodeling is a continuous process to preserve bone integrity and quality. The osteoclast precursors mature into multinucleated osteoclasts for resorption. Then osteoblasts form new bone in the lacunae. (Reprinted with open-access from Owen and Reilly, Owen, R., & Reilly, G. C. (2018)).

Bone resorption and bone formation are two tightly controlled processes (Figure1-1). The two processes, resorption and formation are called “coupling mechanism”. This coupling mechanism was discovered after researchers figured out in 97% of healthy adults that bone formation followed resorption [22]. Any impaired balance between the two processes could lead to

pathological diseases. For instance, increased osteoclast activity leads to excessive bone resorption, this condition is called osteoporosis and is also the consequence of inflammatory arthritis [23-25]. Osteopetrosis is diagnosed by decreased bone resorption either due to malfunctioning or absent osteoclasts [26, 27]. Other types of Osteopetrosis have normal or increased number of non-functional osteoclasts with increased bone mass [28, 29].

1.8 Osteopetrosis

Osteopetrosis is a heterogeneous family of inheritable bone disorder in which bone resorption is defective due to inefficient osteoclasts. The disease was characterized by a German radiologist Dr. Albers-Schönberg over a hundred years ago through his radiographic analysis from one of his patients with increased Bone Mineral Density (BMD) [30]. Osteopetrosis is characterized by an increase in bone mass that can be detected by an X-ray via the variability of the whiteness, size, and shape. Bone-in-bone appearance refers to the osteopetrotic bone in radiographic images where two bones appear in a single bone due to the increased calcification (Figure 1-2). Some of the symptoms of Osteopetrosis are osteosclerosis that identifies the disease as “marble bone disease”, and decreased bone marrow cavity which causes hematopoietic failure [21, 31, 32].

Figure 1-2 Osteopetrotic Bone. “Bone-in-bone” appearance in the hand phalanges of an autosomal recessive osteopetrosis patient in a radiograph (Reproduced by free-access from Journal of Clinical and Diagnostic Research Bhati, P., & Goyal, P. C. (2017)).

1.8.1 Role of Osteoclast in Osteopetrosis

Anomalies in osteoclasts lead to osteopetrosis. There are two crucial routes for defective osteoclasts which are external and internal defects. The external defect is an environmental abnormality that affects osteoclastogenesis, whereas the internal route is within the Osteoclast

itself. The defect could be within the initial stage (differentiation of hematopoietic cell stage) till the final stage (maturation of osteoclast).

These mutations could be grouped into two categories. The first is the absence of mature osteoclasts due to blocked differentiation. This disease is also known as osteoclast-poor osteopetrosis. The second type, osteoclast-rich, corresponds to deteriorated resorptive function, where there are mature non-functional osteoclasts [33, 34].

Osteoclastogenesis consists of well-organized consecutive steps: (1) determination and commitment of the hematopoietic cell precursor, (2) differentiation and fusion into mature multinucleated osteoclast, and (3) polarization of the multinucleated osteoclasts (Figure 1-3) [35, 36]. One of the important and earliest transcription factors in stimulation of osteoclastogenesis is PU.1 which controls the synthesis of the Macrophage Colony Stimulating Factor (M-CSF) receptor on osteoclast. The monocytes and hematopoietic stem cells differentiate into osteoclast precursor by the binding of the receptor to M-CSF that is produced by stromal cells and osteoblasts (Figure 1-3) [37].

Besides M-CSF, another factor was observed its importance in osteoclastogenesis from the microphtalmia *mi/mi* mouse model study. The *mi/mi* mouse is a mouse model that has mutation in Microphthalamia-associated transcription factor (*MITF*). This mutation results in the failure of osteoclasts fusion, low TRAP expression levels and no resorption of the bone occurs. MITF plays a significant role in early osteoclastogenesis [38].

After M-CSF and MITF stimulation, the Receptor Activator for Nuclear factor κ B ligand (RANKL) on the cellular membrane of osteoblasts interacts with the Receptor Activator for Nuclear factor κ B (RANK) on osteoclast precursor resulting in the induction of many pathways such as mitogen-activated protein kinases (MAPK), nuclear factor kappa-light-chain-enhancer of activated B cells (NFκB), and nuclear factor of activated T-cells, cytoplasmic 1 (NFATc1) (Figure 1-3). The precursor differentiates into mature osteoclast [16, 31-33]. $RANK^{-/-}$ mice, which have recombination in RANK alleles, have an absence of osteoclast, meaning that they are osteoclast-poor. This leads to mice suffering from severe osteopetrosis [39].

In addition to the initiator of osteoclastogenesis, there are also signals that hinder osteoclasts differentiation like Osteoprotegrin (OPG) (Figure 1-3).

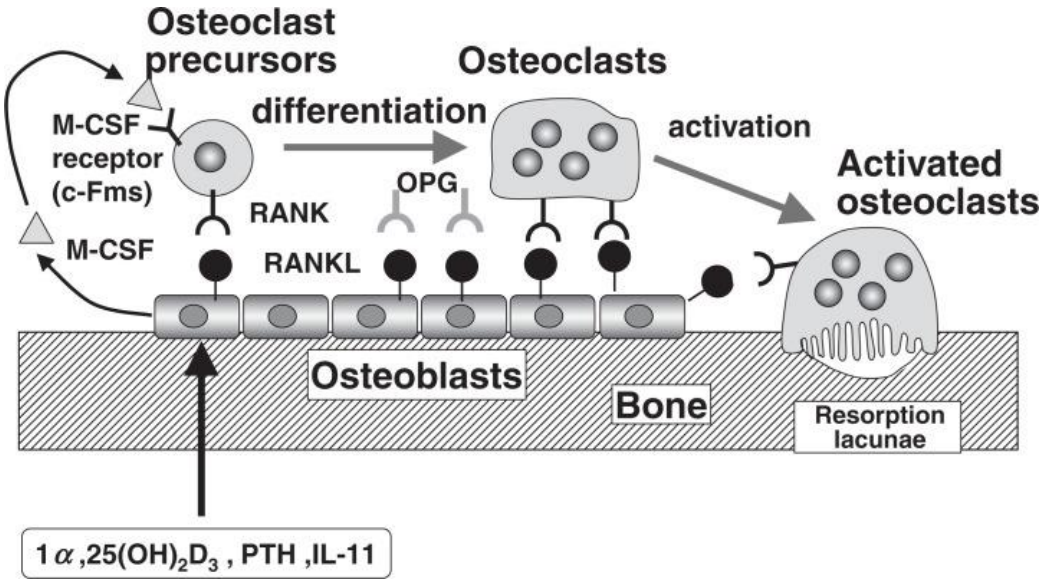

Figure 1-3 Molecules Involved in Osteoclast Differentiation and Maturation. M-CSF has important roles in differentiation. RANK-RANKL interaction controls the late stage of osteoclast differentiation where any anomaly leads to absence of osteoclasts. OPG competes with RANK for RANKL binding and inhibits the interaction. (Adapted with unrestricted access from The Japan Academy, Suda, T., & Takahashi, N., (2008)).

OPG is a soluble protein that competes with RANK for RANKL binding and inhibits the binding of RANK with RANKL [40].The pathways that are activated by RANK-RANL interaction activate the transcription of series of genes important for osteoclast differentiation like dendritic cell-specific trans-membrane protein (DC-STAMP). DC-STAMP plays vital role in the fusion of mononuclear precursors to form multinucleated osteoclast [41]. RANK-RANL interaction initiates the expression of osteoclast markers which are TRAP, calcitonin receptor and integrin αvβ3 [42-44].

Osteopetrosis can still occur even if there is no disruption or mutation in the differentiation of the osteoclast. In other words, maturation of the osteoclast is necessary for bone resorption, and there are many genes that should be transcribed and regulated properly for the osteoclast polarization. The ruffled border formation is one of crucial domains that mature osteoclast should acquire for the breakdown of inorganic hydroxyapatite and organic collagen so lacking this domain results in osteopetrosis. For instance, the grey lethal mouse, which is our lab mice model and our main interest, lacks a developed ruffled border accompanied by an increased number of osteoclasts [45].

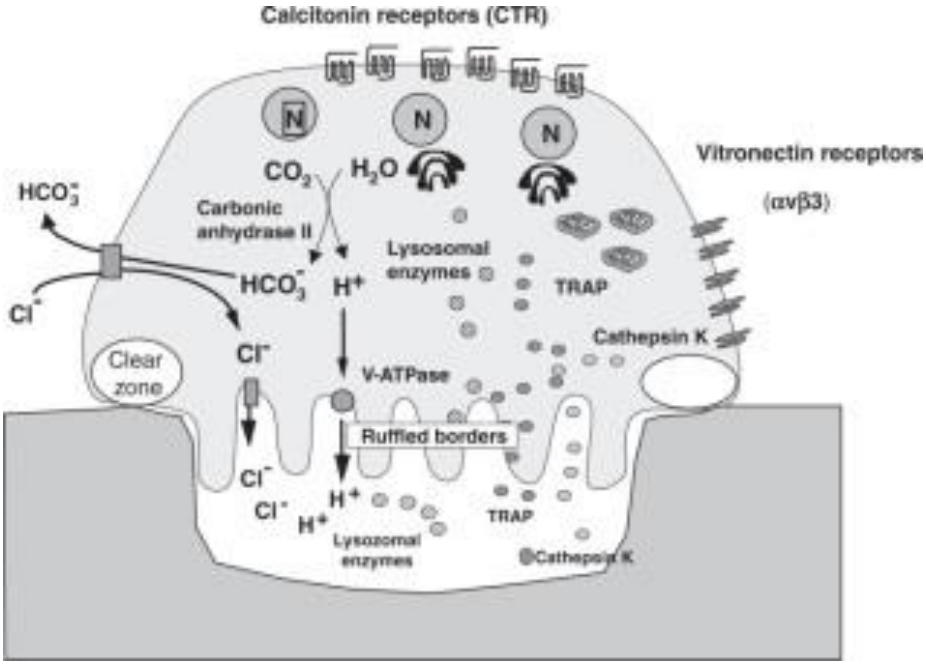

Figure 1-4 Osteoclast Physiology. Osteoclasts attach to the bone surface by αvβ3 integrin to form the resorption lacunae. Proton (H^+) and chloride (Cl^-) are secreted to maintain acidity and electroneutrality respectively. Cathepsin K, one of the enzymes, is also secreted to the resorption lacunae for breakdown of bone matrix. (Adapted with open use from The Japan Academy, Suda, T., & Takahashi, N., (2008))

The acidification of the resorptive lacunae, which is the site between the ruffled border and the bone, should be maintained by the H^+ protons that are released by the osteoclasts for normal function of the digestive enzyme Cathepsin K. In order to preserve that pH, the osteoclasts create a sealing zone/acting ring with the bone by the adherent filamentous actin (F-actin) and the two distinct integrins alpha and beta chains (Figure 1-4) [46].

1.8.2 Forms of Osteopetrosis in Human

Osteopetrosis is classified by the severity of the disease, the age of onset, and the inheritance. The three forms of osteopetrosis are: autosomal dominant osteopetrosis (ADO), intermediate autosomal recessive osteopetrosis (IRO), and infantile malignant autosomal recessive osteopetrosis (ARO) [32, 47].

1.8.2.1 Autosomal Dominant Osteopetrosis

Autosomal Dominant Osteopetrosis is the mildest form of osteopetrosis with the occurrence of approximately 5/100,000 of the population. All patients have normal lifespan [32]. The disease is subdivided into two categories: ADOI and ADOII. ADOI disease has increased bone density by amplified calcification due to overactive osteoblasts and a low number of osteoclasts [48]. The

other group, ADOII disease, is also called Albers-Schonberg disease and is caused by a mutation in the CLCN7 gene. Most of these mutations are missense and lead to non-functional osteoclast with less severe osteopetrotic phenotype compared with other forms of oseopetrosis [49].

1.8.2.2 Intermediate Autosomal Recessive Osteopetrosis

Intermediate autosomal recessive osteopetrosis ranges in a medium severity scale between autosomal dominant osteoporosis and infantile malignant autosomal recessive osteopetrosis. IRO is less frequent and is caused mainly by mutation in carbonic anhydrase-2 gene (*CA-II*). CA-II converts carbon dioxide (CO_2) and water (H_2O) into H^+ and bicarbonate (HCO_3^-). The proton is transported across the ruffled border to acidify the resorption lacuna. Conversion failure of the CO_2 and H_2O leads to osteopetrosis accompanied with renal tubular acidosis and cerebral calcification [33, 50].

1.8.2.3 Infantile Malignant Autosomal Recessive Osteopetrosis

Infantile malignant autosomal recessive osteopetrosis is the most dreadful form of osteopetrosis with an incidence of 1/250,000, and higher in some regions like Costa Rica, the Middle East and The Chuvash Republic of Russia where the rate increases to 3.4/100,00. The disease appears early around 3 months of age. Most of the children die within 4 years due to their weak immune system (infections) [51]. Most of the variable spontaneous mutations end up producing normal to increased number of non-functional osteoclasts that lead to detrimental symptoms on the patient. The increase of osteoclasts number may be a compensatory mechanism for restoring the function. Most of the shared symptoms are growth retardation, delayed psychomotor development, hepato-splenomegaly, micrognathia, delayed tooth development, osteomeoyelitis, osteosclerosis and dense fragile bone filling the bone marrow spaces which results in anemia, leukopenia, and thrombocytopenia [51-53].

Moreover, the increase of bone mass spreads throughout the entire skeleton and one of its severe effects is craniofacial bone anomalies such as nasal obstruction, hydrocephalus and cranial foramina thickening. The tightness of the cranial opening compresses the nerves and leads to blindness and deafness as a secondary effect [53, 54]. Beside the secondary effects, some genes, *CLCN7* and *Ostm1*, primarily affect the central nervous system that will be the main focus of my thesis [55, 56]. The most frequent genetic mutations in ARO patients are in the T-cell immune regulator 1 (*TCIRG1*) gene that codes for a3 subunit of the V-ATPase [57]. Osteopetrotic

patients could be healed by bone marrow transplant, but success rate is not high due to complications such as human leukocyte antigen matching and age of the transplantation. The most successful transplantations are done before the age of 10 years due to the decrease in rate of rejections [33, 58].

1.9 Mutations in ARO

Mutations effects vary from intrinsic to extrinsic. Within the intrinsic part, defects could arise from mutations of differentiation genes like *TNFRSFIIA* that encodes for RANK receptor [59] or from mutations of maturation genes like *TCIRG1*, *CLCN7*, *OSTM1* and *SNX10* (Figure 1-5) [33]. Most of the mutations in the ARO patients are intrinsic, but there are still some extrinsic defects; for instance genetic alteration in *TNFSFII* that codes for protein specialized in cytokine, survival, and osteoclastogenesis functions [60]. Among the intrinsic genes, mutations in *TCRIG1*, *CLCN7*, and *OSTM1* genes are the main causes of ARO in humans and mice and are the most prone to natural spontaneous mutations. These spontaneous mutations help scientists to characterize the genes involved and to create mice models to investigate the effects of these mutations on the entire body. Moreover, mice models can serve as the important step to test the success rate of a treatment prior to trial in humans.

1.9.1 *TCIRG1*

TCIRG1 mutations score more than 50% of all mutation in ARO disease [33]. *TCIRG1* encodes for a3 subunit of the Vacuolar proton ATPase (V-ATPase or H^+-ATPase) with a mass of 116 KDa. V-ATPase is located on many intracellular compartments, endosomes, lysosomes and the ruffled border of a mature osteoclast. Its main duty is to acidify the lacuna by pumping H^+ in the compartments creating a pH gradient. The V-ATPase is made up of two domains, V1 and V0. V1 is a cytosolic domain composed of eight subunits (A-H) and responsible of ATP hydrolysis by A and B subunits [61]. The other subunit, V0, is a trans-membrane domain where protons are pumped through a, c, c", d, e and the accessory subunits Ac45 and M8-9 [62, 63]. The "a" subunit has 4 isoforms, a1, a2, a3, and a4. Osteoclasts only express the a3 subunit, so any mutations in the *TCIRG1* will prevent the embedding of the V-ATPase in the plasma membrane that will result in osteopetrosis [64]. The oc/oc mice model with 1.6 kb deletion in *TCIRG1* gene including the start site dies within 3-6 weeks due to non-functional osteoclasts (Figure 1-5) [65].

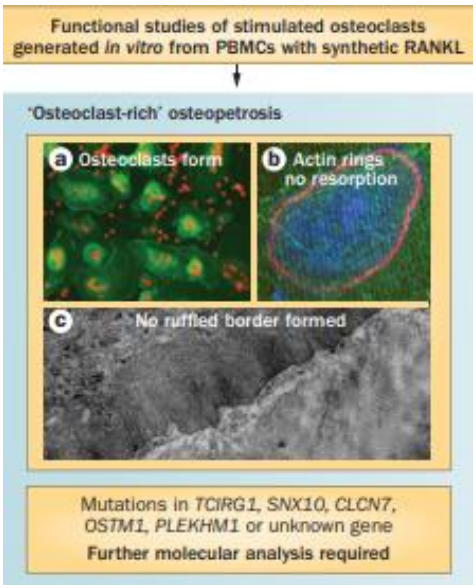

Figure 1-5 Diagnosis and Mechanisms Underlying Osteoclast-Rich ARO. (a) Vitronectin receptor (green) and nuclei (orange) staining cultured osteoclast. (b) Undamaged F-actin ring identified by TRITC-phalloidin (red) on a mineralized substrate (green) were seen in osteoclast. (c) Osteoclast lacking ruffled border at the interface site with the bone (Adapted with permission from Springer Nature, Nature Reviews Endocrinology, Sobacchi, Schulz et al. 2013).

1.9.2 *CLCN7*

CLCN7 mutation ranks the second more common mutation with percentage of approximately 15% of all ARO mutations. The *CLCN7* encodes for 89 kDa chloride/proton exchanger [55]. During osteoclast polarization, lysosomes containing the CLCN7 protein and others are fused with the cellular membrane forming the ruffled border. CLCN7 maintains the charge balance in the lacuna by expelling protons coupled with chloride ions [66].

The CLCN7 deficient mouse model, which has a point mutation in the *CLCN7* gene, is osteopetrotic. Although it was found to have normal lysosomal pH, there was disruption of electroneutrality due to low chloride ions. CLCN7 deficient mouse model have drastic lysosomal accumulation in the hippocampal and the cortical neurons, revealing the role of CLCN7 in trafficking by the chloride ion concentration modulation [67].

Clcn7 knockout mice models (*Clcn7*$^{-/-}$) displayed severe neuronal and retinal degeneration beside to osteopetrotic symptoms. These mice had a very short life span and died within 7 weeks [68]. Kasper et al. (2005) wanted to cure this osteopetrotic phenotype by creating transgenic gene *CLCN7* under the regulation of TRAP promoter. This TRAP-*Clcn7* mice model had normal bone size, shape and density, but it still showed neuronal abnormalities and visual impairment. This phenotype revealed similar features of neuronal ceroid lipofuscinoses (NCL) by accumulation of

avacuolar lipopigments, and granular osmophilic deposits in the perikarya of hippocampal and cortical neurons. An intense activation of astrocytes and microglia occurs in the cortex and the hippocampus. Their life span was extended by 3 weeks. Kasper and his colleagues concluded that the loss of CLCN7 primarily affects the central nervous system unlike other osteopetrotic genes such as *TCIRG1* where the neurological compression with no neurological anomalies was a secondary effect due to bone mass increase [69].
This suggests that certain genes regulating osteoclast function can play additional important roles in other tissues including the brain.

1.9.3 *OSTM1*

OSTM1 is the central point of this thesis. 4-6% of the patients suffer from *OSTM1* mutation with severe symptoms [33]. *OSTM1* gene has 6 exons and codes for Osteopetrosis associated transmembrane protein (Ostm1) that is a type I trans-membrane protein. The immature Ostm1 protein with a mass of 34 kDa is post-translationally modified and highly N- glycosylated to reach a mass of 60 kDa. Ostm1 is localized within endosomes/lysosomes by being synthesized in the endoplasmic reticulum (ER), and trans-Golgi network [70]. Ostm1 is the β-subunit of CLCN7 (Figure 1-5). Ostm1 and CLCN7 mutually rely on each other. Ostm1 needs CLCN7 to be shuttled from the ER to the lysosome, on the other hand Ostm1 maintains the stability of CLCN7 through its proper binding [71].
OSTM1 mutations are considered the most severe due to early age onset of ARO symptoms where patients die within the first year that is considered a short life period [72]. The classic osteopetrotic phenotype from which human patients suffer is increased bone mineralization. The endochondral ossification is disrupted where neither bone resorption nor detectable cartilage is seen. The robust trabecular bone growth leads to the progression of the disease affecting many organs and tissues [73]. These patients develop bone marrow suppression that results in all blood cell type deficiencies (pancytopenia) and increased infection susceptibility. The suppression stimulates the extramedullary hematopoiesis in the spleen and the liver; thus, it undergoes abnormal enlargement (hepatosplenomegaly). In addition, visual and neuronal degeneration occurs which will be discussed in depth later in the thesis [73].

1.10 Ostm1 Partners

Ostm1 null mice had impaired melanosome dispersion, lysosome lacking fusion ability with plasma membrane, and accumulated neuronal vesicular structures (metabolites and autophagosomes). The multiple roles of Ostm1 and its most severe phenotype in ARO highlight the presence of interacting partners. Mimicking the physiological conditions in the cell lines ensures the same interaction as *in vivo*. Affinity purification and mass spectrometry experiments identified 16 unique Ostm1 interacting proteins. These included kinesin motor KIF5b, present in high amounts, but also protein remodeler EDD1/UBR5 and nuclear pore importin KPNB1. These results were consistent with GST pull down assay and co-localization experiments. Due the movement of the kinesin motor protein, a live time lapse imaging examined the dynamic co-localizations of the fluorescence (Figure 1-6) [70].

Moreover, Ostm1 perinuclear colocalization supports its interaction discovery with KPNB1/Importin β1 which participates in nucleocytoplasmic trafficking [70, 74]. This evidence depicts a role of Ostm1 in cargo and organelles shuttling as an adaptor in the KIF5B complex throughout the impaired osteoclast, melanosomes and neuronal cells in the *gl/gl* mice.

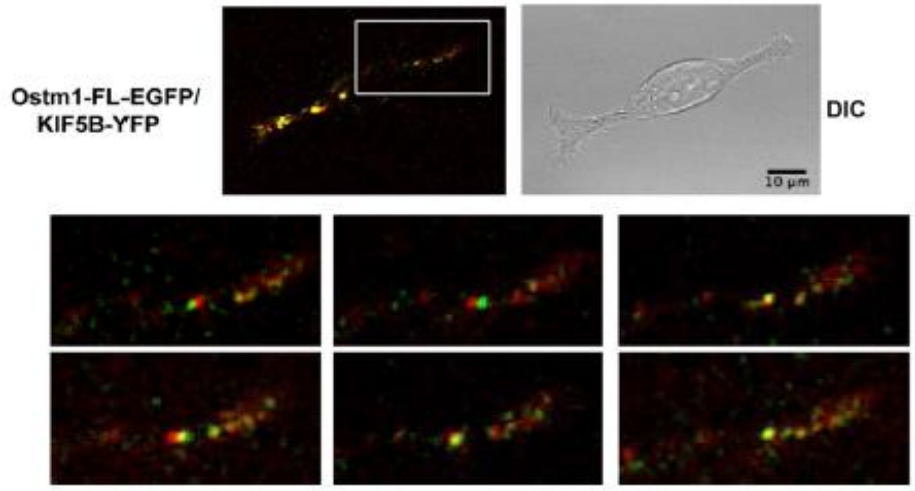

Figure 1-6 Identification of Ostm1 Partners. Time lapse confocal microscopy images of EcR293 cells showed co-localization of Ostm1-FL-EGFP and KIF5B-YFP (Adapted with permission from American Society for Microbiology, Molecular and Cellular Biology. Pandruvada, Beauregard et al. 2016).

1.11 Osteopetrosis and the Central Nervous System

In addition to the suppression effect of bone mass increase on the bone marrow cavity, the aberrant bone mass increase compresses the main processor, the brain. Some patients experience abnormally large thickened head, known as macrocephaly, and cranial foramina narrowness that accumulates the cerebrospinal fluid (CSF) and compresses the blood vessels and nerves passing through respectively. As a result, deafness and blindness can occur [75]. These secondary effects could be erased by treating the primarily effect which is osteopetrosis. The malfunctioning osteoclasts could be substituted by hematopoietic stem cell transplant (HSCT) where the patient returns into a healthy life afterwards [33, 58].

As described above, neuronal compressions are marked as secondary effect like mutations in *TCIRG1* [72]. However, genes with multifunction and multi-organ expression such as *CLCN7* and *Ostm1* cannot be completely cured by HSCT. As seen above, the autonomous role of *CLCN7* in the CNS had a primary effect rather than a secondary effect upon restoring bone remodeling in the TRAP-*Clcn7*. Other treatments should be added to HSCT for a full rescue.

Concerning Ostm1 and the CNS, our lab reported neuronal defects in brain of the *Ostm1* mutant mice with transgenic bone rescue. These findings indicate that with normal bone mass growth the mice suffered from neurodegeneration. Hence, the loss of Ostm1 has a primary effect on the neuronal system rather than a secondary effect. [56].

1.11.1 Case Studies

The first *OSTM1* related ARO patient was reported by Chalhoub et al (2003). This Italian patient expressed shorter *Ostm1* RNA due to skipping exon five of the (*Ostm1*) gene [76]. Another ARO patient with *OSTM1* mutation was examined thoroughly in our lab. Sequencing was done and the results displayed nonsense mutation in exon one where T substituted G generating a stop codon [73].

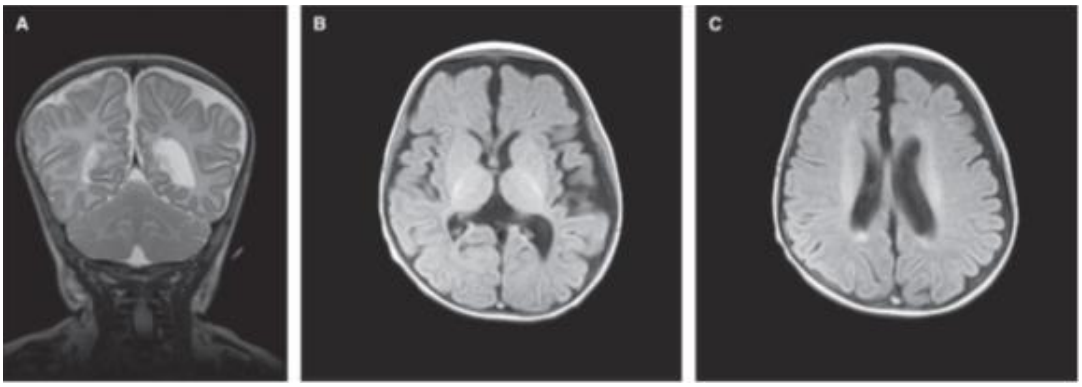

Figure 1-7 *OSTM1*-Related ARO Patient Cerebral MRI. (A) Coronal T2 displaying sub-ependymal heterotopias, delayed myelination and global atrophy (B) Axial T1: sub-ependymal heterotopias (C) Axial T1 showing sub-ependymal heterotopias (Reprinted with permission from John Wiley and Sons, Journal of Bone and Mineral Research, Maranda, Chabot et al. 2008)).

This sequence also transcribed a shorter RNA and translated a putative truncated protein lacking the trans-membrane domain, so this protein will be either degraded or secreted by the cell [70, 71]. The patient had non-functional osteoclasts that led to an increase in bone mineral density. The patient suffered from eyesight impairment and seizures at 4 months age.

The complication of these initial symptoms led to an early death at 1 year of age and was accompanied by neurological defects. The patient lacked any cranial protrusions which indicated that the neurodegeneration was not a secondary effect. Cerebral magnetic imaging (MRI) (Figure 1-7) results revealed cerebral atrophy, delayed myelination, and bilateral atrial subependymal heteropias. Heteropias in this case was the protrusion of gray matter into the ventricles [77]. This abnormal delocalization is a sufficient evidence of abnormal neural growth. Computed tomography (CT) scan showed neither auditory nor optic nerve compression which also confirmed the primarily role of Ostm1 in neuronal function [73].

Taking all these novel *OSTM1* patients into consideration and for a deep and further understanding of Ostm1 role, generating a mouse model mirroring these patients would be an ideal approach to get a better understanding of the role of Ostm1 and its disease prognosis. Mice models help to target and tackle the gene function in the entire body or in a specific organ and tissue in order to identify the mechanism of action and to aid scientists in creating an efficient treatment.

1.12 Grey lethal mouse model

The grey lethal mouse (*gl*) is a mouse model having osteopetrotic syndrome. These mice are named grey-lethal due to their grey coat color instead of an agouti color and the *gl/gl* mice live up to 3-4 weeks [76]. The color defect is not due to agouti gene mutation but due to an accumulation of pheomelanin granules in the melanocytes [78].

In the last decade, several molecular and cellular researches have been done on the *gl/gl* mice to detect the role of Ostm1. One of these investigations was contributed by Prinetti et al. (2009) [79] where they tried to depict the function of Ostm1 from the brain composition. Ostm1 and ClCN7 form a complex that embeds in the endosomes and lysosomes of different cells including neuronal cells. Mutation in either genes results in lysosomal storage and neuronal defects beside to osteopetrosis. These *gl/gl* mice had smaller diffused translucent brain hemispheres with respect to the wild type (*wt*). Dissecting the brain showed loss of neuronal demarcation between the grey and white matter. These preliminary results reveal hypomyelination (myelin loss) [72]. To understand the nature of the neuronal prognosis, the biochemistry of the brain should be analyzed. Brain immunohistochemical images staining of myelinated fibers and oligodendrocytes displayed lack of myelin in hippocampus, and a decrease of myelin in thalamus, and in the cortex [79]. To determine the reason of myelin decrease, the myelin components, galactosylceramides, sulfatides, and sphingomyelin, were tested. In addition to myelin elements, gangliosides, glycerophospholipids, and cholesterol were screened to complete the biochemical analysis. Both cholesterol and glycerophospholipids were the same in the *gl/gl*, and wild type, whereas, the monosialogangliosides GM3 and GM2 scored a gradual increased percentage from day 8 to 12. In contrast to the increase which maybe the trigger, the *gl/gl* mice suffered from 50% decrease in galactosylceramide, sulfatide and sphingomyelin which explains the reason of myelin decrease and fragmentation. Extrapolating the cause behind neurological impairment where the lysosome storage could occur, Prinetti, A. et al. (2009) [79] hypothesized that the accumulation of gangliosides could be the effect of lysosomal defect. After the cultural fibroblast experiments that showed normal lysosomal enzyme activity, studies are still being pursued to test whether the demyelination is the effect of oligodendrocytes or secondary to neuronal pathology. This pathology does not resemble the Krabbe disease, which is an inflammatory disease caused by the defective galactosylceramiadse, but shares the concept that the accumulation of substrates causes toxicity and neurodegeneration. The piling of

galactosylsphingosine, substrate of galactosylceramiadse, stimulates apoptosis of oligodendrocytes and macrophage engulfing [80]. The accumulation of certain sphingolipids that constitutes the lipid rafts could modulate the cellular signal and also disturbs the organization of the plasma membrane that would initiate neurodegeneration. For instance the amyloid precursor protein (APP) in Alzheimer disease and synuclein in Parkinson disease both seem to be located in the lipid rafts [79, 81-83].

Moreover, bone remodeling is disrupted leaving a severe impact on itself and on many organs. The increased bone mass and the piling of trabeculae in the bone marrow space lead to its suppression. Hematopietic defects are generated and produce different blood cell type diseases, anemia and lymphopenia. In the lymphopenia category, B lymphocytes and $CD4^+CD8^+$ double positive T cells decrease in number and the single positive $CD4^+$ and $CD8^+$ T cells undergo an increase in population suggesting an alteration in the differentiation trend [84]. Beside increased BMD, these mice exhibit no teeth due to a blocked tooth eruption held by malfunctioning osteoclasts [45, 84].

Moving to cellular and subcellular pathology, TRAP staining showed that the osteoclast number in *gl/gl* mice is increased and their cytoskeletal organization was damaged and formed a defective ruffled border compared to *wt* [45].

Switching from phenotypic analysis to genomic study, our lab isolated and characterized the *Ostm1* gene responsible for the spontaneous recessive grey-lethal (*gl*) mutation [76]. The spontaneous *gl* mutation is a deletion type mutation in the promoter, exon 1 and 3 kb of the first intron. The deletion shortened the 23 kb *OSTM1* genomic DNA by approximately 7.5 kb. This resulted in the absence of RNA and protein (Figure 1-8) [76].

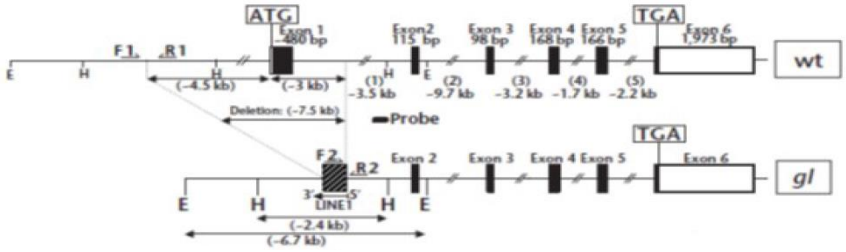

Figure 1-8 Schematic DNA Structures of the Wild-Type and the *gl* Mutant *Ostm1* Gene. Wild-type *Ostm1* gene is approximately 23 kb with 6 exons and 5 introns. The *gl* mutation corresponds to a deletion of 7.5 kb which covers the exon 1 with the start site and 3 kb of first intron (Reprinted with permission from Springer Nature, Nature Medicine, Chalhoub, Benachenhou et al., (2003))

Analysis of *Ostm1* expression was run by our lab on different organs, and it was found that Ostm1 is present in several tissues and organs such as: liver, spleen, kidney, melanocyte and brain, in addition to the bone [76].

Adding up to the spontaneous exon 1 mutation in *gl* mice and in ARO patients, mouse Ostm1 protein is 83% homologous to the human Ostm1 protein [76]. All these evidences create an opportunity to develop a transgenic mouse model for a deep understanding of the Ostm1 mechanism and a translation of preclinical treatments into clinical trials on human.

1.13 PU.1 Transgenic Mice

Our lab wanted to cure these abnormal multinucleated osteoclasts by creating a transgene. *Ostm1* transgene was coupled to a TRAP promoter (Trap-*Ostm1*) to target mature osteoclast, but unfortunately the Trap-*Ostm1 gl/gl* mouse ended up displaying osteopetrotic syndrome as in *gl/gl* [84], unlike the *Clcn7*$^{-/-}$ model that was corrected with TRAP-*Clcn7* transgene [85]. Therefore, Ostm1 seems to play an essential role in the early hematopoietic lineage. Trying another attempt with promoter PU.1 expressed at an early stage of hematopoietic differentiation, the PU.1-*Ostm1 gl/gl* mice were temporarily rescued. The PU.1 regulatory region includes an enhancer sequence 14kb upstream from the promoter site, and in order to include all this genomic DNA in the transgene for a proper transcription, a bacterial artificial chromosome (BAC) was used [84, 86]. PU.1-*Ostm1* BAC was generated from isolating the PU.1 BAC clones containing Tbp1 from 129Sv mouse pBelo11 BAC genomic library [84]. The pLD53.SC1 vector constructed with two homologous regions underwent homologous recombination with the original PU.1 BAC containing the *Tbp1* gene to excise the *Tbp1* gene creating BAC PU.1Δ *Tbp1*.

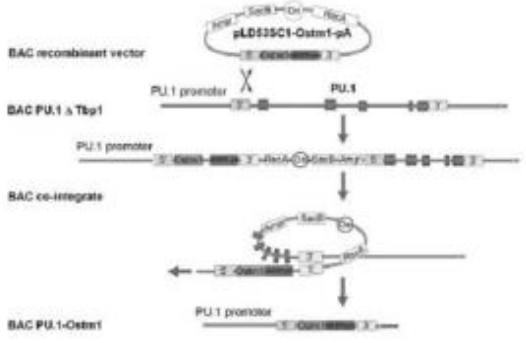

Figure 1-9 Creation of PU.1-*Ostm1* Transgene and Rescue of Osteopetrosis in PU.1-*Ostm1-gl/gl* mice. A schematic representation showing the BAC PU.1-*Ostm1* from BAC PU.1 Δ*Tbp1*. (Adapted with free access from the Journal of Biological Chemistry Pata, Héraud et al. 2008)

Then another pLD53.SC1 cloned with *Ostm1* ORF and polyA sequence inserted between PU.1 5' and 3' was swapped by the homologous recombination sites of the BAC PU.1Δ *Tbp1* to remove the *PU.1* gene keeping its promoter (Figure 1-9) [84].

Surprisingly, these mice survived a longer life span than the *gl/gl* mice, 6-8 weeks, but didn't achieve the normal 2-year life span. Looking at the advantages of this PU.1-*Ostm1* transgene, these mice had normal tooth eruption, bone modeling and remodeling, and recovery of normal bone marrow cavity size that ensures normal hematopoietic stem cells growth (Figure 1-10) [84]. Moreover, to ensure that the hematopoiesis differentiation process was normal, the number of myeloid and lymphocytes cells was counted, and it was the same as in the case of wild type using fluorescence-activated cell sorting (FACS) [84].

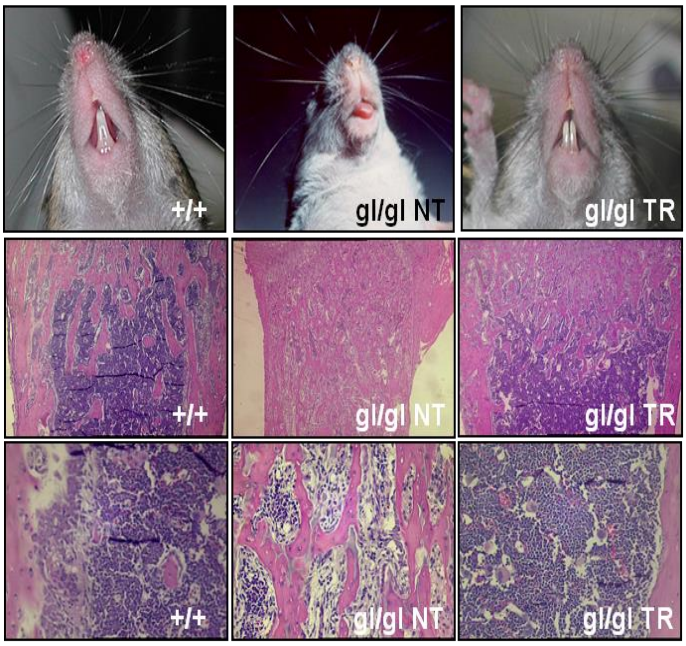

Figure 1-10 Bone and Hematopoietic Phenotypes of *gl/gl* and PU.1-*Ostm1-gl/gl* Mice, and Rescue of Osteopetrosis in PU.1-*Ostm1-gl/gl* Transgenic (TR) Mice. *gl/gl* mice lacked tooth eruption and have reduced bone marrow that is rescued in transgenic PU.1-*Ostm1-gl/gl* mice. Top panel reveals tooth growth and the two bottom panels display bone marrow development in the bone with Hematoxylin and Eosin (H&E) staining. (Adapted with free access from the Journal of Biological Chemistry, Pata et al., 2008).

Through subsequent analyses and knowing that *Ostm1* is highly expressed in the central nervous system, histological examination was done on the PU.1-*Ostm1-gl/gl* mice. Severe brain atrophy was marked by neurodegeneration and rapid onset of astrogliosis and microglial inflammation. The microglial cells were observed in a phagocytic state with Iba1-Ca^{2+} binding protein staining. The astrocyte population was quantified in the hippocampus and cerebral cortex in the PU.1-

Ostm1-gl/gl mice and wild type (+/+). In the hippocampus, there was no significant difference at 3 weeks then it drastically increased by 7 folds at 5 weeks. On the contrary, the cortex showed a high astrocyte peak of 4 folds at week 3 in the PU.1-*Ostm1-gl/gl* mice with respect to the wild type where it kept increasing reaching 30 folds at 5 weeks. Brain sections immunostaining detected neuronal loss in the CA3 and the CA2 layers of the hippocampus and thinning in the 4 cerebral cortex layers (Figure 1-11). Further investigation showed trafficking of carbohydrates, ubiquitinated proteins, and lipids, especially in the axons. Double membrane inclusion bodies number was increased and represented an accumulation of autophagosomes [56].

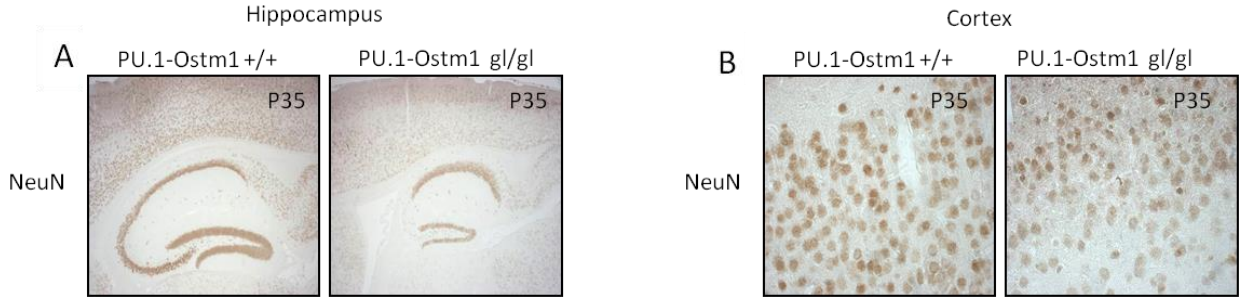

Figure 1-11 Neurodegeneration and Cerebral Atrophy in PU.1-*Ostm1-gl/gl.* (A) Hippocampal neurodegeneration in PU.1-*Ostm1-gl/gl* detected with NeuN staining on brain sections. (B) Cortical neuronal loss in PU.1-*Ostm1-gl/gl* visualized by NeuN staining on brain cortex sections. (Reproduced with free access from the Journal of Biological Chemistry, Héraud, Griffiths et al. 2014)

Besides the function of Ostm1 in the early and the late stage of hematopoiesis including myelopoiesis and lymphopoiesis where there is a required crosstalk mechanism in osteoclast stimulation and activation, and osteoclastogenesis, Ostm1 has another independent role in the neuronal physiology which will be discussed in my thesis.

1.14 Autophagy

Autophagy is a cell cleaning process where toxic, malformed, and non-functional products are recycled in the cell. Autophagy relies on the formation of phagophores (double membrane vesicles), engulfing the cytoplasm constituents including proteins targeted for degradation, fusion with lysosome, and finally degradation of the material to produce amino acids, free fatty acids and nucleotides. This series of steps makes the autophagy which is also called macroautophagy [87]. Several studies extrapolated several involvements of autophagy. Some of these involvements were in starvation, anti-aging, tumor suppression, cell death and development. Autophagy is regulated by nutrient sensors such as the mammalian target of rapamycin (mTOR) which inhibits autophagy during nutrient abundance [88]. Phagophores,

originated from plasma membrane and ER, undergo initiation and nucleation upon phosphatiylinositol 3-kinase catalytic subunit type3 (PIK3C3) (known as VPS34) binding within the complex containing beclin 1 (BECN1) and autophagy-related protein 14 (ATG14). Upon complex formation, two ubiquitin-like steps lead to phagophore elongation. First, the binding of ATG7 and ATG10 conjugates ATG12 with ATG5. The second step involves the cooperation of ATG7 and ATG3 to cleave microtubule-associated protein 1 light chain 3 (LC3)-I into LC3-II. The product of the first step, LC3-II, bound to phosphatidylethanolamine (PE) is recruited to the membrane. While LC3-II on both sides of the phagophore is closing the double membrane, it recruits sequestosome 1 (p62) bound to ubiquinated proteins for degradation. Once the phagophore is closed, it is called autophagosome. The final stage for the recycling of the constituents is the fusion of the autophagosome with the lysosome (Figure 1-12) [89].

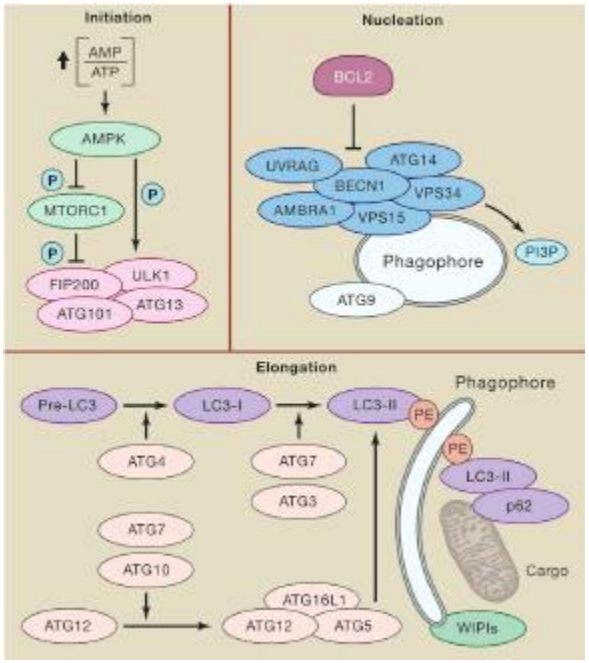

Figure 1-12 Autophagy Pathway. Autophagy starts by an initiation process through direct activating phosphorylation of ATG 13 and ULK1 complex or by an indirect activating dephosphorylation of mTOR. Next, a nucleation step occurs by multiple proteins binding the phagophore. Reaching the elongation step where two ubiquitin-like processes result in LC3-II binding the phagophore. These cause the enclosure of the phagophore (Adapted with permission from Elsevier, Cell, Galluzzi, L et , 2019).

The reason for neuronal death in PU.1-*Ostm1-gl/gl* mice was unknown; the cell usually commits one of the following pathways for its death: apoptosis, autophagic cell death or necrosis [90]. Apoptotic mechanism was tested through tunnel assay where only few cells were revealed to be positive, indicating that the cells are dying by one of the other two mechanisms. Intracellular

analysis was done on these neurons to define their pathology based on other neurodegenerative disorders. Abundant accumulation of carbohydrates and lipid stained with periodic acid-Schiff and Oil Red O, respectively, was seen indicating a hampered trafficking of intracellular metabolites that represents an impaired autophagy mechanism (Figure 1-13) [56].

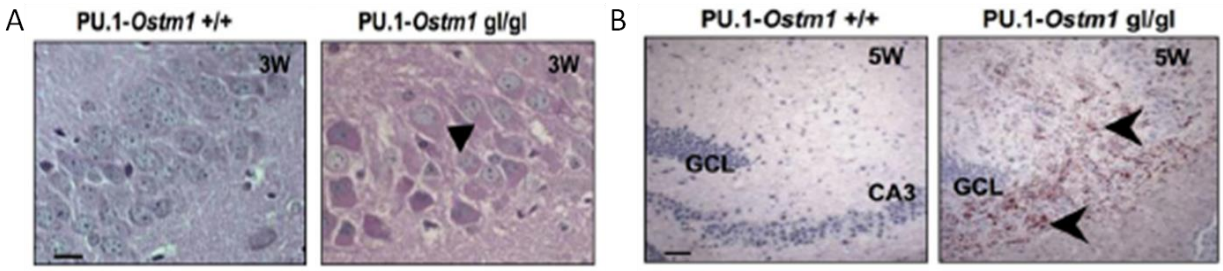

Figure 1-13 PU.1-*Ostm1 gl/gl* Mice Neurons Displaying Carbohydrates and Lipids Accumulation. (A) Comparison of carbohydrates storage in the CA3 layer of hippocampus in each of 3 weeks old PU.1-*Ostm1 gl/gl* and PU.1-*Ostm1* +/+ mice where *arrowheads* in PU.1-*Ostm1 gl/gl* indicate an enhanced amount of carbohydrates with periodic acid-Schiff staining. Scale bar, 20 μm. (B) 5 weeks old PU.1-*Ostm1 gl/gl* mice hippocampus frozen sections displayed high lipid quantity annotated by *arrowheads* relative to PU.1-*Ostm1* +/+. Scale bar, 50 μm. (Reprinted free access from the Journal of Biological Chemistry, Héraud, Griffiths et al. (2014)).

To validate the above evidence, mTOR that regulates the autophagy pathway was monitored. The total brain extracts of PU.1-*Ostm1 gl/gl* contained 30-40% less activated phospho-Akt and phosphor-mTOR with respect to the control extracts [56]. This alteration stimulates an increase of autophagy that will be more investigated by specifics markers in the results chapter.

1.5.2 Rescue of Neurodegeneration in Double Transgenic Mice

The fact that *Ostm1* is highly expressed in the brain and knowing which cells express Ostm1, helped in identifying the reason of the prognosis. Astrocytes, microglia and neurons were found to express Ostm1 using qPCR analysis. Our lab questioned whether the inflammatory response was directly responsible for the phenotype or indirectly resulted from neuronal defect [56]. To address this question, another transgene should be expressed concomitant with the PU.1 *Ostm1* for a full rescue. A double transgenic PU.1-*Ostm1*-GFAP-*Ostm1-gl/gl* and PU.1-*Ostm1*-SYN1-*Ostm1-gl/gl* were generated from crossing PU.1-*Ostm1- gl/+* mice with GFAP (Glial Fibrillary Acidic Protein)-*Ostm1* transgenic founders to target astrocytes and from crossing PU.1-*Ostm1-gl/+* mice with Synapsin 1 (SYN1) Ostm1 transgenic mice to target neurons, respectively [56]. Only the PU.1-*Ostm1*-SYN1-*Ostm1-gl/gl* revealed a full rescue in these mice that survived after

6-7 weeks and showed an indistinguishable CNS structure from the controls by MRI (Figure 1-14) [56].

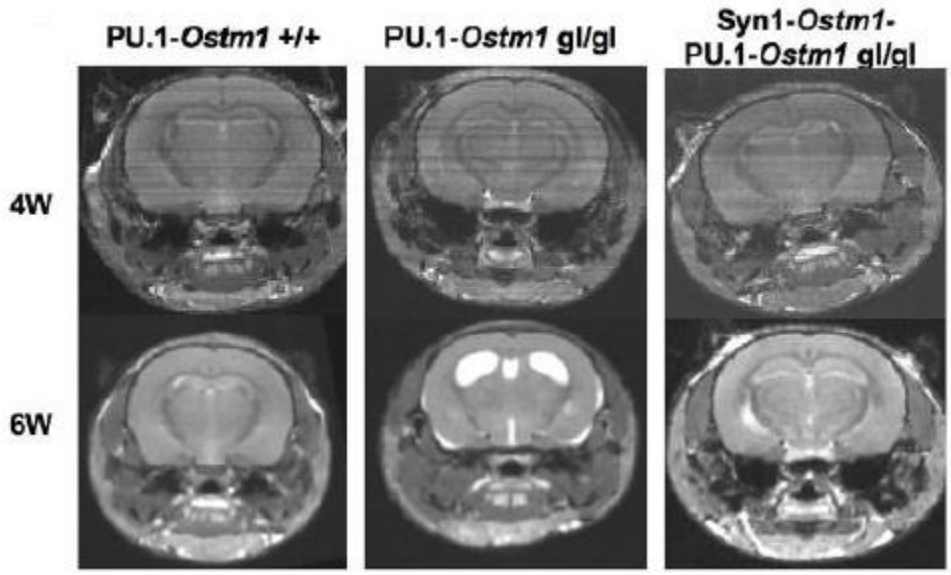

Figure 1-14 SYN1-*Ostm1* Transgene Rescued the Cerebral Atrophy and CNS Degeneration. MRI scan of 4-week-old and 6-week-old PU.1-Ostm1 +/+, PU.1-*Ostm1 gl/gl*, and PU.1-*Ostm1*-SYN1-*Ostm1 gl/gl* brain. PU.1-*Ostm1*- SYN1-*Ostm1 gl/gl* exhibited full brain size and morphology as in PU.1-*Ostm1* +/+ (Reprinted free access from the Journal of Biological Chemistry, Héraud, Griffiths et al. (2014)).

Therefore, one can conclude that Ostm1 loss primarily impacts neurons rather than a combination of cells and plays a crucial role in regulating cellular metabolites in neurons.

Hypothesis and Approach

The unexpected death of the PU.1-*Ostm1- gl/gl* mice after 6-7 weeks with full bone and hematopoietic cell recovery triggered and unraveled further analysis of organs expressing Ostm1 [49]. In addition, the neurological complications that human *OSTM1* related ARO patients suffered from revealed a prominent autonomous role of Ostm1 in the CNS [67]. To decipher the function of the protein from the pathological context compared to the normal one, a conditional neuronal loss of function has been produced. Cre–lox system was used to abrogate Ostm1 in the neurons excluding other organs and systems by introducing lox sites to the *Ostm1* allele that will be excised by neuronal specific SYN1-Cre deleter transgenic mice. Then, we analyzed the phenotypic changes for the mouse growth to determine the role of Ostm1 in the neuronal system and whether neuronal Ostm1 loss has secondary effects on other systems.

Chapter 2

Materials and Methods

2.1 Mice

All the procedures and protocols were approved by the Local Institutional Animal Care and Use Committee and followed the guidelines of the Canadian Committee for Animal Protection (Appendix 1). All the mice were supplied with tap water ad libitum and laboratory chow. They were sheltered in 12-hour light/dark cycle at temperature of 22-26 ºC. All the mice were backcrossed on a C57BL/6J background for at least 10 times.

2.1.1 Grey-Lethal Mice

The mouse strain GL/Le *dl*^{J}*+/+gl* was obtained from the Jackson Laboratory, and this strain was maintained by crossing brothers with sisters.

2.1.2 Ostm1 Floxed Mice

To mirror the Italian patient who had a skip of exon 5 [70], a mouse model with loxP sites in the introns surrounding exon 5 was generated. When Cre was expressed, it excised the flanking regions of exon 5 resulting in Ostm1 protein lacking the trans-membrane domain that will be either degraded or secreted. Two lines were created KO237 and KO195 and the latter was analyzed in depth.

2.1.3 SYNAPSIN-1 Cre Mice

The SYNAPSIN-1 Cre mice (SYN1-cre) only expressed the Cre recombinase in the neurons. This mouse strain B6.Cg-Tg (SYN1-cre) 671Jxm/J was obtained from the Jackson Laboratory.

2.1.4 Genotyping

The tail biopsies were lysed with buffer (50 mM Tris-HCl (pH 8), 100mM EDTA (pH 8), 100 mM NaCl, 1% SDS) and with 150 µg of Proteinase K for an overnight in 55º C incubator. Then, DNA precipitation occurred by adding 5 M NaOH and 100% Ethanol followed by resuspension in TE buffer (100mM Tris-HCl (pH 8), 1mM EDTA (pH 8)).

After extracting the DNA, polymerase chain reaction (PCR) reaction steps took place where 0.1 – 0.5µg of DNA was added in the PCR buffer reaction (10 mM Tris-HCl pH 8.3, 50 mM KCl and 1.5 mM MgCl2) along with 12 µM primers (table 1), 1.25 mM dNTP and Taq polymerase. The mixture underwent 35 PCR cycles that are comprised of 94º C for 30 seconds, 63º C for 30 seconds, and 72º C for 30 seconds with a 10-minute final step for elongation. The PCR reactions were analyzed on agarose gels stained with ethidium bromide for visualization.

The conditional knockout (cKO) Ostm1 PCR assay aimed to differentiate the size of introns flanking exon 5, cKO Ostm1 floxed allele had a size of 200 bp, the wild-type allele had a size of 100 bp, and the delta allele generated from ablation of exon 5 had 100 bp. Ostm1 assay helped in distinguishing wild-type and mutated gl allele by generating 236 bp and 330 bp respectively. Finally, the SYN1-Cre amplicon was 500 bp long. (Table 1).

2.1.6 Crosses

Ostm1$^{lox/lox}$ mice were crossed with SYN1-Cre^{+} mice to generate F1 heterozygous *Ostm1*^{lox}/$^{+}$ SYN1-Cre. F1 female *Ostm1*$^{lox/+}$ was crossed with a male heterozygous *Ostm1*$^{lox/+}$ to generate homozygous *Ostm*$^{lox/lox}$ Syn-Cre^{+}. Only female heterozygous *Ostm1*$^{lox/+}$ SYN1-Cre^{+} were used since recombination in the male germline can occur (Figure 2-1) [79].

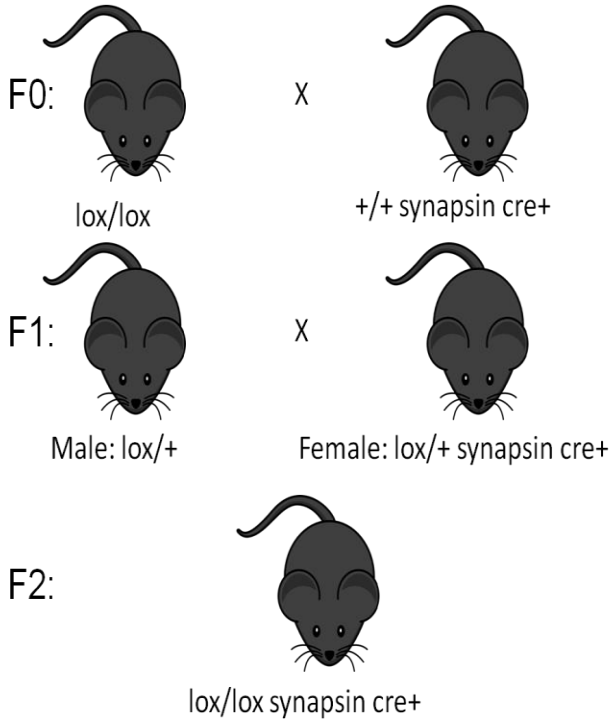

Figure2-1 Breeding Scheme of *Ostm1*$^{lox/lox}$ SYN1-Cre Mice.

2.2 Molecular Analysis

2.2.1 DNA Expression and Recombination Percentage.

DNA was extracted and visualized using the protocol of genotyping, and then the band density of the lox and delta were quantified to calculate the recombination efficiency. The bands were quantified by ImageJ. The delta band intensity was divided by the total of delta and lox and multiplied by 100 to obtain the recombination percentage.

2.2.2 RNA Expression

2.2.2.1 RNA Isolation

Mice tissues were homogenized with Trizol and incubated 5 minutes for complete dissociation of nucleoprotein complexes. Chloroform was mixed with the homogenized sample to obtain two layers: the aqueous phase and the organic phase. Isopropanol precipitated the RNA in the aqueous phase. The RNA pellet was washed with 75% Ethanol and dissolved in DEPC treated water. The quality and the quantity of the RNA were evaluated by gel electrophoresis and spectrophotometer respectively.

2.2.2.2 Reverse Transcription PCR (RT-PCR) Analysis

1 μg of the extracted RNA was treated with DNAse for 15 minutes at room temperature. The samples were incubated at 75^{o} C with 2.5mM EDTA to denature the DNAse enzyme. Adding the 10 mM poly dT primers and 2.5 mM dNTP to the sample, it was incubated for 10 minutes at 70^{o} C to anneal primers. cDNA was transcribed from RNA upon addition of the M-MuLV Reverse Transcriptase in RT M-MuLV buffer (50 mM Tris-HCl, 75 mM KCl, 3 mM MgCl2, 10 mM DTT pH8.3) for 1 hour in 42^{o} C. The enzyme was inactivated afterwards at 70^{o} C for 15 minutes of incubation.

Between 1/10 - 1/5 of the diluted cDNA with specific primers (Table 2) was carried through the PCR for 30-35 cycles. The PCR cycle conditions were 94^{o} C for 30 seconds, 63^{o} C for 30 seconds, 72^{o} C for 30 seconds followed with 72^{o} C for 10 minutes of elongation.

2.2.2.3 Real-time PCR (qPCR) Analysis

The qPCR was done by MX3005 Startagene using SYBR Green Mastermix (Qiagen, Mississauga, Ontario, CA). The reaction mixture was composed of 1 μl of cDNA, dNTP, primer (Table 3), and polymerase to reach 20 μl volume. The cycle that the mixture went through was 95 ^{o}C for 15 minutes to denature the DNA and activate the Hot start Taq DNA polymerase. This was followed by 40 repeated cycles, each consisting of 95^{o} C for 30 seconds, 60^{o} C for 30 seconds and 72^{o} C for 30 seconds. The resulted amplicons were normalized to an internal control, ribosomal protein S16 and quantified.

2.3 Biochemical Analysis

2.3.1 Antibodies

These antibodies, which were used for the biochemical analysis, are primary antibodies including: rabbit anti-LC3 (Sigma), rabbit anti-p62 (Abcam), rabbit anti-Beclin (SantaCruz), rabbit anti-Ubiquitin (Dako), mouse anti-β-actin (Sigma), and the secondary antibodies which are: Horseradish Peroxidase (HRP) labeled goat anti-mouse and goat anti-rabbit IgG (BioRad).

2.3.2 Protein Extraction and Quantification

Tissues were homogenized by manual Potter-homogenizer in 1 ml of 1x RIPA buffer (150 mM NaCl, 1% NP-40, 0.5% sodium deoxycholate, 0.1% SDS, and 50 mM Tris, pH 8.0) with protease inhibitors (1 mM PMSF, 1 mM β-glycerophosphate, 2 mM Sodium Orthovanadate, 1/1000 of Protease Inhibitor Cocktail (Sigma)) for 100 mg of tissue. Following 30 minutes of incubation on ice, the samples were centrifuged at 12,000 RPM for 30 minutes to remove the un-dissolved particles. After centrifugation, Bradford Assay was used to quantify the protein extracts.

2.3.3 Western Blots

Different resolving gels were prepared depending on the size of the protein to be detected, followed by an addition of 5% staking gel on the top of the resolving gel. After gel preparation, 15 μg of the proteins extract was resuspended in the sample buffer (62.5mM Tris-HCl pH 6.8, 2% SDS, 10% glycerol, 0.002% bromophenol blue and 5% β-mercaptoethanol) and boiled for 5 minutes before loading on the gel. The gels were inserted in the running buffer (25 mM Tris, 190 mM Glycine, and 0.1% SDS) and the loaded proteins were run in the gels at 100 V for 30 minutes with gradual increase to 150 V until the ladders were separated.

Next, the proteins were electro-transferred to Polyvinylidene Fluoride (PVDF) membranes by 300mA current for 2 hours. The transfer occurred in a transfer buffer (25mM Tris and 190mM Glycine) that was kept cold to prevent protein denaturation.

Then, the membranes were washed with 1xTBST (20 mM Tris, 137 mM NaCl, and 0.1% Tween; pH 7.6) for 15 minutes and blocked with 5% skim milk in 1xTBST. A second round of 1xTBST washing was done, before incubating with diluted primary antibody (1/1000 for all antibodies except β-actin for 1/5000) for an overnight at 4^{o} C. The membranes were washed to remove unspecific binding and incubated in secondary antibody dilution (1/10,000) in 5% skim milk in

1xTBST. Following the last washes, the membrane bands were detected by adding ECL Western Blotting Detection Kit (Amersham GE Healthcare). For other protein detection, the membranes were incubated with stripping solution (2% SDS, 62.5 mM Tris-HCl (pH 6.7), 0.6% β-mercaptoethanol) for 30 minutes to detach the bounded antibodies preventing confusion between the old and the new band. Bands were processed using Image J for quantification.

2.4 Histological Analysis

2.4.1 Tissue Embedding and Sectioning

2.4.1.1 Paraffin Embedding and Sectioning

The mice were anesthetized with 2.5% avertin in 1xPBS (137 mM NaCl, 2.7 mM KCl, 4.3 mM Na_2HPO_4, and 1.47 mM KH_2PO_4) of pH 7.5 for 0.018 µl per gram of mouse mass. They were then perfused with 1xPBS and fixed with 4% PFA. The brain and the spinal cord were isolated and incubated also in PFA for 2 hours. After fixation, the medium was changed into 1xPBS and the tissue was embedded in paraffin and cut (5 µm).

2.4.1.2 Optimal Cutting Temperature (OCT) Embedding and Sectioning

The mice were euthanized and the organs, hind limb muscle (*Tibialis anterior* (TA) and *Gastrocnemius* (Gastro) and spinal cord, were isolated and mounted in OCT compound (Tissue Tek). 10 µm sections were generated using a cryostat and were dried at room temperature for 1 hour before being stored in the -80 ^{o}C.

2.4.2 Cytoarchitectural Studies

In order to visualize the general features of an organ, the frozen sections underwent Hematoxylin and Eosin staining. First, the frozen tissues were fixed in 4% PFA for 45 minutes. Following a hydration step in 1xPBS for 3 minutes at room temperature (RT), the sections were dipped in 95% ethanol for 1 minute at RT, and all the consecutive steps were done at RT. Staining the samples in Hematoxylin (sigma) for 15 minutes lets the Hematoxylin bind with nucleic acids releasing the deep blue-purple color. The unspecific staining was rinsed with water for 15 minutes and the samples were dehydrated two times by dipping for 2 minutes each in increasing ethanol concentrations (95% and 100%). The paraffin-embedded samples required an extra step before starting the staining: deparaffinization and rehydration which will be clarified in the immunohistochemistry treatment section. Any further analysis such as quantification of muscle

surface area was done using Zeiss Axiovert microscope to capture the images and then processed on ImageJ software for quantification.

2.4.3 Immunohistochemistry

2.4.3.1 Antibodies

Incubations in primary antibodies were followed by incubations in secondary antibodies instead of incubation in labeled primary antibodies alone. The primary antibodies that were used in this biochemical analysis are: mouse anti-NeuN (Chemicon), mouse anti-GFAP (Sigma), mouse anti-MBP (Abcam), rabbit anti-LC3 (Sigma), rabbit anti-p62 (Abcam), rabbit anti-Beclin (Santa Cruz), and rabbit anti-Ubiquitin (Dako). The secondary antibodies are: Horseradish Peroxidase (HRP) labeled goat anti-mouse and goat anti-rabbit IgG (BioRad).

2.4.3.2 Immunohistochemistry Treatment

Sections were incubated twice in xylene for paraffin removal for 5 minutes. Following a rehydration step, the sample sections were dipped in decreasing ethanol concentration (100% to 70%) for 5 minutes in each concentration. To improve antibody binding, the slides underwent an antigen retrieval process by incubation in 10 mM sodium citrate of pH 6 for 20 minutes at 95^{o} C. The samples where then blocked with hydrogen peroxide to quench the endogenous peroxydase for 7 minutes and incubated in permeabilization buffer (0.05% saponin in 1xPBS) to allow access for the diluted primary antibody. Afterwards, the samples were incubated in blocking solution (3% BSA, 0.05% Saponin in 1xPBS) and then in primary antibody dilution (1/100 for antibodies except GFAP for 1/400 dilution in the blocking solution) for 2 hours to prevent unspecific binding, and to detect the antigen respectively. Rinsing the samples with 1xPBS for 3 times each to remove false positive signal, the samples were incubated with secondary antibody (1/100) for 90 minutes. The signal was revealed using DAB peroxidase substrate kit and the samples were counterstained with hematoxylin followed by mounting.

2.4.4 Immunofluorescence

2.4.4.1 Antibodies

The following antibodies were used in this study. The primary antibodies were goat anti-ChAT (Abcam), rabbit anti-ubiquitin (Dako), and mouse anti-NeuN (Chemicon). The secondary

antibodies were goat anti-mouse Alexa-488, goat anti-rabbit Alexa-546, and donkey anti-goat Alexa-647 (Molecular Probes).

2.4.4.2 Immunofluorescence Treatment

The sections were treated in the same process of immunohistochemistry treatment until the permeabilization step. After permeabilization, the samples were blocked in 0.3% Triton, 3% BSA in 1xPBS and incubated in primary antibody (1/100 dilution) overnight. Incubating the samples in secondary antibody in 1xPBS for 1 hour was followed by washing 3 times with 1xPBS and staining the nuclei with Hoescht or 4',6-diamidino-2-phenylindole (DAPI). Finally, the sections were washed and mounted.

2.4.4.3 Immunofluorescence for the Neuromuscular Junction

The transverse abdominal (TVA) muscles were dissected from the euthanized mice and fixed in 2% PFA in 1xPBS for 10 minutes. The media was substituted with 1xPBS and the samples were dissected to remove the epithelial and connective tissue above the muscle layer. Following permeabilization with 0.3% Triton in 1xPBS for 30 minutes, the samples were blocked with 4% BSA and 1% Triton for 30 minutes followed by an overnight incubation in mouse-Neurofilament-M and mouse-SV2 (Developmental Studies Hybridoma Bank, Iowa City, IA) antibodies. Before incubating the samples with the secondary antibody goat anti-mouse Alexa-488 in 1xPBS solution containing 0.3% Triton and 1% BSA for 60 minutes, the samples were rinsed to remove unbound antibodies with PBS for 15 minutes. Tetra-methylrhodamine (TRITC) conjugated with alpha-bungarotoxin (Life Technologies, Carlsad, California) was used to stain motor endplates (MEP). Finally, the sample was mounted using an aqueous media.

2.5 Ultrastructural Analysis

For preparing samples for electron microscopy, the same procedures as those for the paraffin embedding and sectioning protocol (Section 2.4.1.1) were done to isolate the organ, but the only difference was the addition 2% glutaraldehyde in the PBS to preserve the samples. Spinal cord samples were post-fixed 2 hr in the same solution, washed in phosphate buffer 0.1M and kept in phosphate buffer 0.2 M at 4° C until processing. The samples were post-fixed with 1% OsO4 in cacodylate buffer for one hour at 4^{o} C then dehydrated in graded series of ethanol and embedded in Epon [91]. After embedding, ultrathin sections of the lumbar region of the spinal cord were

obtained using a Reichert Ultracut microtome and mounted on naked nickel grids. Sections were stained with 2% aqueous uranyl acetate and lead citrate. Examination was performed with a Philips CM100 transmission electron microscope. Electron micrographs were captured using an AMT XR80 digital camera.

2.6 Myofiber Staining

The 10 μm muscle sections that were embedded in OCT and cut using cryostat were incubated in 0.2% Nitro-Blue Tetrazoluim (NBT) in 0.05 M, pH 7.6, 0.05 M TRIS Buffer and an equivalent amount of 200% NADH in TRIS Buffer solution. Then, the samples were rinsed with deionized water followed by acetone immersion in increasing concentrations (30, 60, and 90%) and then decreasing concentrations (the same in reverse order) to remove unbound NBT. After washing three times the samples with deionized water, they were mounted with an aqueous medium. The images of the muscle fibers were quantified by ImageJ and classified into myofiber types (I, IIA, IIB) based on the blue staining intensity.

2.7 Statistics

The experiments were done on 3 samples of the mutant and the control mice. The result of each sample was analyzed using ImageJ to count the number of neuron, astrocyte, and motor neuron cells, to measure the intensity, and to quantify the surface area, followed by calculation of the mean of the 3 samples and standard error mean then the results were illustrated with different graphs using GraphPad Prism. In GraphPad Prism, the results were statistically analyzed using unpaired two sample Student's t test with a significant p value ≤ 0.05.

Table 1: PCR Analysis Primers

Name:	Sequence:
KO Ostm1 gl For 3:	5'-AATAGCCAGGGTTGCACAGAGAGT-3'
KO Ostm1 gl Ex 5 Rev:	5'-GCTGGTTTACAATTAGTAAGTG-3'
KO Ostm1 gl Rev 3:	5'-TTTCACAGGGATAGTATTTTGATGC-3'
Ostm1 gl For 1:	5'-CCTCTGGAAGACTAATACTTGCTG-3'
Ostm1 gl For 2:	5'-GCTACATCTGGGTCCTTTCG-3'
Ostm1 gl Rev 1:	5'-GCCTGGAACAGAGCAAAGC-3'
Ostm1 gl Rev 2:	5'-CGCTTGCTTTTGTCTGTTACCTTTGTGTTC-3'
Cre For:	5'-AATGCTTCTGTCCGTTTGC-3'
Cre Rev:	5'-CGGCAACACCATTTTTTCTG-3'

Table 2: RT-PCR Primers

Name:	Sequence:
RT Ostm1 Ex 3 For:	5’-CCTGCTTTGAGCATAACCTGC-3’
RT Ostm1 Ex 5 Rev:	5’-CTGCAGTCCCAACTTTCGTGAG-3’
iCre For:	5’-CCTGGTCTGGACACAGTG-3’
iCre Rev:	5’-TTGCCCCTGTTTCACTATC-3’
qSyn endo For:	5’-TGGGTAGACACGTGCTCAGA-3’
qSyn endo Rev:	5’-GATGACTCAGGCTCTGCCTC-3’
qNFH endo For:	5’-GAGGACCGTCATCAGGCAGACATTGC-3’
qNFH endo Rev:	5’-TAAGCGGCAATCTCAATGTCCAGG-3’
qNeuN For:	5’-TTGAGGTCAATAATGCCACAGCCC-3’
qNeuN Rev:	5’-GAGGTGGTGCAGCTCGAAATGTAT-3’
β-Actin For:	5’-TGACGATATCGCTGCGCTG-3’
β-Actin Rev:	5’-ACATGGCTGGGGTGTTGAAG-3’

Table 3: qPCR Primers

Name:	Sequence:
qOstm1 For 1:	5’-GTGGTTGCTGTGTCTGTGTTC-3’
qOstm1 Rev 1:	5’-CAGGAGACTTCCGCCACAG-3’
qNeuN For:	5’-TTGAGGTCAATAATGCCACAGCCC-3’
qNeuN Rev:	5’-GAGGTGGTGCAGCTCGAAATGTAT-3’
qS16 For:	5’-GCTACCAGGGCCTTTGAGATG-3’
qS16 Rev:	5’-AGGAGCGATTTGCTGGTGTGC-3’

Chapter 3

Results

3.1 Ostm1 Neuronal Conditional Knockout Mouse

To characterize the prognosis of the disease in the nervous system in-vivo, recombinant mice were generated. These mice are genetically modified, specifically, a gene is inactivated in a certain organ or their entire body. This modified knockout resembled the spontaneous mutation and displayed the defective phenotype that enabled its analysis. From that point on, one can extrapolate the role of the gene. The strategy for the knockout mouse was not only to continue investigating the role of Ostm1 after the double transgenic rescue of the PU.1-*Ostm1*-SYN1-*Ostm1*-gl/gl mice [56] but also to mimic the Italian patient who had a mutation leading to the skipping of exon 5 [76]. The strategy comprised the creation of loxP sites flanking the transmembrane *Ostm1* domain and then a recombinase excising the flanking sites. First, the artificial DNA (vector) consisting of loxP sites surrounding exon5, neomycin, upstream 5' homology arm, and 3' homology arm was introduced to embryonic stem cells (ESC) for genetic targeting. An additional step could be included to enrich the selection and prevent the random insertion of the artificial DNA (vector) by adding another marker that is antagonist to neomycin gene like herpes simplex virus thymidine kinase (HSV TR). This negative selection marker HSV TR would be added outside of the homology arms region of the vector, hence, if a homologous recombination occurs, the entire DNA between the homologous arms would be integrated and the genes outside that area would be lost. In the case where all of the sequence was integrated randomly with the HSV TR, the cell will then die due to the incorporation of the activated ganciclovir in the selecting medium by HSV TK [92]. The two arms are the basis of the homologous recombination with the endogenous exon 5. After transfection, cells that grow on toxic agent neomycin medium were selected due to having successful recombination including neomycin in their genome. The engineered embryonic stem cells (ESC) are injected into a mouse blastocyste to give a chimeric newborn. Following the crossing of these chimeric mice to produce heterozygote with one copy of the recombinant allele, these heterozygotes were interbred to produce homozygous recombinant alleles. The neomycin flanking frt site was excised by flipase (FLPeR) to prevent the interference with gene expression [93]. The expression of flipase was done by mating the homozygous mice with transgenic FLPeR mice [94]. The resulted mice were mated with Synapsin-Cre (SYN1-Cre) to target only the neurons and generate homozygous $Ostm1^{\Delta exon5}$ mice (Figure 3.1).

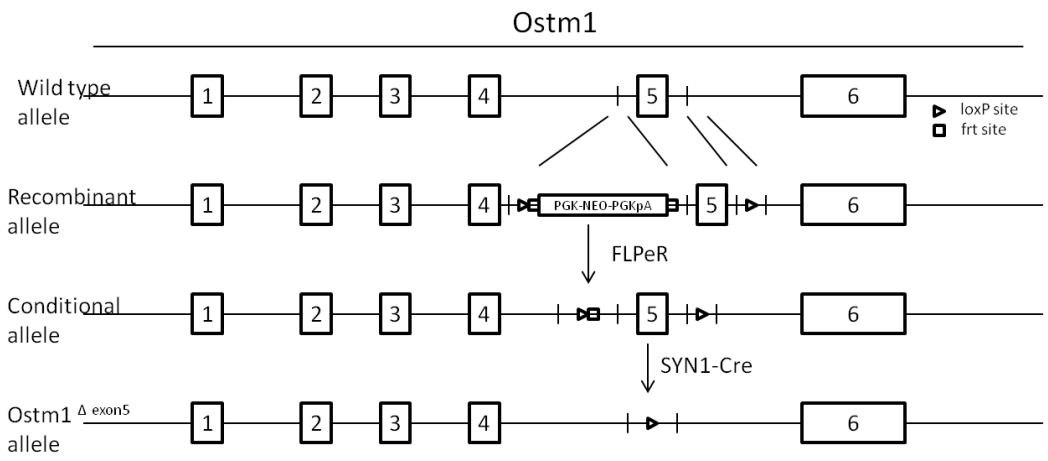

Figure 3-1 *Ostm1* $^{\Delta exon5}$ Allele Generation. LoxP sites and frt sites flanking exon5 and neomycin were recombined with endogenous exon 5 creating a recombinant allele. *Ostm1* $^{\Delta exon5}$ allele was produced by two consecutive excisions. (First, FLPeR removes neomycin, and then SYN1-Cre to delete exon 5.)

In addition to the spatial Cre expression, Cre can be controlled timely either in embryonic or postnatal stage by using a specific promoter. Cre-loxP system is a successful approach to avoiding activation of immune response and the harmful consequences of the transgene during embryogenesis. SYN1 rat promoter was used to target the brain and the spinal cord [95]. Synapsins are a family of neuronal phospho-proteins. They regulate the release of the neurotransmitters at the presynaptic terminal by binding to the vesicles. Beside their role in neuronal networking, they play a crucial role in tuning neuronal plasticity [96]. Synapsin 1 is expressed in all differentiated neurons and can be used as a promoter to direct the excision of Cre recombinase. Since neuronal conditional Ostm1 loss will mirror the *gl/gl* and osteopetrotic patients, it should be deleted as early as possible. This condition was satisfied by Synapsin 1 promotor due to its early and continuous expression starting at E.12 in the rat's brain and spinal cord [95, 97].

3.2 Recombination Percentage Efficiency and Specificity

To detect whether Cre complied with the specificity and efficiency recombination, the *Ostm1* $^{\Delta exon5}$ allele was measured at different nucleic acid level, DNA and RNA.

3.2.1 DNA Recombination Level

To check whether this recombination was specific, DNA extracts were collected from different organs, brain (Br), spinal cord (Sc), and liver (Lvr) and were amplified by PCR that was followed by analysis in gel mobility. Concomitant with the neuronal Cre promoter, the genomic

amplicon corresponding to the null allele lacking exon 5 is only detected in brain and spinal cord attesting Cre appropriate expression and proper recombination (Figure 3-2).

Besides the specific *Ostm1* neuronal knockout, calculating the efficiency of Cre is an essential factor if the loss of function occurred. To know the percentage of recombination required to mimic the spontaneous mutation, one should know the inheritance patterns of the gene. *Gl* mutation belongs to the autosomal recessive osteopetrosis, thus both alleles are required to be defected to have phenotype. In this case, the percentage of recombination should be more than 50%. The PCR products indicated that 23% of cells were recombined in the brain, and 20% in the spinal cord at 4 weeks. Considering that neurons represent 35% of the mouse brain and 30% in the spinal cord [98-100], the percentage of recombination in neurons reach approximately 64% in the brain and 64% in the spinal cord (Figure 3-2 A).

Further analysis that could be extrapolated from DNA recombination is monitoring this percentage with age. The percentage recombination was monitored in the *Ostm1*$^{lox/lox}$ SYN1-Cre^{+} and in the *Ostm1*$^{lox/lox}$ SYN1-Cre^{-} at 4w and 12w. Surprisingly, the percentage decreased from 64% to 48% in both brain and spinal cord considering the percentage of neurons is approximately similar at 4 and 12 weeks [101]. This raises a question as to whether there may be a neuronal death with age (Figure 3-2 B).

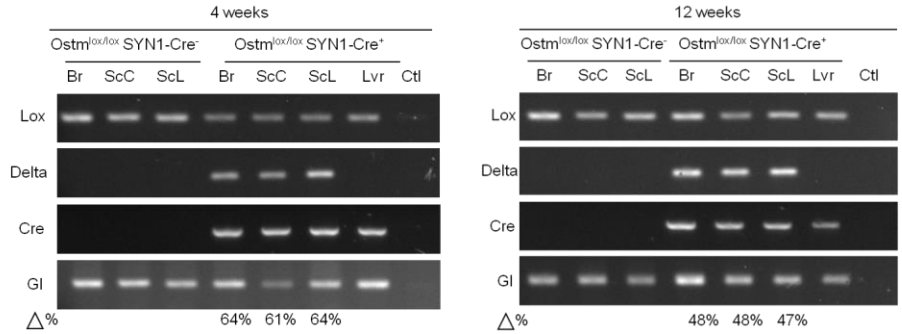

Figure 3-2 Semi-Quantitative PCR Results of Different Tissues of the *Ostm1*$^{lox/lox}$-SYN1-Cre^{+} and *Ostm1*$^{lox/lox}$-SYN1-Cre^{-} at 4w and 12w with Exon 1 *Ostm1* as Internal Control Showing Specificity. With age, the recombination percentage in the brain and in the spinal cord decreased approximately from 64% to 48%. Br=brain; ScC= cervical spinal cord; ScL= lumbar spinal cord; Ctl = negative control (no DNA)

3.2.2 RNA Expression

Heading to the transcriptional level, the expression analysis was done to confirm the results of the DNA recombination. RNA was isolated and underwent reverse transcription followed by PCR amplification for *Ostm1* exons 5 and 6 with β-actin as control. Before the start of the qPCR, the quality of the RT-PCR products was assessed by running them on an agarose gel. In the brain

and spinal cord, only the amplicon for specific neuronal deleted exon5 *Ostm1* appeared. The RT-PCR gels (Figure 3-3 A) showed similar pattern as the PCR-gel (Figure 3-2). To ensure that neuronal cells were found in the sample, different neuronal markers such as neuronal nuclei (NeuN), neurofilament heavy chains (NFH), and Synapsin 1 (SYN1) were tested. NeuN is a neuronal nuclear protein that functions as Rbfox3, a family of splicing factors [102]. NFH is a neuronal intermediate filament that forms and supports the cell architecture and interacts with other proteins aiding in transporting organelles and optimizing the conduction velocity [103, 104]. Both *Ostm1*$^{lox/lox}$ SYN1-Cre^{+} and *Ostm1*$^{lox/lox}$ SYN1-Cre^{-} express NeuN, NFH, and SYN1 in the brain, spinal cervical and lumbar at 4 and 12 weeks but these gels showed semi-quantitative results that were not precisely measurable.

Quantification of these genes with respect to S16 was processed by qPCR in which the *Ostm1* expression from the *Ostm1*$^{lox/lox}$-SYN1-Cre^{+} showed the expected RNA value relative to the *Ostm1*$^{lox/lox}$ SYN1-Cre^{-}. In the brain, the *Ostm1* RNA prevalence of *Ostm1*$^{lox/lox}$ SYN1-Cre^{+} was reduced by 67% at 4 weeks and by 50% at 12 weeks relative to *Ostm1*$^{lox/lox}$-SYN1-Cre^{-}.

In the cervical spinal cord (ScC), the *Ostm1* amplicon was also decreased compared to the control by 76% at 4 weeks and by 60% at 12 weeks. In the lumbar spinal cord (ScL), the *Ostm1* was lessened relative to the control by 73% at 4 weeks and 62% at 12 weeks. In contrast to non-neuronal organs such as the liver shown in the bar graph, the RNA decrease was not significant in the *Ostm1*$^{lox/lox}$ SYN1-Cre^{+} compared to the controls at 4 weeks and at 12 weeks, the *Ostm1* expression was approximately the same in both (Figure 3-3 B). All the evidence above indicated tissue specificity and efficacy of SYN1- Cre recombinase.

As the mouse aged, the reduction in *Ostm1* expression level of the *Ostm1*$^{lox/lox}$-SYN1-Cre^{+} mouse lessened compared to the control. For instance, the RNA percentage loss in the brain decreased from 67% to 50% at 4 weeks and 12 weeks, respectively, indicating a decrease in null allele number. *Ostm1* expression was tested in both neuronal and non-neuronal cells which express *Ostm1*. Results indirectly showed neuronal degeneration due to an increase of *Ostm1* peaks with time.

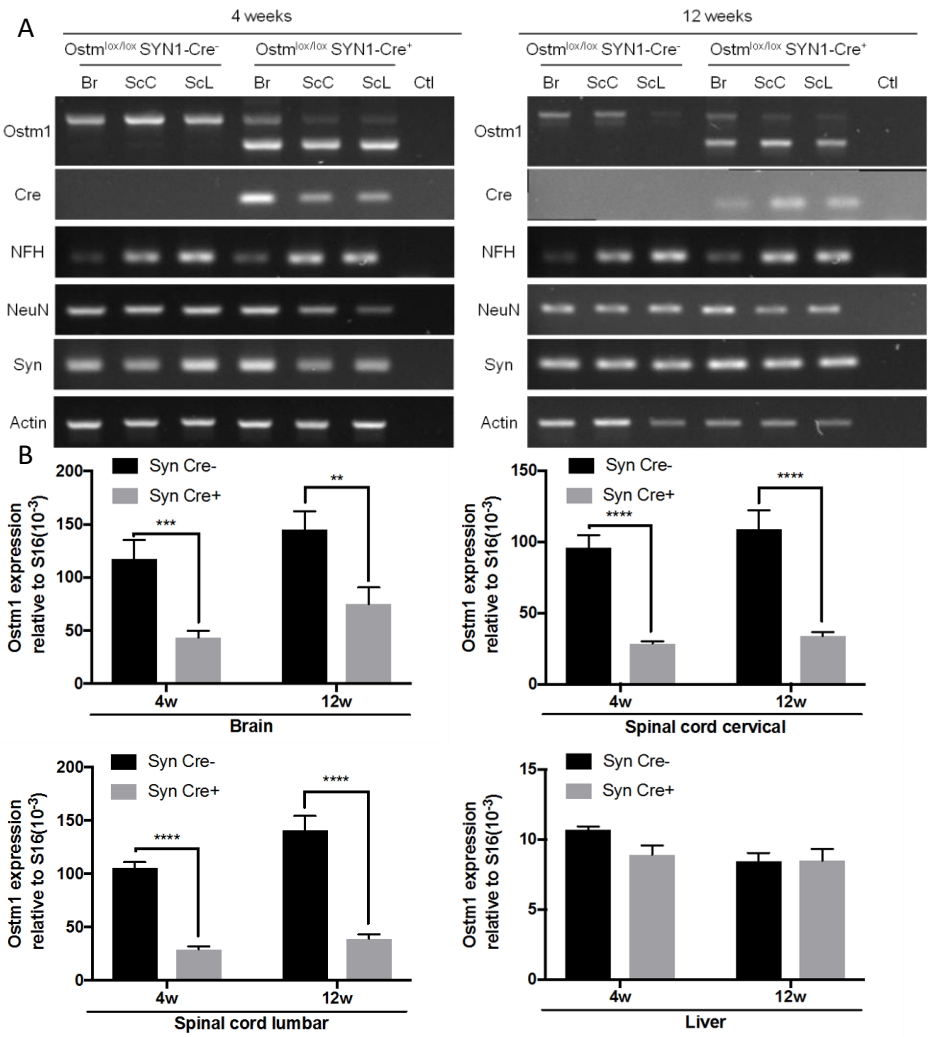

Figure 3-3 *Ostm1* and Neuronal Markers Expression Showing Specificity and Efficiency of the Recombination. (A) Semi-quantitative gels showing the null allele in neuronal organs with age. The markers were normalized to β-actin. Br=brain; ScC= spinal cord cervical; ScL= spinal cord lumbar; Ctl = negative control; NeuN=neuronal nuclei; NFH=neurofilament heavy chains; Syn=Synapsin 1. (B) Quantification of Ostm1 expression by qPCR at 4w and 12w in the brain, spinal cord (cervical and lumbar) and liver respectively (n=3). The Ostm1 expression was reduced in the brain and spinal cord, but this reduction decreased with age hinting on neuronal decrease. The Ostm1 was normalized to S16. **, $p < 0.01$, ***, $p < 0.001$, ****, $p < 0.0001$. *Error bars*, S.E. 4w= 4 weeks, 12w= 12 weeks.

To directly test this hypothesis, expression of the neuronal marker NeuN was analyzed across age. The results suggested a decrease in the RNA NeuN levels in *Ostm1*$^{lox/lox}$ SYN1-Cre^{+} with respect to the control from non-significant value at 4 weeks in all organs till 65% in the brain, 50% in cervical spinal cord, and 57% in lumbar spinal cord at 12 weeks (Figure 3-4). This decrease in expression could be due to either downregulation of the NeuN marker or decrease in number of cells, it also could be a combination of both. These evidences suggested that further tests should be ensued.

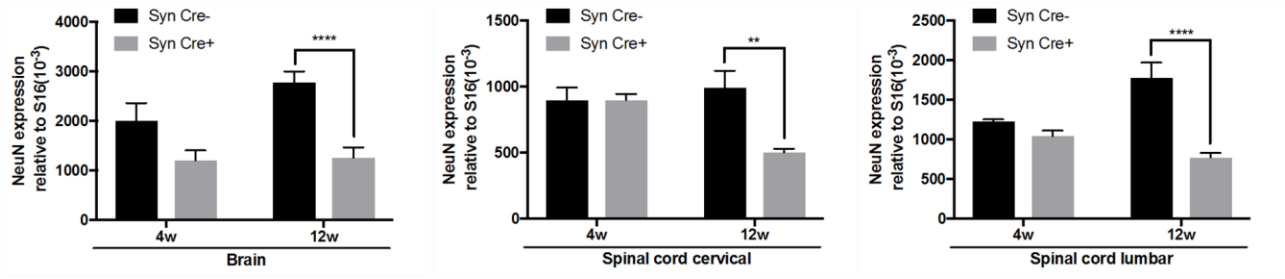

Figure 3-4 Quantification of NeuN Expression in Mutant and Control Mice with Age. At 4 weeks the expression was non-significantly different in the mutant and the control. At 12 weeks the level of NeuN lessens by 65% in the brain, 50% in the cervical spinal cord, and 57% in lumbar spinal cord (n=3). The NeuN was normalized to S16. Approximately same sample size was used for the 4 and 12 weeks. NeuN=neuronal nuclei, 4w= 4 weeks, 12w= 12 weeks. **, $p < 0.01$, ****, $p < 0.0001$. *Error bars*, S.E.

3.3 Phenotypic Characterization of Ostm1$^{lox/lox}$-SYN1-Cre^{+} ice

These mice had a short life span of 12-14 weeks compared to the wild type (2 years) but doubled relative to the 6-7 week life expectancy of the PU.1-*Ostm1-gl/gl* mice. Along this life span, several phenotypes were observed, indicating a neuronal defect. Before 8 weeks, the littermates were indistinguishable from the controls. Starting at 8 weeks, the mice had some gait problems and the motor tasks (balance beam, rotarod, and inverted grid) were challenging for them. This motor defect worsened with age by the occurrence of tremors and abnormal limb clasping reflex reaching limb paralysis at 12 weeks (Figure 3-5 A).

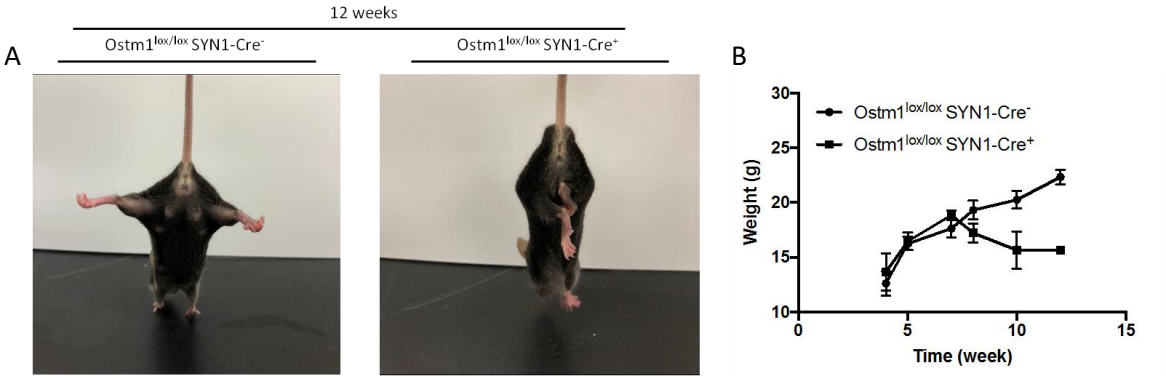

Figure 3-5 Phenotypical Observation in the *Ostm1*$^{lox/lox}$-SYN1-Cre^{+} and Cre^{-}. (A) The *Ostm1*$^{lox/lox}$-SYN1-Cre^{+} mouse suffered from hind limb clasping at 12 weeks. (B) The mutant started losing weight at 8 weeks and continued with age (n=5). *Error bars*, S.E.

Also in the final stages, the mice developed kyphosis, a pathological condition of excessive out-warding of the spinal cord. Limb paralysis caused the mice to drag their legs whenever they

wanted to move. These changes transformed the mouse into a non-ambulatory and moribund state. The *Ostm1*$^{lox/lox}$ SYN1-Cre^{+} mice did not only faced locomotion defects but also a weight decrease at 8 weeks and onwards (Figure 3-5 B).

3.3.1 Spinal Cord Size Reduction

A general histologic approach using hematoxylin and eosin (H&E) staining indicated that the spinal cord of the mutant mice and the control were similar at 4 and 8 weeks, but this observation changed at 12 weeks resulting from the decrease in the total size of the spinal cord that could explain disruption of the neural system that will be analyzed for its constituents (Figure 3-6).

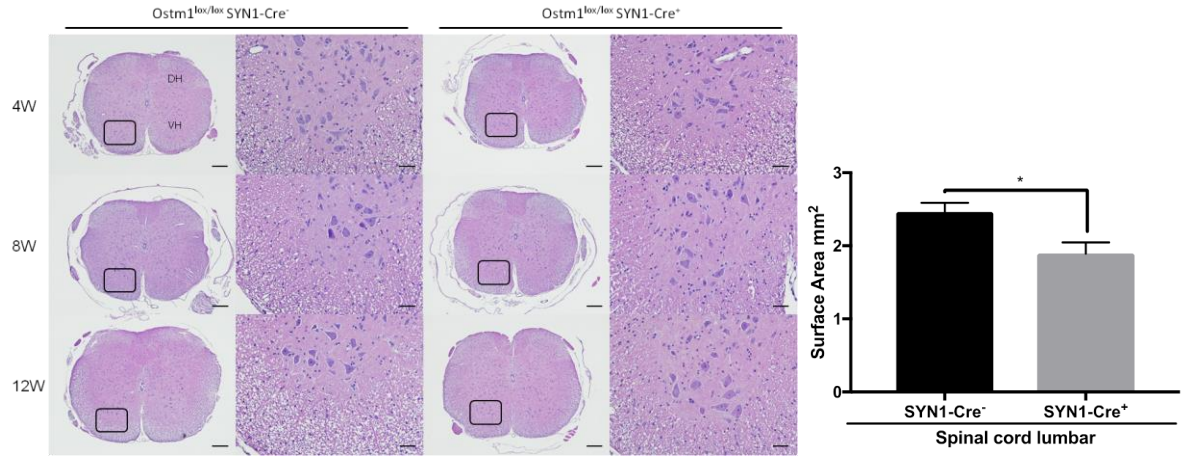

Figure 3-6 H&E Stained the Lumbar Spinal Cords of Different Ages Showing its Morphology. Reduction in surface area of the 12 week lumbar spinal cord mutant compared to the control. The total size of the ScL was approximately similar until 8 weeks. 4W= 4 weeks, 8W= 8 weeks, 12W= 12 weeks. Scale in entire ScL= 200 μm, and in the zoom anterior horn of ScL = 50 μm.

3.3.2 CNS Inflammatory Response

One of the important hallmarks of a defective nervous system is the activation of the inflammatory response. The neuronal inflammatory response consists of activating glial cells such as microglia and astrocytes. An assessment of the central nervous system was done in order to understand in-depth the hallmarks of this pathogenesis and its similarities with the PU.1-*Ostm1-gl/gl* mice. Since the behavioral deficits started at 8 weeks, we questioned whether any disturbances occurred previously. The astrocytes were detected by GFAP staining. The number of astrocyte population of the 4-week-old *Ostm1*$^{lox/lox}$ SYN1-Cre^{+} and *Ostm1*$^{lox/lox}$ SYN1-Cre^{-} looked alike in the spinal cord.

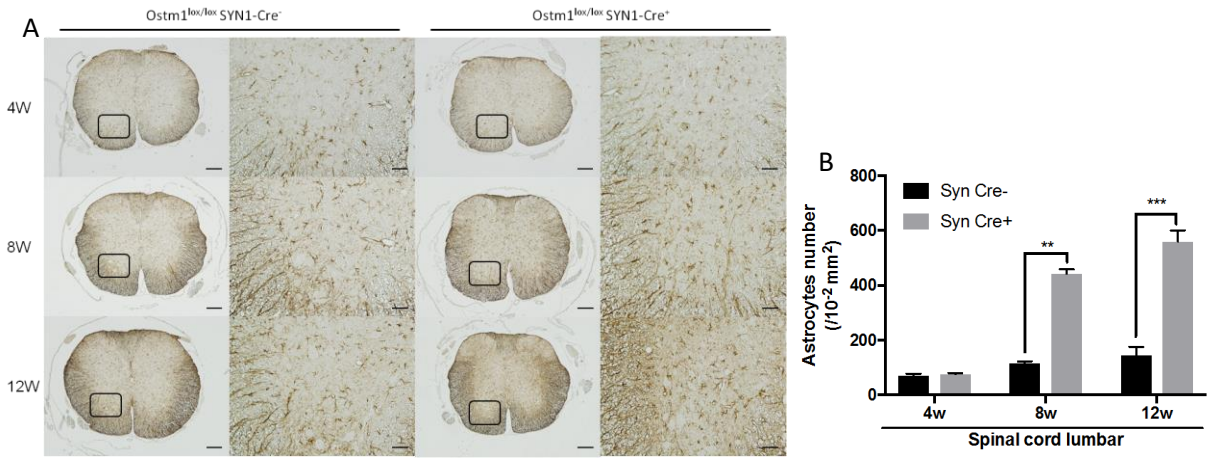

Figure 3-7 GFAP Staining Showing the Number of Astrocyte at 4, 8 and 12 Weeks in Ostm1$^{lox/lox}$-SYN1-Cre^{-} ScL Sections Relative to the Control. (A) The GFAP immunostaining became stronger (darker) with age in the mutant. Scale bar, 200 μm; 50 μm inset. (B) Quantification of astrocyte in 10^{-2} mm^2 of ScL was elevated by 2.5 fold at 8 weeks and 3 fold at 12 weeks in the mutant with respect to the control (n=3). **, $p < 0.01$, ***, $p < 0.001$. Error *bars*, S.E. 4W= 4 weeks, 8W= 8 weeks, 12W= 12 weeks.

The astrocyte inflammatory response started appearing at 8 weeks where the GFAP immunostaining signal appeared slightly higher than the control and continued to become stronger at 12 weeks (Figure 3-7 A). The immunostaining was followed by quantification of the astrocytes relative to the controls for further support that was increased by 2.5 fold at 8 weeks and 3 fold at 12 weeks (Figure 3-7 B).

3.3.3 Myelination Reduction

Due to the decrease of myelin specific lipids that was detected from the translucent morphology of the brain in the *gl/gl* mice [79] and knowing that most neuronal axons are located in white matter region of the spinal cord [105], we questioned whether the spinal cord of the *Ostm1*$^{lox/lox}$-SYN1-Cre^{+} suffered from hypo-myelination. To investigate this hypothesis, spinal cords were immunostained for myelin binding protein (MBP) at different developmental age. The appearance of the spinal cord section looked indistinguishable at 4 weeks in the *Ostm1*$^{lox/lox}$ SYN1-Cre^{-} and *Ostm1*$^{lox/lox}$ SYN1-Cre^{+}.

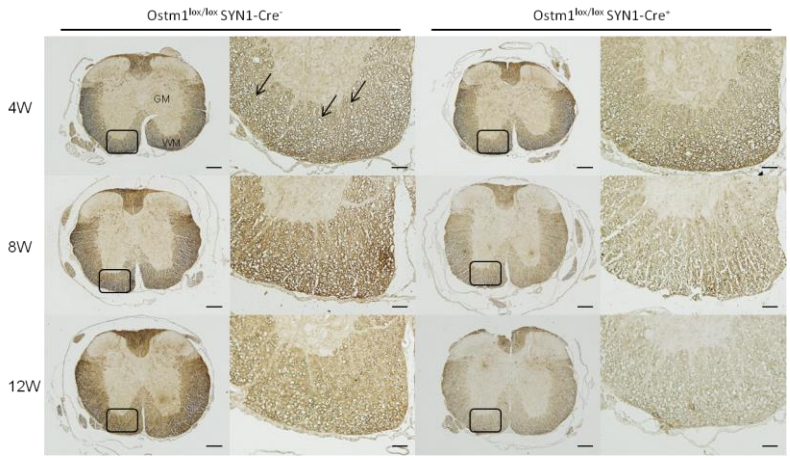

Figure 3-8 MBP Immunostaining Displaying Myelin in the Mutant and the Control ScL. The myelin color indicated by the brown intensity as it became lighter with age in the mutant indicating hypo-myelination. White holes in the white matter are neuronal axons indicated by arrow. GM= gray matter, WM= white matter, 4W= 4 weeks, 8W= 8 weeks, 12W= 12 weeks. Scale in entire ScL= 200 μm, and in the zoom anterior horn of ScL = 50 μm.

The difference in the *Ostm1*$^{lox/lox}$ SYN1-Cre^{+} compared to the control began at 8 weeks when the reduction in immunostaining intensity indicated hypo-myelination and became lighter at 12 weeks.

Furthermore, these mutant spinal cord samples did not only lack a defined demarcation between the white matter and the grey matter, but the grey matter infused the white matter (Figure 3-8).

3.3.4 Neurodegeneration in the Spinal Cord

To link behavioral defect with the central nervous system, the well-being and the viability of the neurons were evaluated. NeuN staining marked the neurons for visualization. At the start of the slightly pronounced astrocyte activation, the neuronal population number in the *Ostm1*$^{lox/lox}$ SYN1-Cre^{+} resembled the control (Figure 3-9 A). Neuronal loss was evident at 12 weeks when the NeuN stained neurons decreased by 27% (Figure 3-9 B).

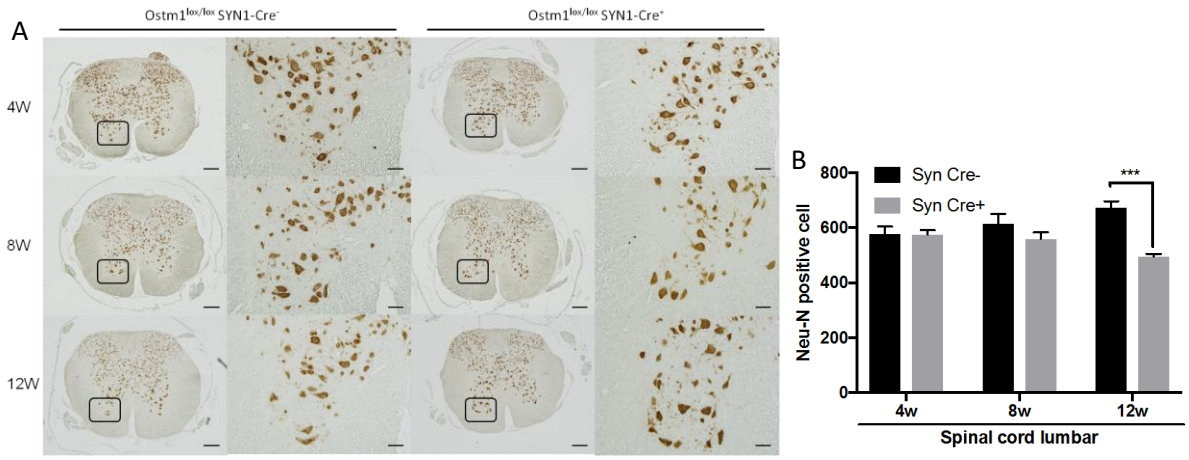

Figure 3-9 NeuN Staining of ScL Sections in *Ostm1*$^{lox/lox}$-SYN1-Cre^{-} and SYN1-Cre^{+} at 4, 8 and 12 Weeks.(A) The immunostaining looked similar until 8 weeks; afterwards the number of neurons lessened in the mutant at 12 weeks. Scale bar, 200 μm; 50 μm inset. (B) Quantification of neuron numbers in the entire ScL showed a decrease of 27% only at 12 weeks (n=3). ***, $p < 0.001$. *Error bars*, S.E. NeuN=neuronal nuclei, 4W= 4 weeks, 8W= 8 weeks, 12W= 12 weeks.

3.3.5 Motor Neuron Loss

Particularly, the motor phenotype defect is correlated with damaged motor neurons. We examined the ventral horn of the spinal cord since it harbors motor neurons that send their axons to the skeletal muscles. Motor neurons were quantified in the lumbar spinal cord ventral horn by specific staining with cytosolic Choline Acetyltransferase (ChAT), an enzyme that biosynthesis acetylcholine which is the neurotransmitter released by motor neurons to activate the muscle [106], and nuclear DAPI. The motor neurons were counted in the *Ostm1*$^{lox/lox}$ SYN1-Cre^{-} and SYN1-Cre^{+} at 12 weeks. A 57% decrease was noticed relative to the control (Figure 3-10).

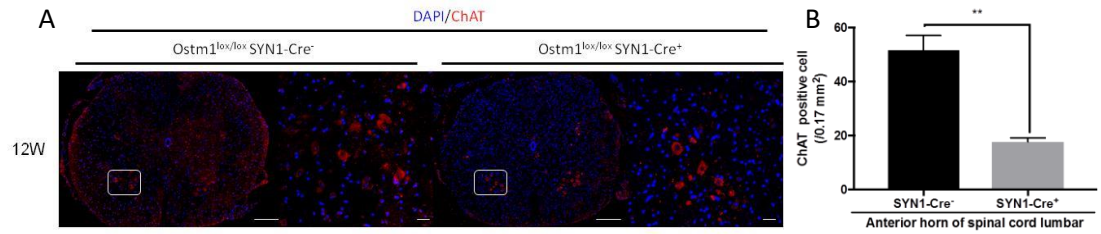

Figure 3-10 Representative Images of Motor Neurons in ScL Co-Immunostained with Cytosolic ChAT and Nuclear DAPI. (A) Reduced number of motor neurons was detected in the anterior horn of ScL mutant compared to the control. Scale bar, 200 μm; 50 μm inset. 12W= 12 weeks, ChAT= Choline Acetyltransferase. (B) Quantification of motor neuron number in 0.17 mm^2 show a decreased by 57% in mutant at 12 weeks (n=2). **, $p < 0.01$. *Error bars*, S.E.

Taken together the histology data demonstrated a widespread activation of astrocytes in the mutant spinal cord that was followed by neuronal loss especially in the motor neurons. This neuronal loss may trigger a massive increase of astrocytes by 12 weeks of age.

3.3.6 Axonal Swelling and Neuromuscular Junction

To further gain insight in the neuronal pathogenesis, ultrastructural analysis of the anterior horn of the lumbar spinal cord was conducted in the 12-week-old *Ostm1*$^{lox/lox}$ SYN1-Cre^{+} and Cre^{-}. The axons of the neurons in the *Ostm1*$^{lox/lox}$ SYN1-Cre^{+} were larger than those in the control at 12 weeks corresponding to axonal swelling. Looking inside the axon there was abundant accumulation of electron dense inclusions (Figure 3-11), referring to storage defects in cortical and hippocampal neurons of PU.1-*Ostm1-gl/gl* whose vacuolation imaged by electron microscopy at a higher magnification revealed disorganized neurofilaments and accumulation of cellular structures similar to autophagosomes [56]. These inclusions in the spinal cord may resemble autophagy components that require further testing by immunohistochemistry.

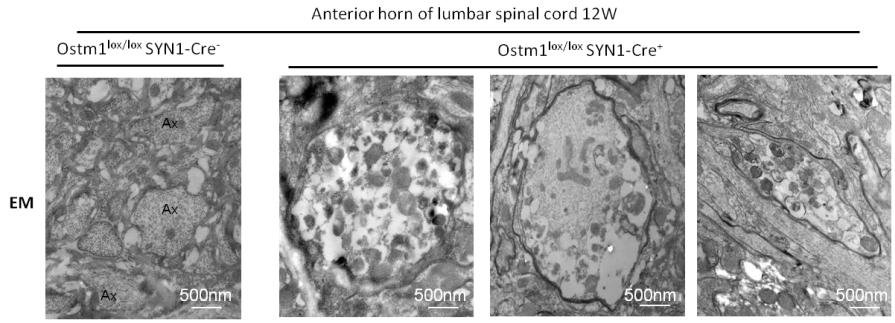

Figure 3-11 Representative Images of Ultra-Structural Analyses of Axonal Cross-Sections in the Anterior Horn of ScL in the *Ostm1*$^{lox/lox}$-SYN1-Cre^{-} and Cre^{+} by EM. The mutant axons cross sectional area was larger and contained many inclusions compared to the control. The myelin boundaries were also thinner in the mutant. Ax= axon, EM = electron microscopy, 12W= 12 weeks. Scale bar, 500 nm.

Consistently with histology staining, the myelin surrounding axons was thinner in the SYN1-Cre^{+} compared to the control.

Since locomotion requires collaboration of the motor neurons and the muscles, a bridge should be linking the two: the neuromuscular junction (NMJ). NMJ analysis provides a broad insight about different features: the morphology of the motor neurons, the frequency of innervations and the size of motor endplates. Any disturbances of the NMJ indicate neuromuscular pathogenesis such as the SMA disease in which the NMJs are the initial sites of pathogenesis [107]. To validate the axonal swelling that was seen in the ultra-structural analysis and detect other symptoms of NMJ defect, mouse Transverse abdominus (TVA) muscles were immunostained

with neurofilament (NF-M) and synaptic vesicle 2 (SV2). At 12 weeks, the *Ostm1*$^{lox/lox}$-SYN1-Cre^{+} demonstrated pre-synaptic swelling/ enlargement detected by axonal neurofilaments green staining (spheroids) with respect to the control.

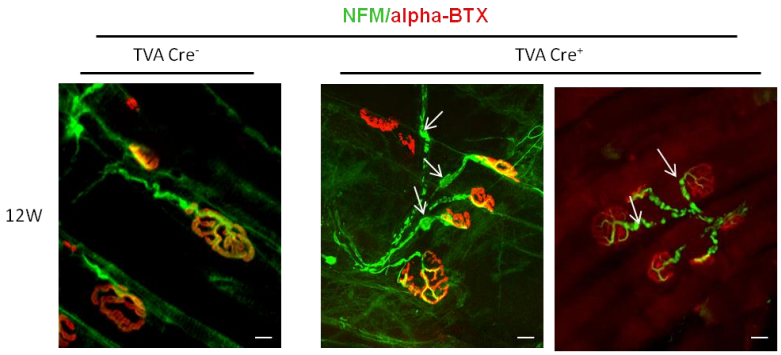

Figure 3-12 Representative Image of NMJ Examination in the TVA of the Mutant and the Control at 12 Weeks Using NFM/alpha-BTX Immunostaining. Swelling in the pre-synaptic axons of the mutant compared to the control was pointed by arrows. TVA= Tranversus abdominis, NFM= neurofilament, alpha-BTX= alpha-bungarotoxin, 12W= 12 weeks. Scale bar, 20 μm.

The motor endplates stained by alpha-bungarotoxin (red) sometimes appeared approximately similar in size in both mice (Figure 3-12) but denervation and reduced NMJ size were present in mutant samples. Overall, these results showed that the loss of Ostm1 function leads to hypo-myelination, widening and protrusion of the axons suggesting a hindered intracellular cargo transportation.

3.3.7 Muscle Fiber Cross-Sectional Area Reduction

Since contraction of the muscle is initiated by the motor neurons, an assessment of the impact of motor neuron axonal swelling on the muscle was monitored. Tibialis anterior (TA) muscle cross-sections were stained with H&E for a general observation.

A

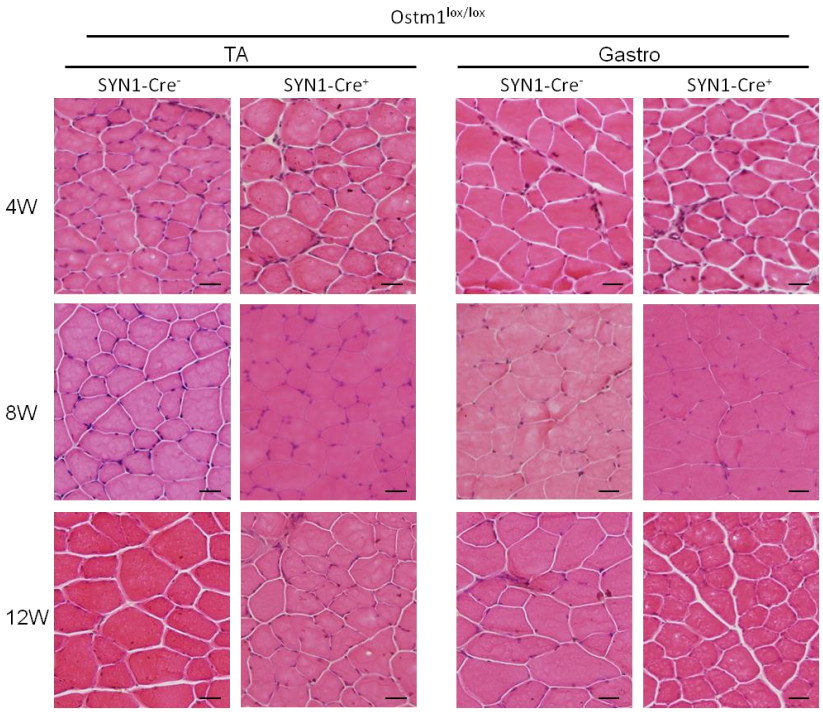

B

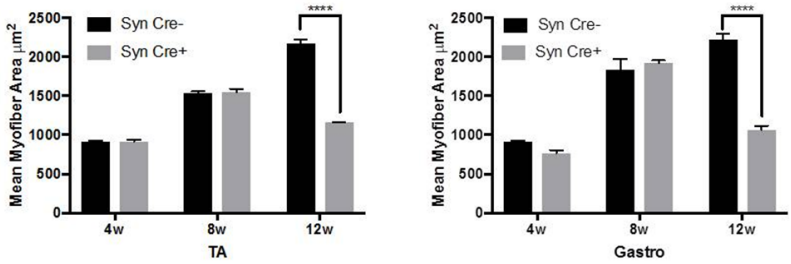

C

Muscle Type	Cre-/+	Myofiber Area	P value
TA	Syn Cre-	2172.8±28.8µm²	<0.0001
	Syn Cre+	1158±2.4µm²	
Gastro	Syn Cre-	2226.9±42.3µm²	<0.0001
	Syn Cre+	1067.8±28.8µm²	

Figure 3-13 Muscle Fibers Area Analysis in the *Ostm1*$^{lox/lox}$-SYN1-Cre^{+} and Control.(A) Representative images of H&E staining of TA and Gastro muscles sections indicated similar size until 8 weeks in both samples. By 12 weeks, the muscle fibers were smaller in size in the mutant compared to control. Scale bar, 50 µm. (B) Quantification of the average cross-sectional surface area of myofibers in TA and Gastro of mutant and control at 4, 8, and 12 weeks. ****, $p < 0.0001$. *Error bars*, S.E. (C) Average cross-sectional surface area at 12 weeks. TA= Tibialis anterior, Gastro= Gastrocnemius, 4W= 4 week, 8W= 8 week, 12W= 12 week.

The morphometry of the myofibers in the *Ostm1*$^{lox/lox}$-SYN1-Cre^{+} did not change at 4 and 8 weeks compared to the control. However, by 12 weeks, most myofibers decreased in size in the *Ostm1*$^{lox/lox}$ SYN1-Cre^{+} (Figure 3-13 A). To support this result, the average surface area of the myofiber was calculated. The analysis presented non-significant change in the values in both

mice at 4 and 8 weeks. However, at 12 weeks, the mean surface area of the *Ostm1*$^{lox/lox}$ SYN1-Cre^{+} fibers was significantly reduced to approximately half the average of the surface area of the control (Figure 3-13 B, C).

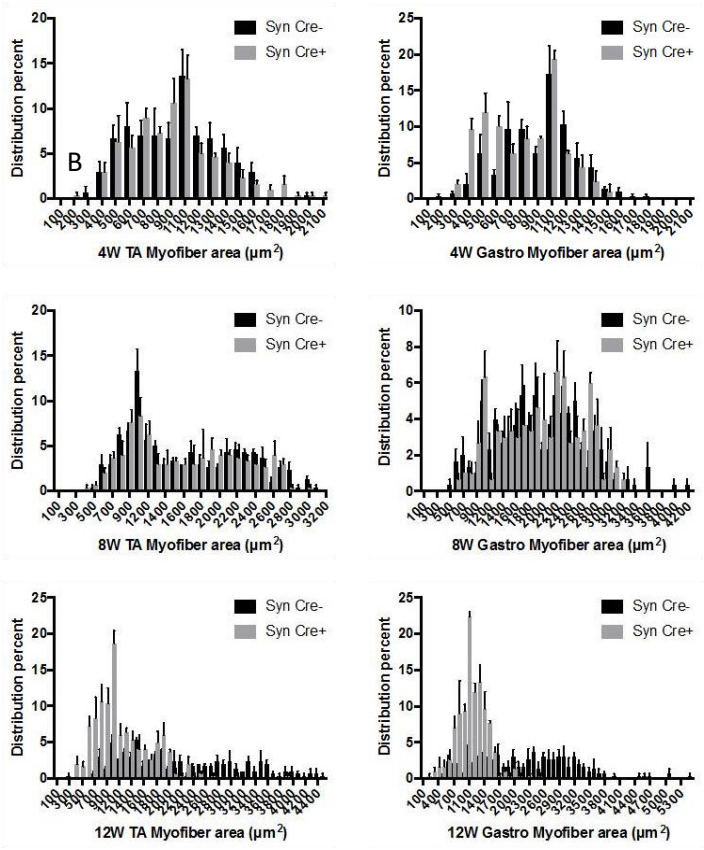

Figure 3-14 Distribution and Quantification of the Myofibers Size in TA and Gastro Muscles from Mutant Mice Compared to Control at 4, 8 and 12 weeks. The mutant myofibers showed a shift toward the small range size with age in both TA and Gastro muscles compared to control (n=3). TA= Tibialis Anterior, Gastro= Gastrocnemius, 4W= 4 weeks, 8W= 8 weeks, 12W= 12 weeks.

Then we questioned whether this reduction was only limited for the TA or represented a more general defect. The Gastrocnemius muscle (Gastro) was thus investigated and a similar 50% decrease at week 12 in the average cross-sectional myofibers surface area of the Ostm1$^{lox/lox}$ SYN1-Cre^{+} was quantified (Figure 3-13 A, B, C).

We also determined the muscle fiber size distribution with progression of the pathology. With age (4, 8 and 12 weeks), fibers size distribution in mutant TA and Gastro muscles demonstrated a significant shift toward smaller size (Fig 3-14) consistent with observed denervation (Fig 3-12). To determine if the reduction of muscle fibers size affected differentially slow contracting, small, oxidative type I fibers; fast contracting, large, glycolytic type IIB fibers; and fast contracting, intermediate, oxidative-glycolytic type IIA; specific Nicotinamide Adenine Dinucleotide

Tetrazolium Reductase (NADH-TR) staining was undertaken [108, 109]. In the TA, the mean myofibers surface area of type I, type IIA, and type IIB in the mutant decreased by non-significant 20%, non-significant 23%, and significant 32%, respectively, compared to the control as shown in Figure (3-15) indicating that neurodegeneration affected all muscle fiber types.

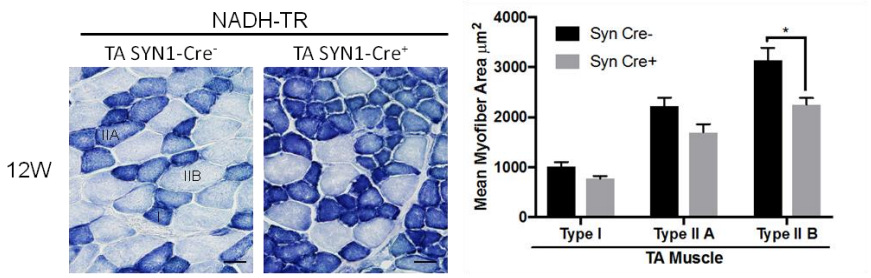

Figure 3-15 NADH-TR Staining Reveal Differentiated Muscles Fibers Types in the Mutant and the Control. Reduction in the type I, IIA, IIB cross sectional surface in the mutant compared to the control as seen in the TA section image and quantification (n=3). NADH-TR= Nicotinamide Adenine Dinucleotide Tetrazolium Reductase, TA= Tibialis Anterior, 12W= 12 weeks. Scale bar, 50 µm. * $p < 0.05$. *Error bars*, S.E.

Absence of Ostm1 led to a secondary muscle deficit phenotype. The deficit in the muscle was characterized by reduction of the myofiber surface area. The reduction affected general hind limb muscles (TA, Gastro) myofibers shifting their size distribution toward the small range. In addition, the reduction spread to all its types (I, IIA, IIB) with type IIB being greatly reduced. This massive decrease in muscle size led to muscle wasting, weakness, and paralysis.

3.4 Molecular Mechanism Responsible for Neuronal Deficit

To decipher the mechanism associated with neuronal degeneration, the intracellular autophagy pathway was analyzed including major molecular players involved in autophagy response. This was based on our previous intracellular examination of PU.1-*Ostm1-gl/gl* that showed a stimulation of autophagy pathway [56].

3.4.1 Ubiquitin Accumulation

Ubiquitin binds to proteins to recruit them into the recycling pathway. Spinal cord sections of the *Ostm1*$^{lox/lox}$-SYN1-Cre^{+} and the *Ostm1*$^{lox/lox}$-SYN1-Cre^{-} were co-immunostained for ubiquitin and NeuN at 4w, 8w and 12w to detect autophagy mechanism.

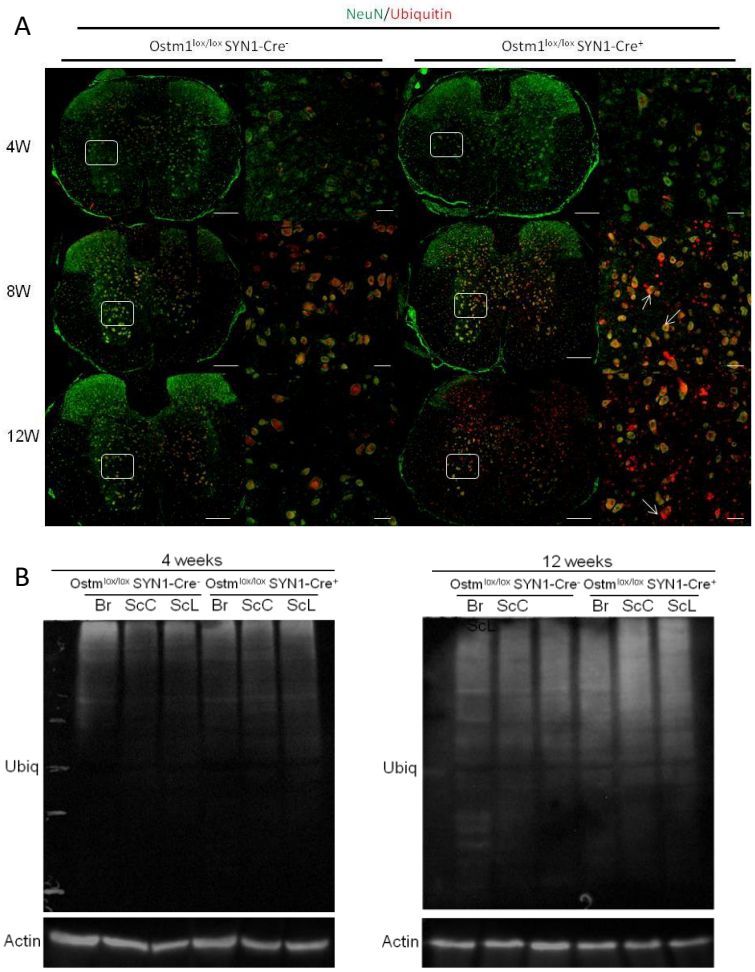

Figure 3-16 Ubiquitin Accumulation in the *Ostm1*$^{lox/lox}$-SYN1-Cre^{+}. (A) Co-immunostaining of Ubiquitin and NeuN displayed an accumulation of Ubiquitin at 8, and 12 weeks Ostm1$^{lox/lox}$-SYN1-Cre^{+} ScL. In addition, ubiquitin aggregates were indicated by arrows. 4W= 4 weeks, 8W= 8 weeks, 12W= 12 weeks Scale bar, 200 µm; 50 µm inset. (B) Immunoblots showing the level of Ubiquitin normalized to actin at 4 and 12 weeks. At 12 weeks, the immunoblots supported the ubiquitin increase in the immunofluorescent results of the ScL and showed an increase in the Br and ScC. Ubiq= Ubiquitin, Br=brain; ScC= spinal cord cervical; ScL= spinal cord lumbar.

The ubiquitin level was not significantly different at 4 weeks consistently with the phenotype. An increase in ubiquitin level co-localizing with neurons was observed at 8w in the *Ostm1*$^{lox/lox}$-SYN1-Cre^{+} compared to the control. The neurons from 12-week-old *Ostm1*$^{lox/lox}$-SYN1-Cre^{+} showed higher ubiquitin accumulation suggesting an increase of ubiquitin level with age (Figure 3-16 A). Both 8 and 12 weeks displayed punctate cytoplasmic staining in the neurons.

To confirm the above results, the expression of ubiquitin was examined using Western blot analysis of the brain, cervical spinal cord and lumbar protein extracts. Consistently with immunohistochemistry, the ubiquitin expression was similar at week 4 in the *Ostm1*$^{lox/lox}$-SYN1-

Cre^{+} and *Ostm1*$^{lox/lox}$-SYN1-Cre^{-}. By 12 weeks of age, the ubiquitin expression was increased in the *Ostm1*$^{lox/lox}$-SYN1-Cre^{+} compared with the controls (Figure 3-16 B).

Hence, these results revealed that neuronal Ostm1 loss of function negatively affected the turnover process of the accumulated proteins.

3.4.2 Impaired Autophagy

Accumulation of intracellular inclusions prompted us to monitor whether the autophagy mechanism, which is associated with protein degradation, was altered. LC3 is one of the fundamental markers in autophagy that is commonly monitored. LC3 consists of two forms: LC3-I cytosolic and LC3-II associated with membrane. LC3-I is cleaved into the active form: LC3-II [89].

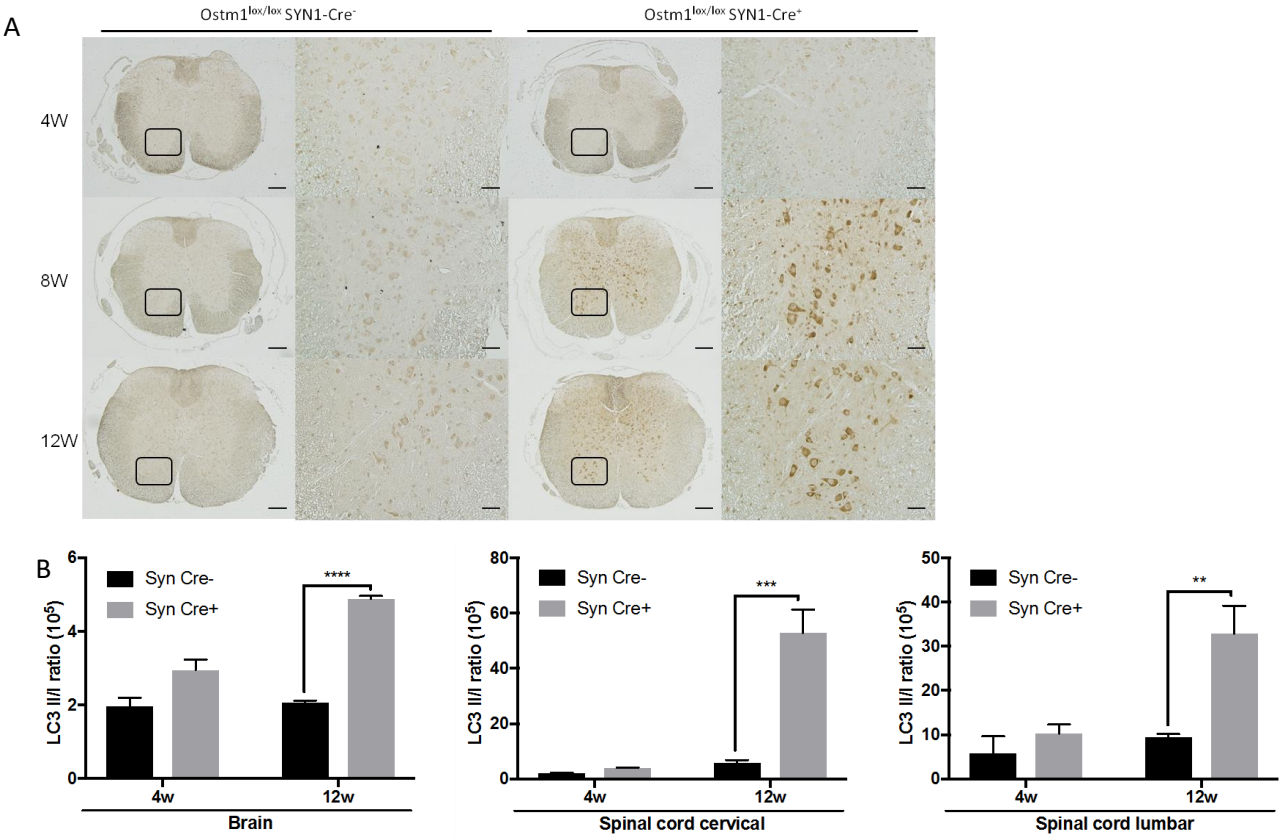

Figure 3-17 Defective and Increased Autophagy Mechanism in the Mutant. (A) LC3 immunostaining in the ScL sections marked an increase in LC3 expression at 8, and 12 weeks in the mutant. Scale bar, 200 µm; 50 µm inset. (B) Quantification of LC3II/I ratio on immunoblots attested the immunostaining in the lumbar spinal cord, and showed a significant increase in the brain and cervical spinal cord at 12 weeks (n=3). **, $p < 0.01$, ***, $p < 0.001$, ****, $p < 0.0001$. *Error bars*, S.E. LC3= light chain 3, 4W= 4 weeks, 8W= 8 weeks, 12W= 12 weeks.

Phagophore elongation is stimulated by LC3-II becoming a component of the autophagosome. An elevated peak of LC3-II is a result of defective autophagy clearance [110].

A general look over LC3 expression was done using immunohistochemistry. The modulation of LC3 was not seen until 8 weeks by color intensity. This immunostaining was increased in the *Ostm1*$^{lox/lox}$-SYN1-Cre^{+} at 12 weeks (Figure 3-17 A).

Consistently, Western blots using protein extracts were done. The significant increase of the expression of LC3-II/I ratio was detected at 12 weeks by 1.5 fold in the brain, 8 fold in the cervical spinal cord, and 2.7 fold in the lumbar spinal cord of the *Ostm1*$^{lox/lox}$-SYN1-Cre^{+} (Figure 3-17 B).

Hence this LC3 elevation could indicate a blockage in autophagy. To support this hypothesis, other autophagy players (e.g. Beclin-1, and p62) had been monitored.

Beclin-1 protein is one of the upstream regulators of autophagy signaling cascade and was monitored by its expression using Western blot of protein extracts. In the brain, the amount of Beclin-1 in *Ostm1*$^{lox/lox}$-SYN1-Cre^{+} was similar at 4 weeks, and 7 times the amount present in the control at 12 weeks. In the cervical spinal cord, the Beclin-1 amount was non-significant at 4 weeks, and then the Beclin1 peak in the mutant became significantly double the peak in the control at 12 weeks. In the lumbar spinal cord, at 4 weeks the Belin-1 result was same as the cervical and the brain, and at 12 weeks the Belin-1 amount in the *Ostm1*$^{lox/lox}$-SYN1-Cre^{+} was 1.25 times that in the control (Figure 3-18).

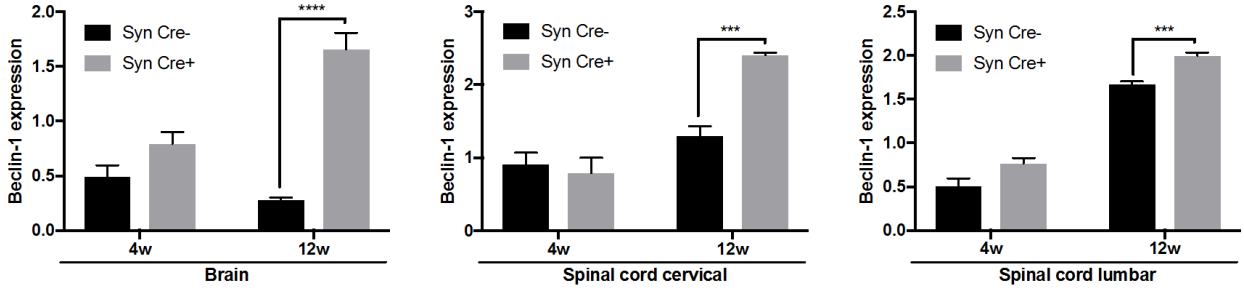

Figure 3-18 Defective Autophagy in the *Ostm1*$^{lox/lox}$-SYN1-Cre^{+}. Quantification of Beclin-1 expression at 4 and 12 weeks using Western Blots showed an increase amount in brain, cervical and lumbar spinal cord at 12 weeks (n=3). 4W= 4 weeks, 12W= 12 weeks. **, $p < 0.01$, ***, $p < 0.001$, ****, $p < 0.0001$. *Error bars*, S.E.

Another marker that consolidates the above hypothesis -defect in autophagy- is p62, which recruits ubiquitinated proteins to the phagophore. Complementary to the Beclin-1 results at 4 weeks, the protein extracts and immunohistochemistry staining did not demonstrate any different

results between the *Ostm1*$^{lox/lox}$-SYN1-Cre^{+} and *Ostm1*$^{lox/lox}$-SYN1-Cre^{-} at 4 weeks. At the point where ubiquitin and LC3 was increased, p62 also started increasing in the mutant as shown in the immunohistochemistry images. Reaching week 12, spinal cord immunostaining area displayed a dark brown color in the Ostm1$^{lox/lox}$-SYN1-Cre^{+} with respect to the control (Figure 3-19 A). Consistently, in the protein extracts, p62 increased in the *Ostm1*$^{lox/lox}$-SYN1-Cre^{+} by 6 folds in the brain, 2.5 folds in the cervical spinal cord and 1 fold in the lumbar spinal cord at 12 weeks (Figure 3-19 B).

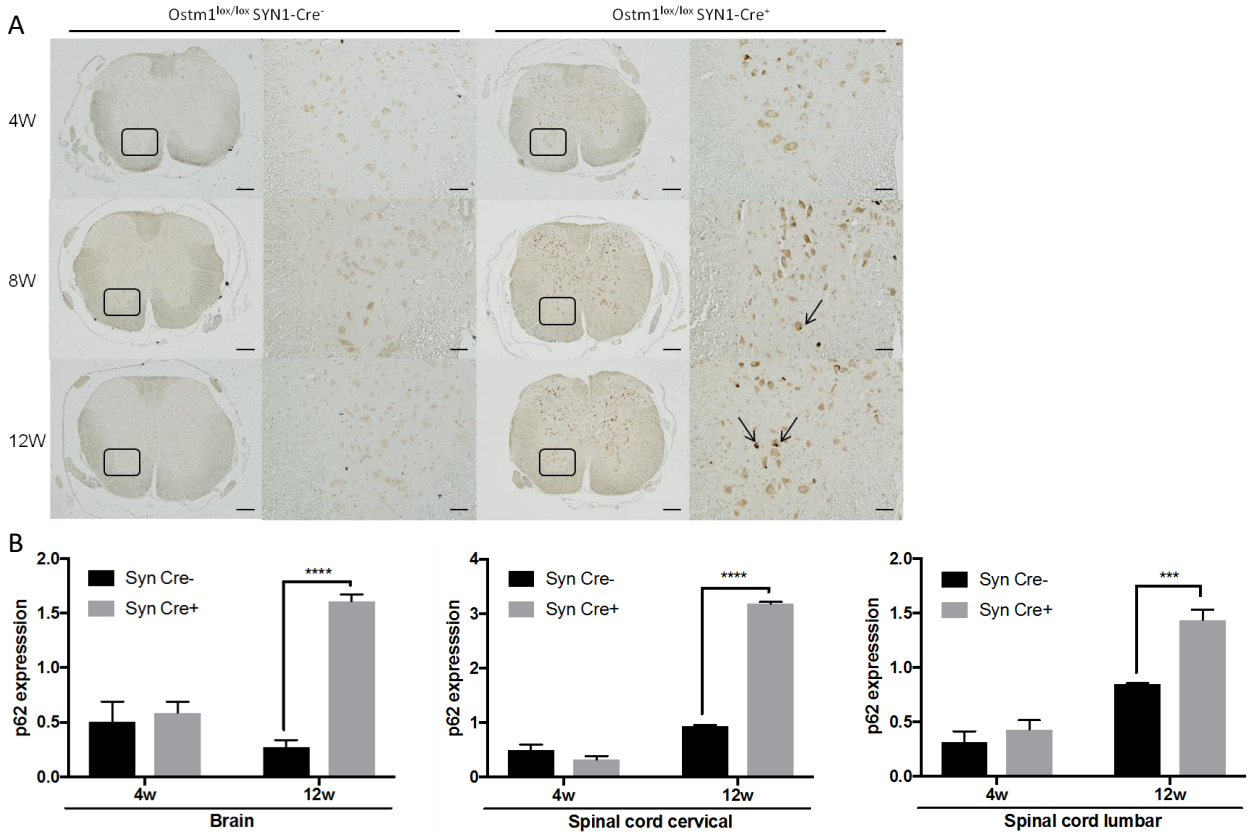

Figure 3-19 Defective Autophagy Mechanism in the Ostm1$^{lox/lox}$-SYN1-Cre^{+}. (A) p62 immunostaining in the ScL sections exhibited an increase in p62 accumulation at 8, and 12 weeks in the mutant. Aggregated p62 are indicated by arrows. Scale bar, 200 μm; 50 μm inset. (B) Quantification of p62 Immunoblots at 4 and 12 weeks confirmed the elevation in the lumbar spinal cord at 12 weeks and also displayed an increase in the brain and cervical spinal cord at 12 weeks (n=3). ***, $p < 0.001$, ****, $p < 0.0001$. *Error bars*, S.E. 4W= 4 weeks, 8W= 8 weeks, 12W= 12 weeks.

Taken together, the enhanced expression of these markers (Figure 3-20) highly corroborated a defective mechanism of autophagy that resulted in accumulating autophagosomes which, in return, impacted the normal homeostasis and trafficking in neurons.

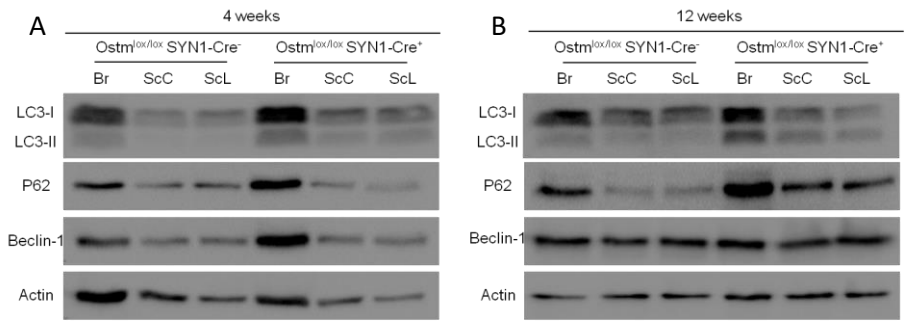

Figure 3-20 Western Blots of 4 and 12 weeks *Ostm1*$^{lox/lox}$-SYN1-Cre^{-} and Cre^{+} Protein Extracts Showed That All Autophagy Markers (LC3, p62, Beclin-1) Underwent an Increase at 12 weeks in Br, ScC, ScL of the Mutant Mice. Br=brain; ScC= spinal cord cervical; ScL= spinal cord lumbar, LC3= light chain 3.

These results are consistent with those documented in the PU.1-Ostm1-gl/gl mice [56] and further supported a major role of autophagy in the neuronal phenotype associated with the loss of Ostm1.

Chapter 4

Discussion

Autosomal recessive osteopetrosis (ARO) is an inherited bone disease and considered one the severest forms of osteopetrosis. It affects infants resulting in enormous bone increase due to the malfunction or absence of osteoclasts [51]. These defective osteoclasts are generated from a heterogeneous molecular defect. The absent or the non-functional osteoclast is associated with extrinsic or intrinsic gene deficits.

Among the intrinsic genes that regulate the functionality of the osteoclast is *Ostm1*. Mutated *Ostm1* underdevelops the osteoclast ruffled border resulting in a non-functional state. These non-functional osteoclasts increase in number as a compensatory mechanism. *OSTM1*-related ARO patients suffered from common ARO symptoms such as increase bone mineral density that produce the "bone in bone" appearance and occupy the bone marrow cavity leading to hematopoietic defects [21, 31]. Patients are more susceptible to infection due to not only bone marrow reductions but also anomalies in myeloid, lymphoid B- and T- lineages which was explored by our lab [84]. Regardless of these common ARO symptoms, *Ostm1* reflected unexpected pathogenesis in the nervous system leading to limiting the life span of ARO patients to 1 year [73]. Subsequently, this prognosis renders *Ostm1* the most severe form of osteopetrosis. In addition to hematopoietic defects, the neurological anomalies that are associated with Ostm1 loss are cerebral atrophy, hypotonia, and heterotopias [73]. This gene was characterized by our lab for the spontaneous grey lethal mutation in mice [76]. Throughout the gene transcription and translation, it produces a type I transmembrane protein, as determined by protein structural analysis [70]. This grey lethal mouse mirrors the severe human malignant ARO, rendering a model to understand in depth its contribution in molecular and cellular process. The grey lethal mouse had a deletion, which was detected by positional cloning, at the start of transcription site of *Ostm1* gene until the beginning of the intron leading to absence of its RNA and protein. The full penetrance of the spontaneously mutated gene in these mice results in their early death at 3-4 weeks of age [76].

All the hematopoietic pathological changes were corrected by *Ostm1* under PU.1 control from a bacterial artificial chromosome transgene. The early expression of PU.1 at initial stage of hematopoietic differentiation rescued the *gl/gl* mice partially suggesting that *Ostm1* is a prerequisite in hematopoietic lineage development in addition to osteoclast lineage. Monitoring the life span of these PU.1-*Ostm1-gl/gl* mice, they lived up to 6-7 weeks, indicating another function of ostm1 in other organs and tissues [84]. This prompted us to unravel the role of Ostm1

in the brain using different analyses. Tackling the PU.1-*Ostm1-gl/gl* mice with neuronal *Ostm1* transgene led to precluding nervous system disorders [56]. Since few studies have been conducted on the neuronal role of Ostm1, the concept and the prognosis are unclear and poor. In addition, *gl/g*l mouse model develops the bone, hematopoietic and neuronal abnormalities that hinder studying the independent role of Ostm1 in cells and organs. We generated a conditional *Ostm1*$^{lox/lox}$ of exon 5 with Synapsin1-Cre to comprehend and characterize the neuronal *Ostm1* loss of function which is highlighted in this thesis. Knocking out exon 5 of *Ostm1* encoding transmembrane protein domain resembles the first Italian human patient [76] who was well defined for his osteopetrotic diagnosis, indicating a role of Ostm1 in pathogenesis of osteopetrosis.

The *Ostm1* condition allele (*Ostm1*^{lox}) functions as the wild type allele in the absence of expressed Cre. Homozygous *Ostm1*^{lox} mice are able to pass their lox allele to future generations, which are phenotypically normal and viable. Cre expression can be regulated by a specific promoter that is activated in a certain organ to function its deletion role. To target the neuronal role of Ostm1, synapsin1 was used. SYN1 modulates the release of the neurotransmitters. It expresses plenty of Cre at E12 driving the deletion of exon 5 at early embryogenesis [95-97]. Regardless of the early expression of Cre, only female heterozygous *Ostm1* $^{lox/+}$-SYN1-Cre^{+} mice were chosen to be crossed with *Ostm1*$^{lox/lox}$ mice to produce *Ostm1*$^{lox/lox}$-SYN1-Cre^{+} due to the low recombination percentage in *Ostm1* $^{lox/+}$- SYN1-Cre^{+} male testes [111]. On the other hand, its early expression coincides with the human patients who had the inherited mutations. The product of Cre deletion is *Ostm1* null allele (*Ostm1*$^{\Delta exon5}$) that is comparable in size to the mutated transcript of ARO patients [76]. The *Ostm1* mouse model generated by deletion of exon 5 developed a neurologic pathogenesis similar to the PU.1-*Ostm1-gl/g*l mice. This indicates that the percentage of recombination was sufficient to construct this pathological phenotype. To confirm the above result, the percentage of recombination was calculated by levels of recombined DNA and RNA.

According to DNA recombination percentage, the *Ostm1*$^{lox/lox}$-SYN1-Cre^{+} neurons demonstrated 64% recombination in the brain, 61% in the ScC, and 64% in the ScL at 4 weeks, which are above the 50% requirement of recombination efficiency for phenotype penetrance. These percentages were sufficient to mimic the spontaneous mutation *Ostm1* allele in the PU.1-*Ostm1-gl/gl* mice due to its pathological and phenotypical changes appearing at 8 weeks even though

the recombination did not reach the 100% optimal range of recombination. Surprisingly, this recombination was monitored at 12 weeks in which there was a significant decrease in recombination percentage reaching 48% in the brain, 47% in the ScC and 48% in the ScL. These reductions suggest a neuronal population decrease that could be due to death and require in-depth investigation.

Supporting DNA recombination, *Ostm1* neuronal expression at 4 weeks of the deleted exon 5 mice was decreased by 67% in the brain, 76% in the ScC and 73% in the ScL. Consistently, the expression followed the same decrease trend as DNA recombination in age development. Phenotypically, the truncated form of Ostm1 protein constrained the life span of the mice to 12-14 weeks which was greater than 6-7 weeks in the PU.1-*Ostm1-gl/gl* mice, but shorter than the normal life span. This increased life span is possibly due to the secreted truncated form of *Ostm1* [70] that was absent in the PU.1-*Ostm1-gl/gl* mice indicating the role of Ostm1 domains in the severity of the disease. Furthermore, the recombination percentage was not 100% as in the PU.1-*Ostm1-gl/gl* mice which might affect the delay in the phenotype. Unlike PU.1-*Ostm1-gl/gl* mice that had absence of Ostm1 in all organs except in the rescued hematopoietic cells, the *Ostm1*$^{lox/lox}$-SYN1-Cre^{+} mice had the Ostm1 loss of function in the neurons. Last but not least, recent studies identified the role of background strains on spinal muscular atrophy (SMA) timing [112], and since the PU.1-*Ostm1-gl/gl* is GL/Le *dlJ +/+ gl* strain and the *Ostm1*$^{lox/lox}$-SYN1-Cre^{+} is C57BL/6, this difference may postpone the onset of the disease. The SYN1-Cre^{+} mice started losing weight at 8 weeks and continued to reach approximately two-thirds the weight of the control at 12 weeks. Their gait developed abnormally at week 8 and progressed with age to accompany tremors, and deficient limb opening that resulted in defective limb clasping. Their backs arched more forming a hump as in Parkinson's disease and ALS [113, 114]. The fatal stage of this severe motor movement involved hind limb paralysis. This locomotion deficit suggests a neuronal abnormality in these mice. The weight loss could be due to gait defects that the mice faced in reaching the food and as this disease progressed with age. Paralysis may contribute to a large extent in impeding its way to eat. The second possible reason is neuronal deficit that might affect the mice's appetite and their digestive system [115]. This behavioral deficit led to investigate the reason by analyzing the brain, the spinal cord, and neuromuscular network. This analysis glimpsed a neuronal degeneration, particularly in the motor neurons. This

incentive led to further examination of the spinal cord and the brain of the *Ostm1*$^{lox/lox}$-SYN1-Cre^{+}.

The locomotion and the motor defect hint that an impaired motor neuronal system is involved. This abnormality can be originating from different regions that control the motor system. To begin with, *Survival Motor neuron 1* (*SMN1*) mutations result in motor neuron loss within the spinal cord [116]. *Prolifin 1* and *copper-zinc superoxide dismutase* (*SOD1*) mutations generate ALS due to loss of upper (corticospinal motors neurons in layer V of the cortex) and lower motor neurons (ventral horn of the spinal cord) [114, 117]. The spontaneous *motor neuron damage* (*mnd*) mutation in the *Cln8* gene known for α-motorneuron degenerations leads to paralysis [118]. Besides the motor degeneration of the spinal cord ventral horn, there are mutations in the neurons of the dorsal horn that control sensory information such as *cramping 1* mutation of *Dync1h1*. These mice were diagnosed by thinner sensory axons and muscle spindle denervation without α-motorneuron loss [119]. Variety of mutations occurred in motor parts instead of the spinal cord like the pathological hind paw clasping mutations that were reported in the cerebellum due to a spontaneous semi-dominant *Weaver* mutation of *Girk2* causing cerebellar granule and Purkinje cell atrophy [120, 121]. Moreover, mutations in the cerebellum affect balance and movement coordination. The *Weaver* mutation spreads to the substantia nigra pars compacta diminishing its dopamine concentration [122]. Disturbances of dopamine levels affect reward-motivated behaviors, motor control, as well secretions of various hormones [123]. Finally, the basal ganglia participate in motor movements, where any mutation as in the *HDH* gene of R6/1 and R6/2 ends up developing Huntington's disease [124]. Previous discoveries of PU.1-*Ostm1-gl/gl* showed CNS inflammatory response and massive neurodegeneration in the brain, and nothing was reported on the spinal cord pathology. Therefore, histological examination was processed on the spinal cord, particularly the ventral horn to link it to the defective phenotype.

The general staining observation indicated a decrease in the total spinal cord size compared to the non-Cre mice. This decrease in size was also found in the brain of the PU.1-*Ostm1-gl/gl* and the *Ostm1*$^{lox/lox}$-SYN1-Cre^{+} which could explain the decrease in weight and suggest a neuronal issue. The myelin lost its demarcation at the beginning of 8 weeks and its concentration was decreased marked by fading of MBP immunostaining at 12 weeks. This fade of color depicted

the grey matter pervading the white matter. Disruption results in motor disorders confirming the tremors and dysrhythmic movement.

Consistently with PU.1-*Ostm1-gl/gl* mice that marked a massive increase in astrocytes and microglia in the brain [56], the spinal cord that is also part of the central system demonstrated a robust activation of astrocytes by histological examination. This robust activation started at the point of behavioural defect and increased with time indicating the severity of the pathogenesis and representing a secondary phenotype from neuronal issues because *Ostm1* is still expressed in glial cells. This astrogliosis mechanism can act as neuroprotection by isolating the damaged region [125]. As long as it can handle it, it maintains protection until a threshold which afterwards causes the neuronal death. The astrocytes eliminate the damaged neurons for the sake of the others [126]. On the other hand, astrocytes can contribute to neuronal damage by increasing toxicity as in Alzheimer's disease where activated astrocytes contribute to plaques formation [127]. Hence, in that case it could be responsible for the pathogenesis. Knowing that astrocytes are non-neuronal cells, their activation suggests a non-cell autonomous role of neuronal Ostm1. NeuN histology showed neuronal loss in the spinal cord at 12 weeks indicating spinal degeneration. Alternatively, astrogliosis could be due to a detection of dysfunction of neurons at 8 weeks and increased as a consequence of neuronal loss at 12 weeks. In particular, the *Ostm*$1^{lox/lox}$-SYN1-Cre^{+} had motor neuron loss at 12 weeks. Our structural analysis of the ventral root axons by EM highly demonstrated an accumulation of inclusions and decrease in myelin thickness. Since myelination is fundamental for proper action potential conduction velocity to generate a rhythmic movement, this hypomyelination is a plausible mechanism of *Ostm1*$^{lox/lox}$-SYN1-Cre^{+} improper locomotion.

Following the track of the motor neurons in which it innervates with the muscles via the neuromuscular junctions, NMJ analysis revealed swelling of the presynaptic axon of the *Ostm1*$^{lox/lox}$-SYN1-Cre^{+} mice, indicating accumulation of compounds at that site. Besides the motor neuron decrease, this swelling blocks the shuttling of neurotransmitters reaching the synaptic terminals and reflects the atrophy of muscle architecture and deficient function.

All the biological techniques whether measuring percentage of DNA recombination, expression level, the number of neurons particularly motor neurons, and NMJ analysis through the denervation indicated a neuronal death.

Reaching the end track of the motor system and based on the evidences above, the expectation of muscle atrophy was validated, indicating the atrophy was not restricted to one type of muscle but to all hind limb muscles. The mutant muscles underwent a 50% decrease in their average cross-sectional surface area and shift to the smaller range size of the myofibers at 12 weeks. Exploration of Ostm1 in relation to other neuronal disorders provided an opportunity to gain insight into the mechanisms of neurodegeneration and shed light on shared pathways of pathogenesis. Accumulation of ubiquitin in neuronal cells was detected in high amounts at 8 and 12 weeks accompanied with punctate aggregates in the cytoplasm in the *Ostm1*$^{lox/lox}$-SYN1-Cre^{+} as this pathological alteration was seen in Huntington's, Parkinson's, and Alzheimer's diseases [128]. This Ubiquitin increase denoted an increased amount of misfolded, dysfunctional, and misprocessed proteins that required recycling. Besides ubiquitin, a misfolded protein marker; p62 is one of the main autophagy indicators that binds polyubiquitinated proteins destining them for autophagy degradation. There was a large increase in p62 in the *Ostm1*$^{lox/lox}$-SYN1-Cre^{+} as well as aggregates indicated by dark brown immunostaining, possibly indicating an increase in autophagosomes due to defects in autophagy in degrading p62 by the lysosome. Subsequently, this elevated level in autophagosomes was detected by LC3-II. In addition to the defect in autophagy, LC3-II increase also alludes for an autophagy rate increase. The elevated levels of Beclin1 autophagy inducer assent this autophagy rate enhancement as a compensatory mechanism for the previously undegraded particles. The accumulation garnered the degeneration fate due to increased toxicity and blocked trafficking as highlighted by swellings in the EM and immuno-fluorescence. Similar undermined trafficking was diagnosed in mutant dynactin/dynein mouse model[129], PI(3,5)P2 deficient mice [130] and Alzheimer's disease mouse models [131]. The basis of this shuttling is proven by its disruption. Autophagosome-lysosome fusion depends on microtubule shuttling, and blockade of this step with microtubule polymerizing drugs reflects enlarged autophagosomes and elevated aggregation of autophagosome substrates [132]. Thus, impaired transport system challenges the transportation of the cargo, leading to stimulation of autophagy that increased autophagosome formation, whereby they accumulate due to their impaired clearance transport destining the cell to its death fate. The absence of Ostm1 prohibited the dispersion of these autophagosomes. Thus, a role in intracellular trafficking can be attributed to Ostm1.

Osteoclast-like cells (OCLs), lacking Ostm1 from *Ostm1*$^{lox/lox}$-Ctsk-Cre^{+}, had no resorption activity and this was not due to intracellular acidification. Indeed, orange staining in the OCLs of the mutant and the control showed normal H^{+} production and acidification. Despite this fact, mutants showed similar diffuse localization during osteoclast activation while controls displayed staining near the ruffled border membrane corresponding to lysosomes to be released in the resorption lacunae. This indicates that Ostm1 contributes a role to endo/lysosomal dispersion [133]. This result also suggests a widespread role of Ostm1 in other cellular trafficking components. The same study also examined the protein secretion by the OCLs lacking Ostm1. A significant decrease in TRAP release levels and undetectable levels in Ctsk hydrolase were observed [133]. Also, Ostm1 directly interacted with KIF5B in the cell lines, which shuttles various vesicles [70]. In accordance with this data and the neuronal data, these results credit the role of Ostm1 in intracellular organization.

The neuronal Ostm1 loss of function shared many histopathologic features ALS and SMA, including muscle paralysis, loss of the ventral horns in the spinal cord, weight loss, glial activation, and increased ubiquitination levels. Despite the shared motor changes, mutant neuronal loss of Ostm1 has its unique etiopathogenesis and disease onset that make it different from other genes involved in neural pathology.

Chapter 5

Conclusion and perspectives

The understanding of Ostm1 role in the *gl/gl* mice could not be easily distinguished due the major bone increase and the extremely short 3-week life span. Since the Ostm1 mutation is expressed in many organs, and because of the partial rescue in the PU.1-*Ostm1-gl/gl* transgenic mouse, we had to create a conditional allele mouse that targets only one defect at a time, preventing other interference. The *in vivo* model (transgenic mice) is better to decipher the role of Ostm1 than *in vitro* due to many reasons: in cell culture, the only target is the cell, however in the transgenic model; the target is the cell and organs in the context of the entire system. Moreover, transgenic models provide an environment that could affect the target cells' growth and vice versa. Hence, one can reveal whether a protein has cell or non-cell autonomous functions where in our case, muscular atrophy and inflammatory response which are secondary phenotypes were observed. This underscores the importance of generating this mice model. Our study recapitulated the changes by neuron axonal swelling and collapsing of the motor neurons, early death, inflammation indicated by astrocyte activation, demyelination, and denervation of the myofibers.

The ignition of these changes started at 8 weeks and progressed until death at 12-14 weeks. Following the pathological development helped to characterize the role of Ostm1 in trafficking in the neurons. *Ostm1*$^{lox/lox}$-SYN1-Cre^{+} transgenic mouse establishes an opportunity to record and understand the Ostm1 function in the neuronal trafficking and neuromuscular crosstalk. There are further tests to check for impairment of autophagy by Akt/mammalian by the target of rapamycin (mTOR pathway) [89]. Since these levels were decreased in the PU.1-*Ostm1-gl/gl* [49], determining the levels in *Ostm1*$^{lox/lox}$-SYN1-Cre^{+} could support the impaired autophagy mechanism. Moreover, the LC3 accumulation suggests two possible explanations: either an elevated level of autophagy or a block in completion of autophagy. To answer this question precisely, an investigation for markers of autophagy should be done. Our results showed an increase in Beclin-1 which hints to an increased autophagy level and can be substantiated by testing the mTOR-independent induction of autophagy.

In addition to the above approaches to determine the defective autophagy, there are further experiments that could confirm this result. For instance, p62 and ubiquitin with peroxidase immunostaining or silver staining could be performed to detect immunodense cytoplasmic inclusion bodies containing ubiquitin and p62 which could confirm the presence of autophagosomes. Since these autophagosomal membranes bud out from the ER and Golgi, an

immunocytochemical analysis for their markers such as ER (GRP94) and Golgi (P115) could confirm the architecture of these inclusions.

Of interest, lysosomal levels could be evaluated to confirm the defective autophagy by measuring Lamp1 and Lamp2. In previous studies in the PU.1-*Ostm1-gl/gl*, these markers expressions were similar to the control indicating unstimulated lysosomal compartment suggesting a fundamental role of Ostm1 in upstream regulation of lysosome [56]. Hence, these results raise another possibility besides aiding in endolysosomal transport on microtubule, this possibility being Ostm1 serving in the fusion of the autophagosome with the lysosome.

Our findings suggest that the ubiquitin proteasome system (UPS) might be negatively affected by *Ostm1* mutation since there is accumulation of ubiquitin, knowing that autophagy serves as a degradation compensator when UPS system is defective [134] and conditional deletion of the autophagy gene causes neuronal atrophy diagnosed by ubiquitin immunoreactive inclusions [135].

Beside our phenotype characterization, these mutant mice have sensory defects due to increased ubiquitin at the dorsal horn of the spinal that were not phenotypically indicated.

Moreover, some gait abnormalities in mice were due to less dopamine levels as in *Weaver* mutation [123]. Knowing that dopamine interferes with hormonal secretion, reward-motivated behaviour, and motor control, it would be interesting to check for its levels.

From our findings, this mouse is a valuable tool in understanding Ostm1 role in trafficking in the neuronal system which makes hematopoietic stem cell transplantation (HSCT) an insufficient therapy. Targeting the pathological changes in the neurons that account for the clinical presentation including paralysis, weak motor coordination and others, may alleviate the severity of the disease and may be translated into a cure for neuronal *Ostm1* disease.

Neuronal stem cell transplantation besides HSCT could be a complementary therapy. Tamaki et al. implement this therapy where neurons were protected and loss of motor control was delayed. Another reasonable therapy could be addressing autophagy besides HSCT [136].

Autophagy is a pro-survival mechanism that occurs at low levels in all cells to execute homeostatic functions. However, it is unregulated in the case of starvation, remodeling and accumulation of toxic components. In contrast to its normal increase state, in disease cases, autophagy exceeds the threshold increase in which it causes more disturbances than benefits. Disturbances in the axonal transports have proven pathogenesis in the human and animal models

[137] and these disturbances precede the timing of clinical signs, indicating that these disturbances are the trigger of the pathogenesis such as in the mutant *SOD1* [138]. Knowing that the vulnerability of the neurons may be related to their post-mitotic state since the accumulated vesicles are not distributed to their daughter cells by cell division [139], so inhibition of autophagy pathway could be a cure for these mice as seen in similar mouse models. For example, supplying the carcinogen-treated rats' hepatocytes with pharmacologic inhibitor of autophagy 3-methyladenine (3-MA) that impedes class III PI3K delays their demise [140]. In addition, this success was also applied in chloroquine-treated cortical neurons [141], in nerve growth factor-deprived sympathetic neurons [142], and many others. In the context of proving that autophagy can induce cell death, a study unraveled death inhibition in non-apoptotic committed ($Bax^{-/-}$, $Bak^{-/-}$) murine fibroblasts treated with killing agents (stuarosporine and etopside) by Atg5, and Beclin-1 RNA interference [143].

Tackling the defective autophagy mechanism as a potential target for treatment in Ostm1 patients in addition to hematopoietic transplant could decrease the accumulation of autophagosomes, thereby reducing the toxicity and opening the axonal pathway for trafficking. This treatment could be accomplished by either activating mTOR activity that represses autophagy mechanism or disruption of ATGs interaction could diminish the upregulated autophagy blocked mechanism. The goal of this treatment is extending the duration of the period free of symptoms and decreasing the severity of the disease. One of the well-known examples on this treatment is inhibiting autophagy by 3-methyladenine in the SMNdelta7 SMA mouse which delays motor neuron degeneration, suppresses autophagosome formation and extends their life span [144]. Thus, targeting autophagy could be a therapeutic approach.

Finally, a third approach to cure osteopetrotic patients is by replacing the origin of the pathogenesis. After knowing the genetic and molecular basis of Ostm1, gene therapy with an entire complete length of *Ostm1* could be the cure. This process could be mediated by adeno-associated virus to replace the mutated *Ostm1* as it scored several successful therapies in SMA diseases. These were recapitulated by presence of 60% expression of SMN protein in spinal cord motor proteins, rescue of the muscle atrophy leading to enhanced motor and strength functions, and extension of their life span up to 400 days, encompassing an increase by 25-fold compared to the 16 days in the mutant untreated mice [145]. Measuring the cure outcomes in *OSTM1*

osteopetrotic patients in a timely, efficient and safe manner will be required to complement the HSCT with gene therapy to avoid the drawbacks, making ARO no longer fatal and incurable.

Appendix 1

IRCM INSTITUT DE RECHERCHES CLINIQUES DE MONTRÉAL
AFFILIÉ À L'UNIVERSITÉ DE MONTRÉAL

Dr Jean Vacher
cancer et maladies génétiques
Institut de recherches cliniques de Montréal
110 avenue des Pins Ouest
Montréal, QC H2W 1R7

2018-12-21

Objet :
Projet # 2019-1022 / 2018-15 JV - Approbation après approbation conditionnelle
Titre: Molecular analysis of osteopetrosis

Investigateur principal : Dr Vacher

Dr Vacher,

Le comité de protection des animaux de l'Institut de recherches cliniques de Montréal (IRCM) a évalué les réponses aux conditions et les documents modifiés pour le projet mentionné dans l'objet de cette lettre.

Il nous fait plaisir de confirmer l'approbation finale de votre projet. Cette approbation est en vigueur jusqu'au 21/12/2022.

Il est de votre responsabilité de soumettre une nouvelle demande avant la date d'expiration. Il est également de votre responsabilité d'aviser le comité dans les plus brefs délais de toute modification au projet.

Je vous rappelle que vous devez inscrire le numéro de protocole sur les cages des animaux correspondants à votre projet et que vous pourrez commander des animaux que si un numéro de protocole est inscrit sur votre commande.

Je vous prie d'agréer, cher collègue, l'expression de mes sentiments les meilleurs.

Artur Kania

Chair, Animal Care Committee

Président, Comité de protection des animaux

Bibliography

1. Herculano-Houzel, S., *The human brain in numbers: a linearly scaled-up primate brain.* Frontiers in human neuroscience, 2009. **3**: p. 31.
2. Brodal, P. and R.E.C.M. Fund, *The Central Nervous System: Structure and Function*. 2004: Oxford University Press, USA.
3. Noback, C.R., et al., *The Human Nervous System: Structure and Function*. 2005: Humana Press.
4. Catala, M. and N. Kubis, *Gross anatomy and development of the peripheral nervous system.* Handb Clin Neurol, 2013. **115**: p. 29-41.
5. Kandel, E.R., J.H. Schwartz, and T.M. Jessell, *Principles of Neural Science*. 1991: Elsevier.
6. Arber, S., *Motor circuits in action: specification, connectivity, and function.* Neuron, 2012. **74**(6): p. 975-89.
7. Brown, A.G., *Organization in the Spinal Cord: The Anatomy and Physiology of Identified Neurones*. 2012: Springer London.
8. Jessen, K.R., *Glial cells.* Int J Biochem Cell Biol, 2004. **36**(10): p. 1861-7.
9. Engel, A.G., *The neuromuscular junction.* Handb Clin Neurol, 2008. **91**: p. 103-48.
10. Clarke, B., *Normal bone anatomy and physiology.* Clin J Am Soc Nephrol, 2008. **3 Suppl 3**: p. S131-9.
11. An, Y.H. and K.L. Martin, *Handbook of histology methods for bone and cartilage*. 2003: Springer.
12. Buckwalter, J., et al., *Bone biology.* J Bone Joint Surg Am, 1995. **77**(8): p. 1256-1275.
13. Hadjidakis, D.J. and I.I. Androulakis, *Bone remodeling.* Annals of the New York Academy of Sciences, 2006. **1092**(1): p. 385-396.
14. Boskey, A. and A. Posner, *Bone structure, composition, and mineralization.* The Orthopedic clinics of North America, 1984. **15**(4): p. 597-612.
15. Härle, F. and R.J. Boudrieau, *Maxillofacial bone healing*, in *Oral and maxillofacial surgery in dogs and cats*. 2012, Elsevier. p. 7-13.
16. Broadhead, M.L., et al., *Therapeutic targeting of osteoclast function and pathways.* Expert opinion on therapeutic targets, 2011. **15**(2): p. 169-181.
17. Marks Jr, S.C. and S.N. Popoff, *Bone cell biology: the regulation of development, structure, and function in the skeleton.* American Journal of Anatomy, 1988. **183**(1): p. 1-44.
18. Capulli, M., R. Paone, and N. Rucci, *Osteoblast and osteocyte: games without frontiers.* Archives of biochemistry and biophysics, 2014. **561**: p. 3-12.

19. Parfitt, A., *Targeted and nontargeted bone remodeling: relationship to basic multicellular unit origination and progression.* Bone (New York, NY), 2002. **30**(1): p. 5-7.
20. Duong, L.T., et al., *Integrins and signaling in osteoclast function.* Matrix Biology, 2000. **19**(2): p. 97-105.
21. Tolar, J., S.L. Teitelbaum, and P.J. Orchard, *Osteopetrosis.* New England Journal of Medicine, 2004. **351**(27): p. 2839-2849.
22. Takahashi, H., B. Epker, and H. Frost. *Resorption precedes formative activity*. in *Surgical forum*. 1964.
23. Durand, M., et al., *Monocytes from patients with osteoarthritis display increased osteoclastogenesis and bone resorption: the In Vitro Osteoclast Differentiation in Arthritis study.* Arthritis & Rheumatism, 2013. **65**(1): p. 148-158.
24. Parfitt, A., *The cellular basis of bone remodeling: the quantum concept reexamined in light of recent advances in the cell biology of bone.* Calcified Tissue International, 1984. **36**(1): p. S37-S45.
25. Owen, R. and G.C. Reilly, *In vitro models of bone remodelling and associated disorders.* Frontiers in bioengineering and biotechnology, 2018. **6**: p. 134.
26. Frattini, A., et al., *Defects in TCIRG1 subunit of the vacuolar proton pump are responsible for a subset of human autosomal recessive osteopetrosis.* Nature genetics, 2000. **25**(3): p. 343-346.
27. Villa, A., et al., *Infantile malignant, autosomal recessive osteopetrosis: the rich and the poor.* Calcified tissue international, 2009. **84**(1): p. 1.
28. Del Fattore, A., et al., *Clinical, genetic, and cellular analysis of 49 osteopetrotic patients: implications for diagnosis and treatment.* Journal of medical genetics, 2006. **43**(4): p. 315-325.
29. Bollerslev, J., et al., *Ultrastructural investigations of bone resorptive cells in two types of autosomal dominant osteopetrosis.* Bone, 1993. **14**(6): p. 865-869.
30. Albers-Schonberg, H., *Rntgenbilder einer seltenen Knochenkrankung.* Munchen Med Wochenschr, 1904. **51**: p. 365.
31. Bhati, P. and P. Goyal, *A Rare Case of Osteopetrosis with Unusual Feature as Microcephaly.* Journal of clinical and diagnostic research: JCDR, 2017. **11**(8): p. SJ01.
32. Del Fattore, A., A. Cappariello, and A. Teti, *Genetics, pathogenesis and complications of osteopetrosis.* Bone, 2008. **42**(1): p. 19-29.
33. Sobacchi, C., et al., *Osteopetrosis: genetics, treatment and new insights into osteoclast function.* Nature Reviews Endocrinology, 2013. **9**(9): p. 522.

34. Teitelbaum, S.L. and F.P. Ross, *Genetic regulation of osteoclast development and function.* Nature Reviews Genetics, 2003. **4**(8): p. 638.
35. Lézot, F., et al., *Skeletal consequences of RANKL-blocking antibody (IK22-5) injections during growth: mouse strain disparities and synergic effect with zoledronic acid.* Bone, 2015. **73**: p. 51-59.
36. Yavropoulou, M. and J. Yovos, *Osteoclastogenesis--current knowledge and future perspectives.* J Musculoskelet Neuronal Interact, 2008. **8**(3): p. 204-216.
37. Yoshida, H., et al., *The murine mutation osteopetrosis is in the coding region of the macrophage colony stimulating factor gene.* Nature, 1990. **345**(6274): p. 442-444.
38. Weilbaecher, K.N., et al., *Linkage of M-CSF signaling to Mitf, TFE3, and the osteoclast defect in Mitfmi/mi mice.* Molecular cell, 2001. **8**(4): p. 749-758.
39. Li, J., et al., *RANK is the intrinsic hematopoietic cell surface receptor that controls osteoclastogenesis and regulation of bone mass and calcium metabolism.* Proceedings of the national academy of sciences, 2000. **97**(4): p. 1566-1571.
40. Simonet, W., et al., *Osteoprotegerin: a novel secreted protein involved in the regulation of bone density.* Cell, 1997. **89**(2): p. 309-319.
41. Yagi, M., et al., *DC-STAMP is essential for cell–cell fusion in osteoclasts and foreign body giant cells.* The Journal of experimental medicine, 2005. **202**(3): p. 345-351.
42. Roodman, G.D., *Regulation of osteoclast differentiation.* Annals of the New York Academy of Sciences, 2006. **1068**(1): p. 100-109.
43. Boyle, W.J., W.S. Simonet, and D.L. Lacey, *Osteoclast differentiation and activation.* Nature, 2003. **423**(6937): p. 337-342.
44. Suda, T. and N. Takahashi, *Contributions to osteoclast biology from Japan.* Proceedings of the Japan Academy, Series B, 2008. **84**(10): p. 419-438.
45. Rajapurohitam, V., et al., *The mouse osteopetrotic grey-lethal mutation induces a defect in osteoclast maturation/function.* Bone, 2001. **28**(5): p. 513-523.
46. Aubin, J.E., *Perspectives: Osteoclast adhesion and resorption: The role of podosomes.* Journal of Bone and Mineral Research, 1992. **7**(4): p. 365-368.
47. Senel, K., et al., *Type II autosomal dominant osteopetrosis.* Rheumatology international, 2002. **22**(3): p. 116-118.
48. Henriksen, K., et al., *Osteoclasts from patients with autosomal dominant osteopetrosis type I caused by a T253I mutation in low-density lipoprotein receptor-related protein 5 are normal in*

vitro, but have decreased resorption capacity in vivo. The American journal of pathology, 2005. **167**(5): p. 1341-1348.

49. Cleiren, E., et al., *Albers-Schönberg disease (autosomal dominant osteopetrosis, type II) results from mutations in the ClCN7 chloride channel gene.* Human molecular genetics, 2001. **10**(25): p. 2861-2867.
50. Sly, W.S., et al., *Carbonic anhydrase II deficiency identified as the primary defect in the autosomal recessive syndrome of osteopetrosis with renal tubular acidosis and cerebral calcification.* Proceedings of the National Academy of Sciences, 1983. **80**(9): p. 2752-2756.
51. Balemans, W., L. Van Wesenbeeck, and W. Van Hul, *A clinical and molecular overview of the human osteopetroses.* Calcified tissue international, 2005. **77**(5): p. 263-274.
52. Helfrich, M.H., *Osteoclast diseases.* Microscopy research and technique, 2003. **61**(6): p. 514-532.
53. Cummings, T.J. and A.D. Proia, *Optic nerve compression in infantile malignant autosomal recessive osteopetrosis.* Journal of pediatric ophthalmology and strabismus, 2004. **41**(4): p. 241-244.
54. Stocks, R.M.S., et al., *Malignant infantile osteopetrosis: otolaryngological complications and management.* Archives of Otolaryngology–Head & Neck Surgery, 1998. **124**(6): p. 689-694.
55. Frattini, A., et al., *Chloride channel ClCN7 mutations are responsible for severe recessive, dominant, and intermediate osteopetrosis.* Journal of bone and mineral research, 2003. **18**(10): p. 1740-1747.
56. Héraud, C., et al., *Severe neurodegeneration with impaired autophagy mechanism triggered by ostm1 deficiency.* Journal of Biological Chemistry, 2014. **289**(20): p. 13912-13925.
57. Kornak, U., et al., *Mutations in the a3 subunit of the vacuolar H+-ATPase cause infantile malignant osteopetrosis.* Human molecular genetics, 2000. **9**(13): p. 2059-2063.
58. Wilson, C. and A. Vellodi, *Autosomal recessive osteopetrosis: diagnosis, management, and outcome.* Archives of disease in childhood, 2000. **83**(5): p. 449-452.
59. Guerrini, M.M., et al., *Human osteoclast-poor osteopetrosis with hypogammaglobulinemia due to TNFRSF11A (RANK) mutations.* The American journal of human genetics, 2008. **83**(1): p. 64-76.
60. Pettit, A.R., et al., *TRANCE/RANKL knockout mice are protected from bone erosion in a serum transfer model of arthritis.* The American journal of pathology, 2001. **159**(5): p. 1689-1699.
61. Jefferies, K.C., D.J. Cipriano, and M. Forgac, *Function, structure and regulation of the vacuolar (H+)-ATPases.* Archives of biochemistry and biophysics, 2008. **476**(1): p. 33-42.

62. Demirci, F., et al., *Identification, genomic structure, and screening of the vacuolar proton-ATPase membrane sector-associated protein M8-9 gene within the COD1 critical region (Xp11. 4).* Mol Vis, 2001. **7**: p. 234-9.
63. Stevens, T.H. and M. Forgac, *Structure, function and regulation of the vacuolar (H+)-ATPase.* Annual review of cell and developmental biology, 1997. **13**(1): p. 779-808.
64. Toyomura, T., et al., *Three subunit a isoforms of mouse vacuolar H+-ATPase preferential expression of the a3 isoform during osteoclast differentiation.* Journal of Biological Chemistry, 2000. **275**(12): p. 8760-8765.
65. Scimeca, J.-C., et al., *The gene encoding the mouse homologue of the human osteoclast-specific 116-kDa V-ATPase subunit bears a deletion in osteosclerotic (oc/oc) mutants.* Bone, 2000. **26**(3): p. 207-213.
66. Henriksen, K., et al., *Characterization of osteoclasts from patients harboring a G215R mutation in ClC-7 causing autosomal dominant osteopetrosis type II.* The American journal of pathology, 2004. **164**(5): p. 1537-1545.
67. Wartosch, L., et al., *Lysosomal degradation of endocytosed proteins depends on the chloride transport protein ClC-7.* The FASEB Journal, 2009. **23**(12): p. 4056-4068.
68. Kornak, U., et al., *Loss of the ClC-7 chloride channel leads to osteopetrosis in mice and man.* Cell, 2001. **104**(2): p. 205-215.
69. Kasper, D., et al., *Loss of the chloride channel ClC-7 leads to lysosomal storage disease and neurodegeneration.* The EMBO journal, 2005. **24**(5): p. 1079-1091.
70. Pandruvada, S.N., et al., *Role of Ostm1 cytosolic complex with kinesin 5B in intracellular dispersion and trafficking.* Molecular and cellular biology, 2016. **36**(3): p. 507-521.
71. Lange, P.F., et al., *ClC-7 requires Ostm1 as a β-subunit to support bone resorption and lysosomal function.* Nature, 2006. **440**(7081): p. 220-223.
72. Pangrazio, A., et al., *Mutations in OSTM1 (grey lethal) define a particularly severe form of autosomal recessive osteopetrosis with neural involvement.* Journal of Bone and Mineral Research, 2006. **21**(7): p. 1098-1105.
73. Maranda, B., et al., *Clinical and cellular manifestations of OSTM1-related infantile osteopetrosis.* Journal of Bone and Mineral Research, 2008. **23**(2): p. 296-300.
74. Jäkel, S. and D. Gürlich, *Importin β, transportin, RanBP5 and RanBP7 mediate nuclear import of ribosomal proteins in mammalian cells.* The EMBO journal, 1998. **17**(15): p. 4491-4502.

75. Steward, C., *Neurological aspects of osteopetrosis.* Neuropathology and applied neurobiology, 2003. **29**(2): p. 87-97.
76. Chalhoub, N., et al., *Grey-lethal mutation induces severe malignant autosomal recessive osteopetrosis in mouse and human.* Nature medicine, 2003. **9**(4): p. 399-406.
77. Manganaro, L., et al., *Bilateral subependymal heterotopia, ventriculomegaly and cerebellar asymmetry: fetal MRI findings of a rare association of brain anomalies.* Journal of radiology case reports, 2013. **7**(11): p. 38.
78. Grüneberg, H., *Grey-lethal, a new mutation in the house mouse.* Journal of Heredity, 1936. **27**(3): p. 105-109.
79. Prinetti, A., et al., *Brain lipid composition in grey-lethal mutant mouse characterized by severe malignant osteopetrosis.* Glycoconjugate journal, 2009. **26**(6): p. 623-633.
80. Igisu, H. and K. Suzuki, *Progressive accumulation of toxic metabolite in a genetic leukodystrophy.* Science, 1984. **224**(4650): p. 753-755.
81. Reddy, A., E.V. Caler, and N.W. Andrews, *Plasma membrane repair is mediated by Ca2+-regulated exocytosis of lysosomes.* Cell, 2001. **106**(2): p. 157-169.
82. Choo-Smith, L.-P.i. and W.K. Surewicz, *The interaction between Alzheimer amyloid β (1–40) peptide and ganglioside GM1-containing membranes.* FEBS letters, 1997. **402**(2-3): p. 95-98.
83. Fortin, D.L., et al., *Lipid rafts mediate the synaptic localization of α-synuclein.* Journal of Neuroscience, 2004. **24**(30): p. 6715-6723.
84. Pata, M., C. Héraud, and J. Vacher, *OSTM1 bone defect reveals an intercellular hematopoietic crosstalk.* Journal of Biological Chemistry, 2008. **283**(45): p. 30522-30530.
85. Supanchart, C., *Characterization of the osteopetrotic Clcn7-/-mouse mutant rescued by osteoclast-specific expression of ClC-7*. 2009.
86. Huang, G., et al., *PU. 1 is a major downstream target of AML1 (RUNX1) in adult mouse hematopoiesis.* Nature genetics, 2008. **40**(1): p. 51.
87. Mizushima, N., *Autophagy: process and function.* Genes & development, 2007. **21**(22): p. 2861-2873.
88. Lum, J.J., R.J. DeBerardinis, and C.B. Thompson, *Autophagy in metazoans: cell survival in the land of plenty.* Nature reviews Molecular cell biology, 2005. **6**(6): p. 439-448.
89. Galluzzi, L. and D.R. Green, *Autophagy-independent functions of the autophagy machinery.* Cell, 2019. **177**(7): p. 1682-1699.

90. Green, D.R. and F. Llambi, *Cell death signaling.* Cold Spring Harbor perspectives in biology, 2015. **7**(12): p. a006080.
91. Luft, J.H., *Improvements in epoxy resin embedding methods.* The Journal of Cell Biology, 1961. **9**(2): p. 409-414.
92. Mortensen, R., *Overview of gene targeting by homologous recombination.* Current protocols in neuroscience, 2007. **40**(1): p. 4.29. 1-4.29. 13.
93. Meier, I.D., et al., *Short DNA sequences inserted for gene targeting can accidentally interfere with off-target gene expression.* The FASEB Journal, 2010. **24**(6): p. 1714-1724.
94. Bouabe, H. and K. Okkenhaug, *Gene targeting in mice: a review*, in *Virus-Host Interactions*. 2013, Springer. p. 315-336.
95. Melloni Jr, R.H. and L.J. Degennaro, *Temporal onset of synapsin I gene expression coincides with neuronal differentiation during the development of the nervous system.* Journal of Comparative Neurology, 1994. **342**(3): p. 449-462.
96. Cesca, F., et al., *The synapsins: key actors of synapse function and plasticity.* Progress in neurobiology, 2010. **91**(4): p. 313-348.
97. Zhu, Y., et al., *Ablation of NF1 function in neurons induces abnormal development of cerebral cortex and reactive gliosis in the brain.* Genes & development, 2001. **15**(7): p. 859-876.
98. Bjugn, R. and H.J.G. Gundersen, *Estimate of the total number of neurons and glial and endothelial cells in the rat spinal cord by means of the optical disector.* Journal of Comparative Neurology, 1993. **328**(3): p. 406-414.
99. Bahney, J. and C.S. von Bartheld, *The cellular composition and glia–neuron ratio in the spinal cord of a human and a nonhuman primate: comparison with other species and brain regions.* The Anatomical Record, 2018. **301**(4): p. 697-710.
100. Allen, N.J. and B.A. Barres, *Glia—more than just brain glue.* Nature, 2009. **457**(7230): p. 675-677.
101. Fu, Y., et al., *Cellular composition characterizing postnatal development and maturation of the mouse brain and spinal cord.* Brain Structure and Function, 2013. **218**(5): p. 1337-1354.
102. Duan, W., et al., *Novel insights into NeuN: from neuronal marker to splicing regulator.* Molecular neurobiology, 2016. **53**(3): p. 1637-1647.
103. Yuan, A., M.V. Rao, and R.A. Nixon, *Neurofilaments and neurofilament proteins in health and disease.* Cold Spring Harbor perspectives in biology, 2017. **9**(4): p. a018309.
104. Perrot, R., et al., *Review of the multiple aspects of neurofilament functions, and their possible contribution to neurodegeneration.* Molecular neurobiology, 2008. **38**(1): p. 27-65.

105. Ganapathy, M.K. and P. Tadi, *Neuroanatomy, Spinal Cord Morphology*, in *StatPearls [Internet]*. 2019, StatPearls Publishing.
106. Oda, Y., *Choline acetyltransferase: the structure, distribution and pathologic changes in the central nervous system.* Pathology international, 1999. **49**(11): p. 921-937.
107. Kariya, S., et al., *Reduced SMN protein impairs maturation of the neuromuscular junctions in mouse models of spinal muscular atrophy.* Human molecular genetics, 2008. **17**(16): p. 2552-2569.
108. Ravara, B., et al., *Functional electrical stimulation as a safe and effective treatment for equine epaxial muscle spasms: Clinical evaluations and histochemical morphometry of mitochondria in muscle biopsies.* European journal of translational myology, 2015. **25**(2).
109. Sarelius, I.H., et al., *Capillarity and fiber types in the cremaster muscle of rat and hamster.* American Journal of Physiology-Heart and Circulatory Physiology, 1983. **245**(2): p. H368-H374.
110. Klionsky, D.J., et al., *Guidelines for the use and interpretation of assays for monitoring autophagy in higher eukaryotes.* Autophagy, 2008. **4**(2): p. 151-175.
111. Rempe, D., et al., *Synapsin I Cre transgene expression in male mice produces germline recombination in progeny.* Genesis, 2006. **44**(1): p. 44-49.
112. Eshraghi, M., et al., *Effect of genetic background on the phenotype of the Smn2B/-mouse model of spinal muscular atrophy.* Human molecular genetics, 2016. **25**(20): p. 4494-4506.
113. Duty, S. and P. Jenner, *Animal models of Parkinson's disease: a source of novel treatments and clues to the cause of the disease.* British journal of pharmacology, 2011. **164**(4): p. 1357-1391.
114. Fil, D., et al., *Mutant Profilin1 transgenic mice recapitulate cardinal features of motor neuron disease.* Human molecular genetics, 2017. **26**(4): p. ddw429.
115. Furness, J., *Types of neurons in the enteric nervous system.* Journal of the autonomic nervous system, 2000. **81**(1-3): p. 87-96.
116. Crawford, T.O. and C.A. Pardo, *The neurobiology of childhood spinal muscular atrophy.* Neurobiology of disease, 1996. **3**(2): p. 97-110.
117. Ripps, M.E., et al., *Transgenic mice expressing an altered murine superoxide dismutase gene provide an animal model of amyotrophic lateral sclerosis.* Proceedings of the National Academy of Sciences, 1995. **92**(3): p. 689-693.
118. Messer, A. and L. Flaherty, *Autosomal dominance in a late-onset motor neuron disease in the mouse.* Journal of neurogenetics, 1986. **3**(6): p. 345-355.

119. Braunstein, K.E., et al., *A point mutation in the dynein heavy chain gene leads to striatal atrophy and compromises neurite outgrowth of striatal neurons.* Human molecular genetics, 2010. **19**(22): p. 4385-4398.
120. Hirano, A. and H.M. Dembitzer, *Cerebellar alterations in the weaver mouse.* The Journal of cell biology, 1973. **56**(2): p. 478-486.
121. Herrup, K. and E. Trenkner, *Regional differences in cytoarchitecture of the weaver cerebellum suggest a new model for weaver gene action.* Neuroscience, 1987. **23**(3): p. 871-885.
122. Roffler-Tarlov, S. and A.M. Graybiel, *Expression of the weaver gene in dopamine-containing neural systems is dose-dependent and affects both striatal and nonstriatal regions.* Journal of Neuroscience, 1986. **6**(11): p. 3319-3330.
123. Ko, J.H. and A.P. Strafella, *Dopaminergic neurotransmission in the human brain: new lessons from perturbation and imaging.* The Neuroscientist, 2012. **18**(2): p. 149-168.
124. Mangiarini, L., et al., *Exon 1 of the HD gene with an expanded CAG repeat is sufficient to cause a progressive neurological phenotype in transgenic mice.* Cell, 1996. **87**(3): p. 493-506.
125. Pekny, M., et al., *The role of astrocytes and complement system in neural plasticity.* International review of neurobiology, 2007. **82**: p. 95-111.
126. Giaume, C., et al., *Glia: the fulcrum of brain diseases.* Cell Death & Differentiation, 2007. **14**(7): p. 1324-1335.
127. Nagele, R.G., et al., *Contribution of glial cells to the development of amyloid plaques in Alzheimer's disease.* Neurobiology of aging, 2004. **25**(5): p. 663-674.
128. Platt, F.M., B. Boland, and A.C. van der Spoel, *Lysosomal storage disorders: The cellular impact of lysosomal dysfunction.* Journal of Cell Biology, 2012. **199**(5): p. 723-734.
129. Laird, F.M., et al., *Motor neuron disease occurring in a mutant dynactin mouse model is characterized by defects in vesicular trafficking.* Journal of Neuroscience, 2008. **28**(9): p. 1997-2005.
130. Ferguson, C.J., G.M. Lenk, and M.H. Meisler, *Defective autophagy in neurons and astrocytes from mice deficient in PI (3, 5) P2.* Human molecular genetics, 2009. **18**(24): p. 4868-4878.
131. Lee, S., Y. Sato, and R.A. Nixon, *Lysosomal proteolysis inhibition selectively disrupts axonal transport of degradative organelles and causes an Alzheimer's-like axonal dystrophy.* Journal of Neuroscience, 2011. **31**(21): p. 7817-7830.
132. Ravikumar, B., et al., *Dynein mutations impair autophagic clearance of aggregate-prone proteins.* Nature genetics, 2005. **37**(7): p. 771-776.

133. Pata, M. and J. Vacher, *Ostm1 bifunctional roles in osteoclast maturation: insights from a mouse model mimicking a human OSTM1 mutation.* Journal of Bone and Mineral Research, 2018. **33**(5): p. 888-898.

134. Pandey, U.B., et al., *HDAC6 rescues neurodegeneration and provides an essential link between autophagy and the UPS.* Nature, 2007. **447**(7146): p. 860-864.

135. Hara, T., et al., *Suppression of basal autophagy in neural cells causes neurodegenerative disease in mice.* Nature, 2006. **441**(7095): p. 885-889.

136. Tamaki, S.J., et al., *Neuroprotection of host cells by human central nervous system stem cells in a mouse model of infantile neuronal ceroid lipofuscinosis.* Cell stem cell, 2009. **5**(3): p. 310-319.

137. Griffin, J.W. and D.L. Price. *Axonal transport in motor neuron pathology*. in *UCLA forum in medical sciences*. 1976.

138. Williamson, T.L. and D.W. Cleveland, *Slowing of axonal transport is a very early event in the toxicity of ALS–linked SOD1 mutants to motor neurons.* Nature neuroscience, 1999. **2**(1): p. 50-56.

139. Yang, Y. and K. Herrup, *Cell division in the CNS: protective response or lethal event in post-mitotic neurons?* Biochimica et Biophysica Acta (BBA)-Molecular Basis of Disease, 2007. **1772**(4): p. 457-466.

140. Schwarze, P.E. and P.O. Seglen, *Reduced autophagic activity, improved protein balance and enhanced in vitro survival of hepatocytes isolated from carcinogen-treated rats.* Experimental cell research, 1985. **157**(1): p. 15-28.

141. Zaidi, A.U., et al., *Chloroquine-induced neuronal cell death is p53 and Bcl-2 family-dependent but caspase-independent.* Journal of Neuropathology & Experimental Neurology, 2001. **60**(10): p. 937-945.

142. Xue, L., G.C. Fletcher, and A.M. Tolkovsky, *Autophagy is activated by apoptotic signalling in sympathetic neurons: an alternative mechanism of death execution.* Molecular and Cellular Neuroscience, 1999. **14**(3): p. 180-198.

143. Shimizu, S., et al., *Role of Bcl-2 family proteins in a non-apoptotic programmed cell death dependent on autophagy genes.* Nature cell biology, 2004. **6**(12): p. 1221-1228.

144. Piras, A., et al., *Inhibition of autophagy delays motoneuron degeneration and extends lifespan in a mouse model of spinal muscular atrophy.* Cell death & disease, 2017. **8**(12): p. 1-16.

145. Foust, K.D., et al., *Rescue of the spinal muscular atrophy phenotype in a mouse model by early postnatal delivery of SMN.* Nature biotechnology, 2010. **28**(3): p. 271-274.